DISSERTATION

EVALUATION AND APPLICATION OF POLARIMETRIC RADAR DATA FOR THE MEASUREMENT OF RAINFALL

Submitted by

Gwo-Jong Huang

Department of Electrical and Computer Engineering

In partial fulfillment of the requirements

for the Degree of Doctor of Philosophy

Colorado State University

Fort Collins, Colorado

Summer, 2003

COLORADO STATE UNIVERSITY

May 7th, 2003

WE HEREBY RECOMMEND THAT THE DISSERTATION PREPARED UNDER OUR SUPERVISION BY GWO-JONG HUANG ENTITLED EVALUATION AND APPLICATION OF POLARIMETRIC RADAR DATA FOR THE MEASUREMENT OF RAINFALL BE ACCEPTED AS FULFILLING IN PART REQUIREMENTS FOR THE DEGREE OF DOCTOR OF PHILOSOPHY.

Committee on Graduate Work

Dr. V. Chandrasekar

Dr. Derek L. Lile

Dr. Steven A. Rutledge

Adviser: Dr. V. N. Bringi

Department Head

ABSTRACT OF DISSERTATION

EVALUATION AND APPLICATION OF POLARIMETRIC RADAR DATA FOR THE MEASUREMENT OF RAINFALL

The measurement of rainfall using weather radar technologies is an important application in our daily life. Rainfall measurement is important in hydrology and flash flood prediction. Physically-based methods rely fundamentally on the precipitation model, namely, models for the drop size distribution (dsd), drop shape, and drop orientation (or, canting). Traditionally, surface disdrometer, aircraft imaging probes and profilers (a vertical pointing Doppler radar usually operating in the VHF or UHF bands) are used in studying the dsd variability. However, these instruments have limited spatial and temporal resolution. On the other hand, scanning radar can offer measurements with high spatial and temporal resolution. Dual-polarization radar technologies which use the back scatter and forward scatter based measurements at two polarization states (horizontal and vertical) have progressed dramatically in recent decades. However, the accuracy of the precipitation model has not been systematically addressed; this thesis seeks to more fully address the basic model assumptions and the related issue of accuracy.

In the first part of this thesis, we propose an areal rainfall algorithm which uses differential propagation phase shift (Φ_{dp}). In this algorithm, we assume that the R-K_{dp} relationship is 'locally' linear in a small K_{dp} interval. We show that the random noise and measurement fluctuations can be reduced significantly by

averaging rainfall over an area. Since K_{dp} is a function of the mean axis ratio of drops, we apply a "β correction" as proposed by Gorgucci et al. (1999, 2000)[16, 17]. The β is the slope of equivalent spherical diameter of drop versus the mean axis ratio which can change due to drop oscillations and canting in different rainfall types. By comparing the estimated areal rainfall rate with areal gage rainfall rate, we show that the "β correction" method can significantly reduce the bias in accumulation over an area.

Since the β is associated with mean axis ratio, and axis ratio is a function of equivalent spherical diameter of drops, it implies that the β should include information about drop size. In the following chapter, we use β along with Z_h and Z_{dr} to retrieve dsd parameters of a normalized gamma model following Bringi et al. (2002)[11]. After retrieving the gamma dsd parameters, we propose a polarimetrically-based Z-R algorithm of the form $Z = aR^{1.5}$, where the coefficient can be continuously adjusted. We compare radar retrieved dsd data with profiler dsd data, and the pol-based Z-R relation with gage rain rate from two long duration rain events from Brazil and Florida.

In chapter 4, we study the drop orientation (or, canting angle) distribution. We first examine the effects of drop oscillation on drop orientation, and then study the relation between the drop orientation distribution and the canting angle distribution. Since polarimetric radar observations are based on the polarization plane, we need to convert drop orientation angles to canting angles. Based on the natural behavior of drop orientation (i.e., azimuthal symmetry), the canting angle should have zero mean. So we only estimate the standard deviation of canting angle (σ_β) from the polarimetric data. We study two existing σ_β estimators; the first one based on the ratio of maximum and minimum of cross-power, namely, ρ_4 method and the second proposed by Ryzhkov (2001) which use LDR and Z_{dr} data. A new algorithm is also proposed which we call the "simplified ρ_4 method".

In addition, we propose another algorithm to estimate σ_β using the asymmetric ratio (A_{sy}). The asymmetric ratio is defined as the ratio of two eigen values of the Graves power matrix. We test the stability of these four algorithms and also show that these algorithms are not sensitive to the dsd and canting angle distributions. In the end, we apply the Ryzhkov method and the simplified ρ_4 algorithm to three rain events. The results for σ_β appear to be reasonable, and even though the two algorithms do not agree with each other for low Z_{dr} values, we are able to explain the differences.

Gwo-Jong Huang
Department of Electrical and Computer Engineering
Colorado State University
Fort Collins, Colorado 80523
Summer, 2003

ACKNOWLEDGEMENTS

The author would like to take this opportunity to express his deep gratitude to his advisers Dr. V.N. Bringi for his inspiring direction, unceasing encouragement and support during the course of his graduate studies; Dr. V. Chandrasekar, Dr. Steven A. Rutledge and Dr. Derek L. Lile for their time and effort to review and comment on the thesis.

The author would like to extend his appreciation to the CSU-CHILL radar staff D.A. Brunkow for providing CSU-CHILL radar data and giving constructive suggestion; and P.C. Kennedy for helping out with data collection.

Additionally, the author sincerely acknowledges Dr. J. Hubbert offer well calibrated STEPS data and sharing his diverse knowledge and experience; and those fellows in the Radar and Communications Group at CSU: Dr. W. Li, Dr. S. Bolen, Y. Wang, T. Tang, Y. Liu and all others, for their direct or indirect involvement to help complete this thesis.

DEDICATION

To my parents Huang, Chi-Mei and Chen, Li-Po.

To my grandmother Chen-Tang, Ken-Suir;

and to my love Wu, Mindy.

TABLE OF CONTENTS

LIST OF FIGURES

LIST OF TABLES

Chapter 1

INTRODUCTION

1.1 A Brief Review

Radar is a electromagnetic device to detect the properties of a target such as position, velocity, size and orientation. The basic electromagnetic theories and concepts were developed in the late 19th century. Although scientists realized the possibility of radar, the accomplishment of radar was limited by electrical technology. The first radar was built on 11 December 1924 by E. V. Appleton (1926)[2]. Radar technology developed very fast during and after World War II. Today, radar is used in many areas. One application we are interested in this thesis is weather observation.

Radar applied to weather observation started in the late 1940's. Atlas and his colleagues (1951)[3] proposed the relation between backscatter and microphysical properties of precipitation particles. In the 1970's dual-polarization radar theories were developed by McCormick and Hendry (circular polarization radar; McCormick and Hendry, 1972, 1976, 1979)[37, 21, 36], and Seliga and Bringi (linear polarization; 1976, 1978)[47, 48]. At the same time, Pruppacher et al. (1970, 1971) [40, 41] and Green (1975)[19] showed that the axis ratio of raindrops are a functional of drop size. Combining dual-polarization radar theories and drop size studies, dual-polarization radar becomes a powerful weather observation tool.

Basically, there are two types of dual-polarization radar, namely, circular-polarization and linear-polarization radar. Circular-polarization radar can separate

shape effects from canting angle effects by measuring the circular depolarization ratio (CDR) and the degree of preferred orientation ($ORTT$) (Hendry and Antar, 1987)[20]. These parameters offer a basis for hydrometeor identification. However, propagation effects in circular polarization are significant and must be corrected. On the other hand, linear polarization radar is less affected by propagation effects. Especially, propagation attenuation at S-band is typically quite small. Since linear horizontal polarization radar gives maximum return power in rain, it is used in the majority of weather radar systems.

1.1.1 Polarization Ellipse

An incident plane wave with real amplitude E_o, propagating in the $\hat{k}_i$ direction can be expressed in a linear basis as,

$$\vec{E}_i(\vec{r}) = E_o \hat{e}_i \exp(-j\vec{k}\cdot\vec{r}) \tag{1-1a}$$

$$= (E_h^i \hat{h}_i + E_v^i \hat{v}_i)\exp(-j\vec{k}\cdot\vec{r}) \tag{1-1b}$$

where $\vec{k} = k_o\hat{k}_i$, $\hat{k}_i = \hat{v}_i \times \hat{h}_i$ and $\hat{e}_i$ is a complex unit vector to express the polarization state of the plane wave. The electric field at origin ($\vec{r} \equiv O$) is,

$$\vec{E}^i(O) = E_o\hat{e}_i = |E_h^i|e^{j\theta_h}\hat{h}_i + |E_v^i|e^{j\theta_v}\hat{v}_i$$

$$= e^{j\theta_h}\left[|E_h^i|\hat{h}_i + |E_v^i|e^{j\delta}\hat{v}_i\right] \tag{1-2}$$

Because E_o is the real amplitude of $\vec{E}_i$, the unit polarization vector, $\hat{e}_i$, can be written as,

$$\hat{e}_i = e^{j\theta_h}\left[\cos\epsilon\hat{h}_i + \sin\epsilon e^{j\delta}\hat{v}_i\right] \tag{1-3}$$

where $\epsilon = \cos^{-1}(|E_h^i|/E_o)$ and polarization ratio (χ_i) is,

$$\chi_i = \frac{E_v^i}{E_h^i} = \tan\epsilon e^{j\delta} \tag{1-4}$$

From these equations, we can get the other orthogonal basis (circular basis) easily. In time-domain (add time phaser $\exp(j\omega t)$) and $\epsilon = 45^o$, the trace of E-field in $(\hat{h}_i,\hat{v}_i)$ plane is a circle; the trace will rotate clockwise (right-hand sense) when $\delta = 90^o$ and counter-clockwise (left-hand sense) when $\delta = -90^o$. So the complex basis of circular polarization is related to linear basis as,

$$\begin{bmatrix} \hat{e}_R \\ \hat{e}_L \end{bmatrix} = \frac{1}{\sqrt{2}} \begin{bmatrix} 1 & j \\ 1 & -j \end{bmatrix} \begin{bmatrix} \hat{h}_i \\ \hat{v}_i \end{bmatrix} \tag{1-5}$$

where the subscripts R and L denote the right-hand and left-hand circular states. The E-fields in time-domain can be expressed in circular basis as,

$$\vec{E}^i(O,t) = |E_R|e^{j\theta_R}e^{j\omega t} + |E_L|e^{j\theta_L}e^{j\omega t} \tag{1-6}$$

where θ_R and θ_L are the initial phases for two circular components. By applying (1-5), the E-field becomes to,

$$\vec{E}^i(O,t) = e^{j[(\theta_R+\theta_L)/2+\omega t]} \left[\hat{h}_i'(\frac{|E_R|+|E_L|}{\sqrt{2}}) + j\hat{v}_i'(\frac{|E_R|-|E_L|}{\sqrt{2}})\right] \tag{1-7}$$

where $\hat{h}_i'$ is the direction when E_R and E_L are in-phase, and $\hat{v}_i'$ is the direction when they are out-phase. The real part of $\vec{E}^i(t)$ is,

$$\vec{E}^i(t) = \hat{h}_i'\left[(\frac{|E_R|+|E_L|}{\sqrt{2}})\cos(\omega t+\beta)\right] + \hat{v}_i'\left[(\frac{|E_R|-|E_L|}{\sqrt{2}})\cos(\omega t+\beta+\frac{\pi}{2})\right] \tag{1-8}$$

where $\beta = (\theta_R+\theta_L)/2$.

Fig. 1.1a shows the traces of E_R and E_L. The initial phase of E_R (θ_R) is counted clockwise (counter-clockwise) from horizontal ($\hat{h}_i$ direction) if θ_R is positive (negative), and θ_L is counted oppositely as θ_R. Since E_R and E_L rotate oppositely, $\vec{E}^i(t)$ would have minimum value ($|E_R| - |E_L|$, assuming $|E_R| > |E_L|$) when two

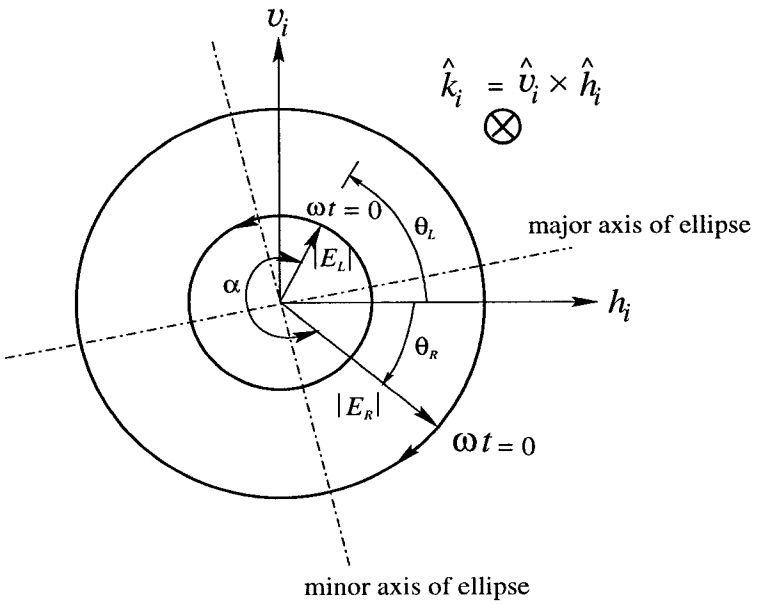

(*a*)

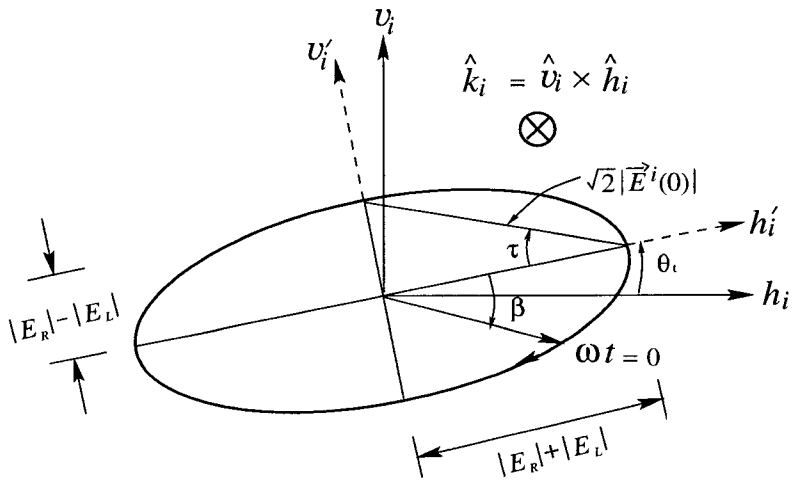

(*b*)

Figure 1.1: **(a)** The right-hand and left-hand circular components for a plane wave propagating along $\hat{k}_i = \hat{v}_i \times \hat{h}_i$. **(b)** Elliptical polarization by combining two components in (a).

components are out-phase (at $\hat{v}_i'$ direction), and have maximum value ($|E_R|+|E_L|$) when they are in-phase (at $\hat{h}_i'$ direction). The trace of $\vec{E}^i(t)$, thus, is a ellipse known as "polarization ellipse" (see Fig. 1.1b). From (1-8) and Fig. 1.1, we can define two important angles, ellipticity angle (τ) and tilt (or orientation) angle (θ_t), as

$$\tau = \tan^{-1}\left(\frac{|E_R|-|E_L|}{|E_R|+|E_L|}\right) \tag{1-9a}$$

$$\theta_t = \frac{\theta_R - \theta_L}{2} \tag{1-9b}$$

The polarization ratio (χ_i, see (1-4)) in terms of τ and θ_t are,

$$\chi_i = \frac{\tan\theta_t + j\tan\tau}{1 - j\tan\theta_t\tan\tau} \tag{1-10a}$$

$$= \frac{\cos(2\tau)\sin(2\theta_t) + j\sin(2\tau)}{1+\cos(2\tau)\cos(2\theta_t)} \tag{1-10b}$$

1.1.2 Scattering Matrix, Covariance Matrix and Basis Transformation

When the incident plane wave described in (1-1a) illuminates a target, part of energy is scattered and part is absorbed by the target. The scattered E-field can be expressed in ($\hat{h}_s$,$\hat{v}_s$) basis as,

$$\vec{E}^s = E_h^s\hat{h}_s + E_v^s\hat{v}_s \tag{1-11}$$

where the scattered wave propagates in the $\hat{k}_s$ direction and $\hat{k}_s = \hat{v}_s \times \hat{h}_s$. The relation between incident wave and scattered wave is (Jones 1941)[29],

$$\begin{bmatrix} E_h^s \\ E_v^s \end{bmatrix} = \frac{e^{jk_o r}}{r}\begin{bmatrix} S_{hh} & S_{hv} \\ S_{vh} & S_{vv} \end{bmatrix}_{FSA}\begin{bmatrix} E_h^i \\ E_v^i \end{bmatrix} \tag{1-12}$$

The 2x2 matrix which can also be written as $\mathbf{S}_{FSA}$ is known as scattering matrix. The subscript, FSA, is for "forward scatter alignment". In radar application, we

are interested in the wave scattered back toward to the radar. The "reflected" E-field, thus, propagates in the "opposite" direction of forward scatter ($\hat{k}_r = -\hat{k}_s = \hat{v}_r \times \hat{h}_r$). The $\hat{v}_r$ is defined the same as $\hat{v}_s$ and $\hat{h}_r = \hat{h}_s$. Therefore, the $\vec{E}^s$ is,

$$\begin{aligned} \begin{bmatrix} E_h^r \\ E_v^r \end{bmatrix} &= \begin{bmatrix} -1 & 0 \\ 0 & 1 \end{bmatrix} \begin{bmatrix} E_h^s \\ E_v^s \end{bmatrix} \\ &= \frac{e^{-jk_o r}}{r} \begin{bmatrix} -1 & 0 \\ 0 & 1 \end{bmatrix} \begin{bmatrix} S_{hh} & S_{hv} \\ S_{vh} & S_{vv} \end{bmatrix} \begin{bmatrix} E_h^i \\ E_v^i \end{bmatrix} \end{aligned} \tag{1-13}$$

The scattering matrix in "back scatter alignment" convention is,

$$\mathbf{S}_{BSA} = \begin{bmatrix} -1 & 0 \\ 0 & 1 \end{bmatrix} \mathbf{S}_{FSA} \tag{1-14}$$

The back scatter matrix for monostatic radar satisfies the reciprocity theorem which means the cross-polar scattering components are equal ($S_{hv} = S_{vh}$). So there are three independent components in the $\mathbf{S}_{BSA}$ to describe the scattering feature of the target. The feature vector can be defined as (Tragl 1990)[53],

$$\mathbf{\Omega}^T = \begin{bmatrix} S_{hh} & \sqrt{2}S_{hv} & S_{vv} \end{bmatrix} \tag{1-15}$$

where superscript "T" refer to transpose, and $\sqrt{2}$ is introduced to satisfy norm conservation under polarization transformation. Using $\mathbf{\Omega}$, Tragl defined the covariance matrix ($\mathbf{\Sigma}$) for random targets as,

$$\begin{aligned} \mathbf{\Sigma} &= \langle \mathbf{\Omega}\mathbf{\Omega}^{T*} \rangle \\ &= \begin{bmatrix} \langle |S_{hh}|^2 \rangle & \sqrt{2}\langle S_{hh}S_{hv}^* \rangle & \langle S_{hh}S_{vv}^* \rangle \\ \sqrt{2}\langle S_{hv}S_{hh}^* \rangle & 2\langle |S_{hv}|^2 \rangle & \sqrt{2}\langle S_{hv}S_{vv}^* \rangle \\ \langle S_{vv}S_{hh}^* \rangle & \sqrt{2}\langle S_{vv}S_{hv}^* \rangle & \langle |S_{vv}|^2 \rangle \end{bmatrix} \end{aligned} \tag{1-16}$$

where "*" refer to conjugate and $\langle . \rangle$ denotes time average. The covariance matrix shown above includes three real and three complex terms. The three diagonal terms are real and represent mean copolar power at H and V-polarizations, and

the cross-polar power. The three upper triangle terms are complex and represent (two co-cross and one co-co) correlation coefficients.

The covariance matrix shown in (1-16) is measured in the (H,V) basis. Actually, we can transform to any orthogonal elliptical basis by using the unitary polarization transformation matrix. The transformation matrix ($\mathbf{T}(\chi)$) is (Tragl 1990)[53],

$$\mathbf{T}(\chi) = \frac{1}{1+\chi\chi^*} \begin{bmatrix} 1 & \sqrt{2}\chi & \chi^2 \\ -\sqrt{2}\chi^* & (1-\chi\chi^*) & \sqrt{2}\chi \\ (\chi^*)^2 & -\sqrt{2}\chi^* & 1 \end{bmatrix} \tag{1-17}$$

where χ is the polarization ratio defined in (1-10a,b). The new covariance matrix in the transformed basis (defined by ellipticity angle τ and tilt angle θ_t) is,

$$\mathbf{\Sigma}' = \mathbf{T}(\chi) \cdot \mathbf{\Sigma} \cdot \mathbf{T}^{T*}(\chi) \tag{1-18}$$

For example, we have covariance matrix in (H,V) basis and need to calculate the covariance matrix in slant 45^o mode. We can let $\tau = 0^o$ (linear polarization) and $\theta_t = 45^o$. Put τ and θ_t into (1-10a,b) to get polarization ratio (χ). Using (1-17) and (1-18) we can get covariance matrix for slant 45^o mode.

As mentioned in the beginning of this section, the different polarization bases (linear and circular) have their own advantages and disadvantages. The covariance matrix includes the most important properties of the radar observables. Therefore, combining covariance matrix measurements and basis transformation can offer more information about the targets.

1.2 Overview of Thesis

This thesis contains 5 chapters as follows:

Chapter 1 Introduction

This chapter gives a brief review of dual-polarization weather radar development. Following the review, we introduce some important concepts of dual-polarization radar theories which include polarization state, scattering matrix, covariance matrix and basis transformation.

Chapter 2 The Areal Rainfall Estimate

An areal rainfall estimate based on differential phase shift is proposed. We compare our algorithm with another algorithm which is based on the same concept, but our approach is different in theory and implementation. Moreover, we have introduced a β correction method which will correct the rainfall estimation error due to mean shape changes caused by drop oscillations. The cases study analyzed shows that the β method can improve the rain accumulation when compared against gages.

Chapter 3 Estimation of Gamma Rain Drop Size Distribution Parameters by Polarization Radar

Based on an equivalent linear mean axis ratio model (β method discussed above), drop size distribution (dsd) parameters are retrieved using Z_h, Z_{dr} and K_{dp} data. We are able to extend the dsd retrieval algorithm for low rain rates where K_{dp} and Z_{dr} tend to be "noisy" signals. We also propose a new coefficient adjustable Z-R relationship. This rainfall estimator is more accurate and more flexible than the traditional Z-R estimator.

Chapter 4 Drop Orientation and Canting Angle

There are three main properties of precipitation namely, dsd, mean axis ratio model and drop orientation distribution which must be specified before a radar-based algorithm can be used to estimate rainfall or dsd parameters. We discuss the drop orientation distribution model due to turbulence and

oscillation. We have analyzed three different canting angle estimators using simulations and show their impact on the radar observables. Finally, we discussed the impact of canting angle to radar observables.

Chapter 5 Conclusion

We summarize the achievements and contributions of this thesis, and suggest how they may be extended in future studies.

Chapter 2

THE AREAL RAINFALL ESTIMATE

Rainfall measurement is an important topic in radar meteorology. Surface rainfall rate is measured using rain gauges. However, rain gauges can only offer the rainfall rate as a function of time at a specified location. It is not realistic to get high spatial resolution measurement over a large area by using gauges. On the other hand, weather radars can overcome this disadvantage. Therefore, the rainfall estimation techniques become an important issue for radar meteorology, especially algorithms using dual-polarization radar.

One important rain rate algorithm is R-K_{dp} (Sachidananda et al. 1987)[45] given as,

$$R(K_{dp}) = cK_{dp}^{b} \qquad ; mm\, h^{-1} \tag{2-1}$$

where R is rainfall rate. The coefficient c and exponent b are dependent on the radar frequency, the raindrop shape model and to some extent on the drop size distribution. There are some advantages of using K_{dp} to calculate rainfall rate. First, K_{dp} is the range derivative of differential phase(Φ_{dp}). It can be expressed as,

$$K_{dp} = \frac{1}{2}\frac{d\Phi_{dp}}{dr} \tag{2-2}$$

Therefore, K_{dp} is not affected by radar system gain or propagation attenuation. Although any phase measurement will contain a system offset, the offset should

be constant for a stable radar system. Therefore, the system phase offset will cancel out by the derivative operation. Second, the reflectivity factor, Z, is the 6th moment of drop size distribution (dsd) and can be expressed as,

$$Z = \int_D D^6 N(D) dD \tag{2-3}$$

On the other hand, K_{dp} is approximately proportional to the 4th moment of the dsd. In the Raleigh limit, it can be written as,

$$K_{dp} = \frac{\pi k_o}{12} Re \left[\int_D D^3 N(D) F(r, \epsilon_r) dD \right] \tag{2-4}$$

where $F(r, \epsilon_r)$ is a function of axis ratio (r) and relative permitivity (ϵ_r), (see Chapter 7, Bringi and Chandrasekar 2001) [9]. Therefore, K_{dp} is less affected by variations in the drop size distribution (Zrnić et al. ; 1996)[43], compared to the other algorithms based on reflectivity.

The radar estimates the rainfall rate in the resolution volume which is always above the ground. On the other hand, rain gauges measure the rainfall rate on the ground. Therefore, there is always some bias and fluctuation error between radar rainfall rate estimates and gauge estimates. This problem can be viewed as a statistical estimation problem (Chapter 8, Bringi and Chandrasekar 2001)[9]. Generally, algorithms to solve this problem are based on statistical/engineering-based techniques or on physically-based techniques. There are many statistical/engineering algorithms such as neural-network, probability-matched and areal-time integral(ATI). In this dissertation, we will focus on physically-based techniques and, in particular, on the mean areal rain rate algorithm based on differential propagation phase (Φ_{dp}) which is useful in hydrological applications.

2.1 Theoretical Basis

Let $R(x, y)$ represent the rainfall rate. The areal rainfall in a Cartesian region can be expressed as,

$$\begin{aligned} AR &= \int\int R(x,y)dxdy \\ &= \bar{R} \cdot A \end{aligned} \tag{2-5}$$

where $\bar{R}$ is the average rainfall rate and A is the area of the region. In polar coordinates, (2-6) can be written as,

$$AR = \int\int R(r,\theta)rdrd\theta \tag{2-6}$$

Combining (2-1) and (2-6),

$$AR = \int\int c \cdot K_{dp}^{b}(r,\theta)rdrd\theta. \tag{2-7}$$

2.1.1 Ryzhkov and Zrnić Formula

Although we can calculate AR from (2-7), K_{dp} is not measured by radar directly. We want to compute AR from Φ_{dp} since this is directly measured. In order to express (2-7) in terms of Φ_{dp}, Ryzhkov et al. (2000)[44] suggested that the exponent b in the equation is close to unity (around .83). Since K_{dp} is radial derivative of Φ_{dp}, K_{dp} over the range interval (r_1, r_n) should be approximately proportional to the $\Phi_{dp}(r_n) - \Phi_{dp}(r_1)$. If $r_n - r_1$ is small, then K_{dp} can be assumed to be a constant in this interval; thus, (2-7) can be simplified as,

$$\begin{aligned} AR_{rzf} &= \int_{\theta_1}^{\theta_n} c \cdot K_{dp}^{b}(\theta) \int_{r_1}^{r_n} rdrd\theta \\ &= \int_{\theta_1}^{\theta_n} c \cdot K_{dp}^{b}(\theta) \cdot \frac{r_n^2 - r_1^2}{2} d\theta \end{aligned} \tag{2-8}$$

Note that "rzf" refers to Ryzhkov-Zrnić formula. From (2-2), K_{dp} can be expressed using finite differences as,

$$K_{dp} = \frac{1}{2}\frac{\Phi_{dp}(r_n,\theta) - \Phi_{dp}(r_1,\theta)}{r_n - r_1} \tag{2-9}$$

and substituting into (2-8), the AR can be written as,

$$AR_{rzf} = \frac{c}{2}\int_{\theta_1}^{\theta_n}(r_n^2 - r_1^2)(\frac{1}{2}\frac{\Phi_{dp}(r_n,\theta) - \Phi_{dp}(r_1,\theta)}{r_n - r_1})^b d\theta, \tag{2-10}$$

and the numerical approximation is,

$$\begin{aligned} AR_{rzf} &= \frac{c}{2}\sum_{i=1}^{n}(r_n + r_1)(r_n - r_1)[\frac{1}{2}\frac{\Phi_{dp}(r_n,\theta_i) - \Phi_{dp}(r_1,\theta_i)}{r_n - r_1}]^b\Delta\theta \\ &= \frac{c}{2}\sum_{i=1}^{n}\frac{r_n + r_1}{2}[2(r_n - r_1)]^{1-b}[\Phi_{dp}(r_n,\theta) - \Phi_{dp}(r_1,\theta)]^b\Delta\theta \end{aligned} \tag{2-11}$$

2.1.2 CSU Formula

Starting from (2-7), Bringi and Chandrasekar (2001)[9] give another approach in chapter 8 of their book. They assume that the exponent b is equal to one. Integrating (2-7) by parts, the AR can be written as

$$AR_{csu} = \frac{c}{2}\int_{\theta_1}^{\theta_n}\left[r_n\Phi_{dp}(r_n,\theta) - r_1\Phi_{dp}(r_1,\theta) - \int_{r_1}^{r_n}\Phi_{dp}(r,\theta)dr\right]d\theta, \tag{2-12}$$

where "csu" refers to CSU algorithm. The numerical form is,

$$AR_{csu} = \frac{c}{2}\sum_j\left[r_n\Phi_{dp}(r_n,\theta_j) - r_1\Phi_{dp}(r_1,\theta_j) - \sum_i\Phi_{dp}(r_i,\theta_j)\Delta r\right]\Delta\theta. \tag{2-13}$$

Fig. 2.1 shows the scatter plot of R vs. K_{dp} based on scattering simulations and measured dsds. The simulations use the operating frequency of 5.5 GHz (C-band) and, the axis ratio relationship given by Andsager et al. (1999)[1] for $1 \leq D \leq 4$ mm and Beard et al. (1987)[7] for $D < 1$ or $D > 4$ mm. In addition, the canting angle distribution is assumed to be Gaussian with zero mean and

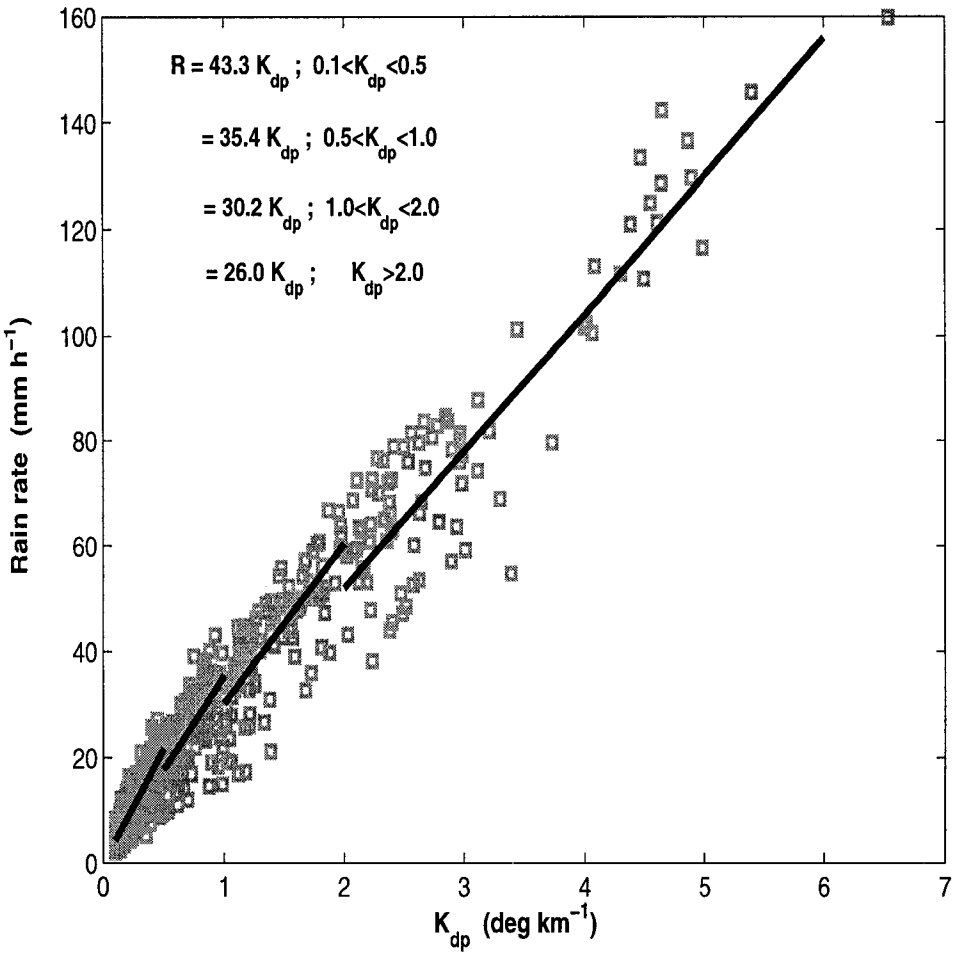

Figure 2.1: The R vs. K_{dp} scatter plot from Darwin dsd at C-band. Note that dark solid lines are the piece-wise linear fit for C-band.

K_{dp} ; ($^o/km$)	Coefficient for C-band	Coefficient for S-band
0.1 - 0.5	43.3	81.5
0.5 - 1.0	35.4	65.5
1.0 - 2.0	30.2	57.5
otherwise	26.0	59.8

Table 2.1: The coefficient for piece-wise linear fitting.

standard deviation of 10^o which is applicable to tropical rain (Chapter 7, Bringi and Chandrasekar 2001) [9]. It is obvious that R-K_{dp} follows a power law. If we force the equation to be linear, the bias in the low rainfall rate region will be large. Therefore, we separate K_{dp} into several portions and then the R-K_{dp} relationship will become linear in each segment. This method is called piece-wise linear fitting (see Fig. 2.1). The coefficient c is listed in Table 2.1 for C and S-bands.

2.1.3 β Correction

Both Ryzhkov-Zrnić and CSU algorithms are based on K_{dp} measurements. Theoretically, all radar parameters, including K_{dp}, can be calculated by specifying the drop size distribution (dsd). A common dsd model is the gamma distribution which can be expressed as (Ulbrich 1983)[54],

$$N(D) = n_c f(D) \tag{2-14}$$

where D is equivalent spherical diameter, n_c is the concentration and $f(D)$ is the gamma probability function which can be written as,

$$f(D) = \frac{\Lambda^{\mu+1}}{\Gamma(\mu+1)} e^{-\Lambda D} D^{\mu} \tag{2-15}$$

with n_c defined as,

$$n_c = N_0 \frac{\Gamma(\mu+1)}{\Lambda^{\mu+1}} \tag{2-16}$$

where Λ and μ are the gamma pdf's parameters. The volume-weighted median drop diameter, D_0, is defined by,

$$\int_0^{D_0} D^3 N(D) dD = \int_{D_0}^{\infty} D^3 N(D) dD \tag{2-17}$$

In terms of dsd, the horizontal reflectivity factor (Z_h), the differential reflectivity (Z_{dr}) and K_{dp} can be defined as,

$$Z_h = \frac{\lambda^4}{\pi^5 |k|^2} \int \sigma_h(D) N(D) dD \quad (mm^6 m^{-3}) \tag{2-18a}$$

$$Z_{dr} = 10 log_{10} \frac{\int \sigma_h(D) N(D) dD}{\int \sigma_v(D) N(D) dD} \quad (dB) \tag{2-18b}$$

$$K_{dp} = \frac{180\lambda}{\pi} Re \left[\int [\hat{h} \cdot \vec{f}(D) - \hat{v} \cdot \vec{f}(D)] N(D) dD \right] \quad (degree) \tag{2-18c}$$

where $\sigma_{h,v}$ are radar cross sections in horizontal and vertical polarization, $k = (\epsilon_r - 1)/(\epsilon_r + 2)$, "$Re$" states for the real parts and $\vec{f}(D)$ is the forward vector scattering amplitude.

The drop axis ratio (or, shape) is dependent on the equivalent spherical diameter, D. In steady air flow, the drop shape is determined by the balance of surface tension, gravity and aerodynamic force. A simple model given by Green (1975)[19] shows that the drop shape should be oblate and D is given by,

$$D = 2 \left(\frac{\sigma}{g \rho_w} \right)^{1/2} \frac{\left[(b/a)^{-2} - 2(b/a)^{-1/3} + 1 \right]^{1/2}}{(b/a)^{1/6}} \tag{2-19}$$

where σ ($72.25\ erg\ cm^{-2}$) is surface tension, g is the acceleration of gravity ($981\ cm\ s^{-2}$), ρ_w is the water density and (b/a) is the axis ratio (b is the semi-minor axis length and a is the semi-major axis length). Pruppacher and Beard (1970)[40] used a linear fit to their wind-tunnel data and showed that the relation between D and (b/a) could be simplified as,

$$\frac{b}{a} = 1.03 - 0.062D; \quad 1 \leq D \leq 8mm \tag{2-20}$$

Careful examination of drop images from aircraft-mount 2D imaging probes by Bringi et al. (1998)[10] showed that (b/a) was slightly larger than (2-20) when D was less than 3 mm and slightly smaller when D was great than 4.5 mm. Moreover, fields studies conducted by Tokay and Beard (1996)[51] showed that raindrops between 1 to 4 mm would oscillate in unsteady air flow. Drop oscillations can result in error in rain rate retrieval using K_{dp} (as well as other polarimetric data). In order to overcome this problem, Gorgucci et al. (1999, 2000)[16, 17] proposed an algorithm to estimate the mean shape of raindrops from the polarimetric measurements. They state that in (2-20), the slope of the linear fit should be a variable, β, instead of a constant (0.062 mm^{-1}). So β can be expressed as,

$$\beta = -\frac{dr}{dD} \tag{2-21}$$

where $r = (b/a)$. Note that $\beta > 0.062\ mm^{-1}$ means that raindrops are more oblate than equilibrium, and $\beta < 0.062$ means that they are less oblate. By computing Z_h, Z_{dr} and K_{dp} using the gamma dsd model with parameters varying as follows:

$$-1 < \quad \mu \quad < 4 \tag{2-22a}$$

$$10^{3.2+0.216\mu} < \quad N_0 \quad < 10^{4.5+0.55\mu} \tag{2-22b}$$

$$0.5 < \quad D_0 \quad < 2.5 \tag{2-22c}$$

and β is between 0.02 to 0.1, Gorgucci et al. (2000)[16] are able to express β at S-band as,

$$\beta = 2.08 \times Z_h^{-0.365} 10^{0.0965 Z_{dr}} K_{dp}^{0.380} \tag{2-23}$$

using non-linear fitting techniques. They also obtained a R-K_{dp} algorithm at S-band as,

$$R(K_{dp}) = 0.440 \beta^{-1.612} K_{dp}^{1.596\beta^{0.175}} \tag{2-24}$$

as well as a linear R-K_{dp} fit,

$$R(K_{dp}) = 0.57\beta^{-1.5}K_{dp} \tag{2-25}$$

To apply the β correction (which corrects the rain rate for unknown drop oscillations), first we find the R-K_{dp} relationship ($R(K_{dp}) = cK_{dp}$) with fixed β based on disdrometer data analysis. However, from simulations using disdrometer data, the β_{model} is a function of Z_{dr} and can be expressed as,

$$\beta_{model} = 0.0049\xi_{dr}^2 - 0.0043\xi_{dr} + 0.0433 \tag{2-26}$$

where ξ_{dr} is Z_{dr} in linear scale ($\xi_{dr} = 10^{0.1Z_{dr}}$). Next, we form the initial estimate of rainfall rate using $R = cK_{dp}$ (with c from Table 2.1). We also calculate β by using (2-23). From (2-25), we can calculate the corrected rainfall rate as,

$$R(K_{dp}, \beta) = (\frac{\beta_{model}}{\beta})^{1.5}cK_{dp} \tag{2-27}$$

Such a methodology can only be applied to events where the rain rate is sufficiently large so that Z_{dr} and K_{dp} data are reliable. It is one physically-based method for accounting for both drop oscillations as well as drop canting due to turbulence.

2.2 Error Structure and Comparison of Two Algorithm

From a statistical view point, any estimation procedure will result in error. In general, the relation between estimated rain rate ($\hat{R}$) and true rain rate (R) can be expressed as,

$$\hat{R} = R + \epsilon_p + \epsilon_m \tag{2-28}$$

and

$$var(\hat{R} - R) = \sigma^2(\epsilon_p) + \sigma^2(\epsilon_m) \tag{2-29}$$

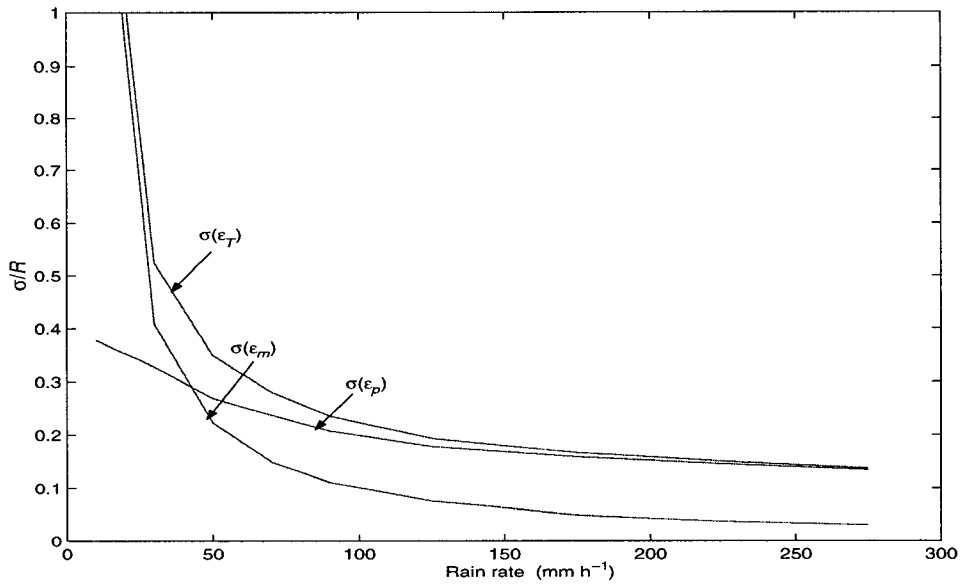

Figure 2.2: The normalized standard deviation of $R(K_{dp}) = aK_{dp}^b$; (σ/R) versus R for S-band radar.

where ϵ_p is the parametric error and ϵ_m is the measurement error (Bringi and Chandrasekar, 2001)[9]. Fig. 2.2 shows the $\sigma(\epsilon_p)$ and $\sigma(\epsilon_m)$ for $R = cK_{dp}^b$ algorithm versus rain rate based on simulations at S-band.

The parametric error is due to the parametric form of R. Since all radar parameters (Z_h, Z_{dr}, K_{dp} and so on) are functions of drop size distribution, canting angle distribution, axis ratio distribution, etc., the parameters are random variables and can change with time. When we used a fixed form to express the relation between $\hat{R}$ and radar data, e.g., $R = cK_{dp}^b$, we will induce parametric errors. According to the result in Fig. 2.2, the standard deviation of parametric error ($\sigma(\epsilon_p)$) is a function of rain rate and is around 27% on average for the R-K_{dp} algorithm. The measurement error (ϵ_m) is due to measurement fluctuations and can be reduced by averaging over area and time. Ryzhkov et al. give the measurement error for their areal rain algorithm (see, (2-30)) when integrated over time as (Ryzhkov et al. 2000)[44],

$$\sigma(\epsilon_m) = \frac{c\sigma_{\Phi_{dp}}}{L(2MJ)^{1/2}} \qquad (2\text{-}30)$$

where L is the number of gates for each beam, J is the total beams in the area, and M is the total number of sweeps in the observing period. Since this error is due to Φ_{dp} measurement fluctuations, it should be valid for the CSU algorithm given in (2-13), too. So we also used (2-30) to estimate the measurement error of $\bar{R}_{csu}$.

2.2.1 Computer Simulation of Additional Errors

Except for general errors discussed above, the two areal rain rate algorithms induce additional errors due to the assumptions involved. The CSU algorithm assumes that the R-K_{dp} relationship is locally linear. Actually, the R-K_{dp} relation at long wavelengths is not linear (Sachidananda and Zrnić, 1987)[45]. Even if piece-wise linear fitting is used, it still produces additional error. On the other hand, the Ryzhkov-Zrnić algorithm assumes that K_{dp} is constant along the radar beam. This assumption introduces two extra error components. First, the actual range profile of K_{dp} usually is not a constant over long path. Second, the range-weighting in (2-7) is constant at $(r_2 + r_1)/2$. However, the further resolution volumes will cover a larger polar area than nearer ones. So (2-7) will produce a range-weighting error.

In order to understand the effect of these additional error components on the two areal rain rate algorithms, we assume that the "true" rain rate is given $R = 32.4K_{dp}^{0.83}$ with 6 ideal K_{dp} profiles used to simulate the resultant errors. The 6 K_{dp} profiles are (see Fig: 2.3):

1. K_{dp} is constant and equal to $2^o\ km^{-1}$ over the range interval.

2. K_{dp} is linear increasing form 0^o to $2^o\ km^{-1}$ versus range.

3. K_{dp} profile is an isoceles triangle.

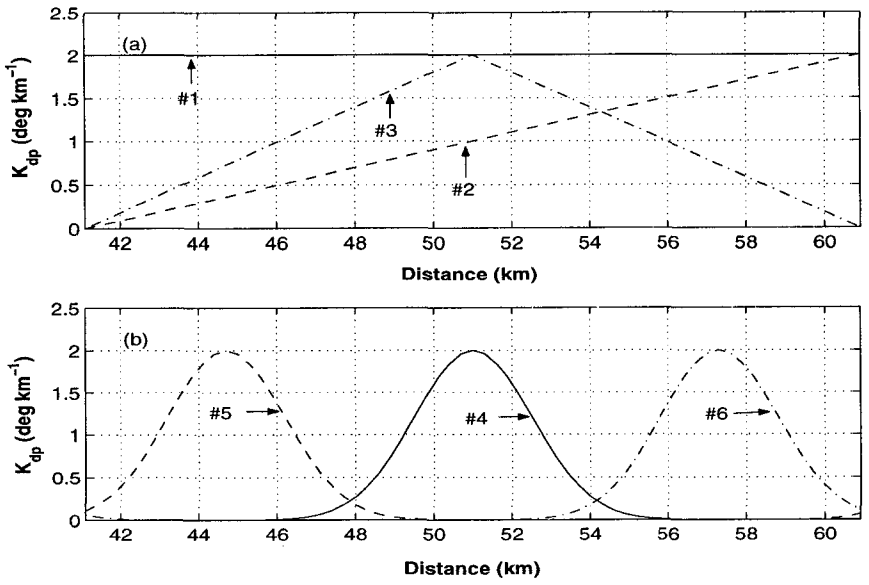

Figure 2.3: Illustrating the idealized K_{dp} profiles used for simulations,(a) Profiles marked 1 through 3, (b) Gaussian profiles marked 4 through 6.

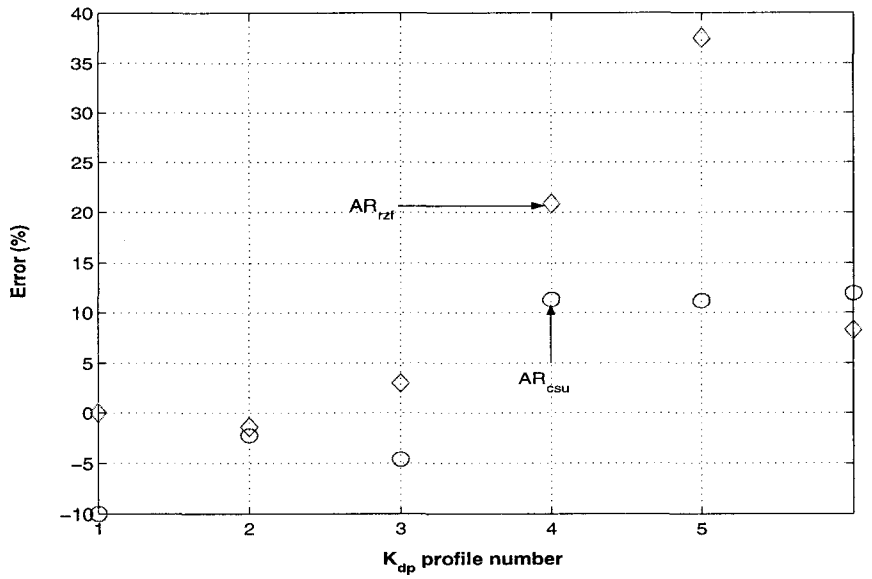

Figure 2.4: The percentage additional error for different areal rain rate algorithms (AR_{rzf} and AR_{csu}). The horizontal axis denote the different K_{dp} profiles (#1-#6).

4. K_{dp} is Gaussian in shape with σ of 1.5 km (5 gates). The peak K_{dp} is located at the center and equal to 2^o km^{-1}.

5. As in 4 except that the peak is located asymmetrically with respect to the center of the path interval.

6. As in 4 except that the peak is located asymmetrically as shown.

Fig. 2.4 shows the percentage error in AR_{csu} and AR_{rzf} versus the K_{dp} profile number. Apparently, AR_{rzf} is exact when K_{dp} is constant (e.g. profile #1) because this profile agrees with the assumption of the Ryzhkov-Zrnić algorithm. However, AR_{csu} has smaller error ($\leq 10\%$) than AR_{rzf} when K_{dp} profiles are Gaussian shape (profile #4-6). Moreover, the errors in AR_{csu} fluctuate between $\pm 10\%$ depending on the shape of K_{dp} and in AR_{rzf} seem to be one-sided. It implies that the error in AR_{csu} may be even smaller than simulations as actual K_{dp} profiles tend to be random in shape.

A further simulation has been performed to investigate the impact of range-weighting. Again, we assume the "real" rain rate follows the power law we mention above. We start with K_{dp} as profile #4 whose peak is located at the center of the profile path ($[r_1, r_2]$=[39.9,59.7] km, center at 49.8 km). The r_1 is fixed and r_2 expands from 59.7 km to 100 km with step of 0.15 km. The percentage error of AR_{csu} and AR_{rzf} versus $(r_2 - r_1)$ is shown in Fig. 6. As expected, the error in AR_{rzf} increases with $(r_2 - r_1)$. On the other hand, AR_{csu} is not sensitive to range-weighting and the error is bounded to $\leq 10\%$.

2.3 Case Study

In this section, we apply two different areal rain rate algorithms to data sets from two different radars. Both data sets include their own gage network. By comparing the estimated rain rate (R_{rzf} and R_{csu}) with gage rain rate (R_g, "g" refer to gage), we are able to examine the accuracy of these two algorithms.

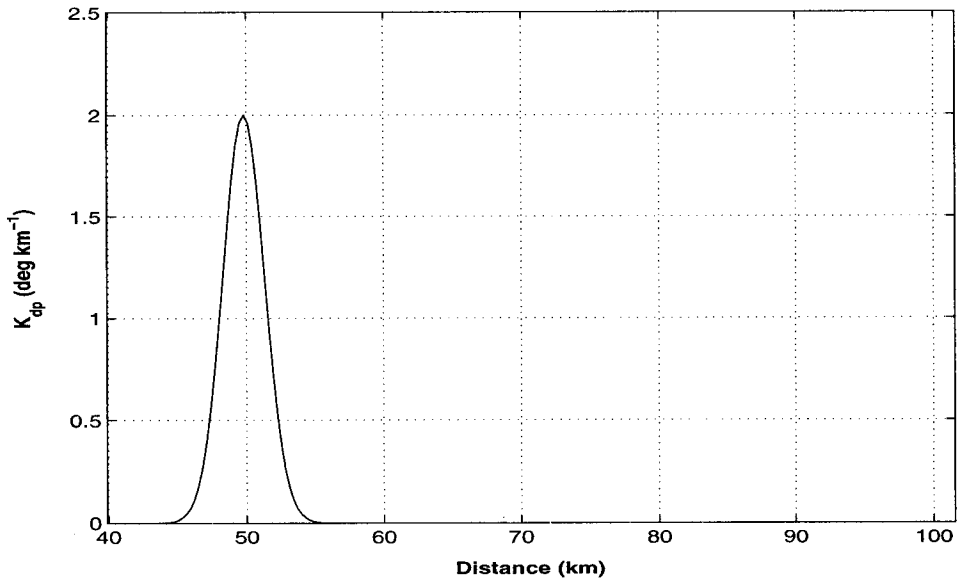

Figure 2.5: Illustrating the idealized K_{dp} profiles used to simulate the effect of range-weighting error.

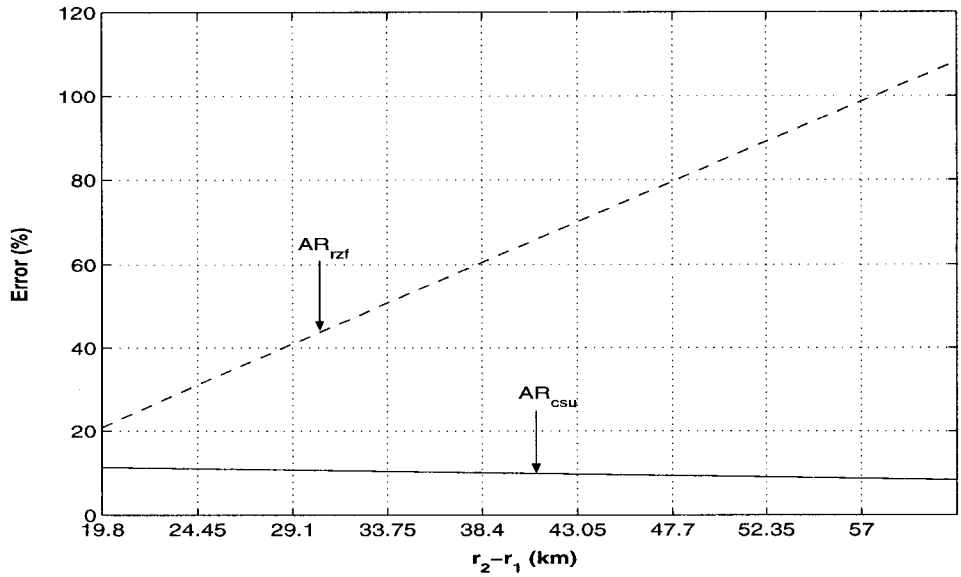

Figure 2.6: The percentage additional error for AR_{rzf} and AR_{csu} versus $(r_2 - r_1)$.

	BMRC C-POL
Peak Power	250 KW
Operating Frequency	5605 MHz
Pulse width	1.0 and 2.0 μs
Antenna Gain	45 dB
Beamwidth	1.0^o
Max. Range	600 km
PRF	200-1200 Hz
Polarization	Linear Horizontal and Vertical
Variables	Z_h, V_r, σ_v, Z_{dr}, Φ_{dp} and ρ_{hv}

Table 2.2: Specifications of the BMRC C-POL radar

2.3.1 C-band Data from Darwin

The C-POL radar[1] is located near Darwin, Australia and operated by the Bureau of Meteorology Research Center (BMRC) (Keenan et al. 1998)[30]. The specification of the C-POL radar is shown in Table 2.2. The D-scale gage network which is located about 40 km southeast of radar includes 20 gates in around 100 km^2 polar area. The gages are 203-mm-diameter tipping-bucket type and calibrated routinely to maintain the data quality (May et al. 1999)[35]. For each gage, 1-minute rain rates (R_g) were available. Also, a Joss disdrometer located in the network offered about 2000 2-minute average dsd data sets which includes different rain types for an entire wet season. These dsd data were used to estimate the coefficients of a piece-wise linear fit between K_{dp} and R (see Fig. 2.1).

The C-POL data includes Z_h, Z_{dr} and Φ_{dp}. Z_h and Z_{dr} are corrected for propagation attenuation by using a self-consistent, constraint-based method (Bringi et al. 2001a)[13]. The Φ_{dp} data are filtered in range with an adaptive filtering algorithm (Hubert et al. 1995) [25]. Since the fluctuations of filtered Φ_{dp} is less

[1]Please see the BMRC web page at www.bom.gov.au/ bmrc/wefor/research/scsmex.htm

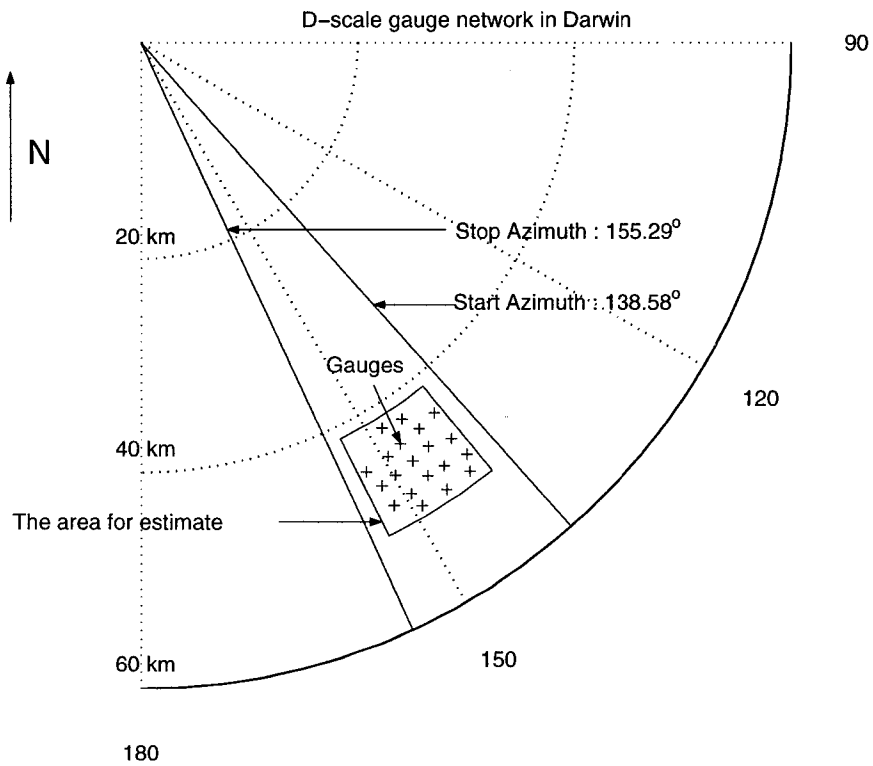

Figure 2.7: The location of D-scale gage network. Note that the C-POL radar is located at the origin.

than 1^o, we applied a threshold of $\Delta\Phi_{dp} = \Phi_{dp}(r_2) - \Phi_{dp}(r_1) > 2^o$ for each beam when using (2-11) and (2-13). The corresponding rain rate for this threshold is around 5 $mm\ h^{-1}$. For those beams below the threshold, a fixed Z_h-R relationship is applied to calculate the rain rate. The coefficient and exponent of the Z_h-R were determined from disdrometer data and is $Z_h = 305R^{1.36}$. The coefficients of a piece-wise linear fit between K_{dp} and R is shown in Table 2.1.

The radar data from the lowest available elevation tilt (0.5^o) were used to estimate the areal rain rate. Generally, there are 12-15 beams in the polar area in Fig. 2.7. A low elevation sweep was available every 10 minutes. So the time spacing for mean areal rain rate ($\bar{R}_{csu}$ and $\bar{R}_{rzf}$) was 10 minutes. Since the time resolution of gage (R_g, 1-minute time spacing) and radar (R_{scu} and R_{rzf}, 10-minute time spacing) is different, a 2-minute time window was applied. Let t_o be the radar sampling time. The gage rain rate ($\bar{R}_g(t_o)$) is estimated by averaging all R_g in the time window which is $t_0 \pm 1$ minute. Next, we applied a time delay by sliding the time window backward/forward in 1 minute intervals, and an optimal delay time was obtained by minimizing the absolute deviation between $\bar{R}_{csu}$ and $\bar{R}_g$. Generally, the optimal delay time was around 1 minute.

There were twelve events from Darwin, Australia that are analyzed here, 11 of them from 1998/1999 summer wet season (December 1998 - March 1999) and one from January 1998. We used normalized error (NE) and normalized bias (NB) to examine the validation of algorithms. The normalized error and normalized bias are defined as,

$$NE = \frac{(1/N)\sum_{i=1}^{N} |\bar{R}_{csu} - \bar{R}_g|}{(1/N)\sum_{i=1}^{N} \bar{R}_g} \tag{2-31a}$$

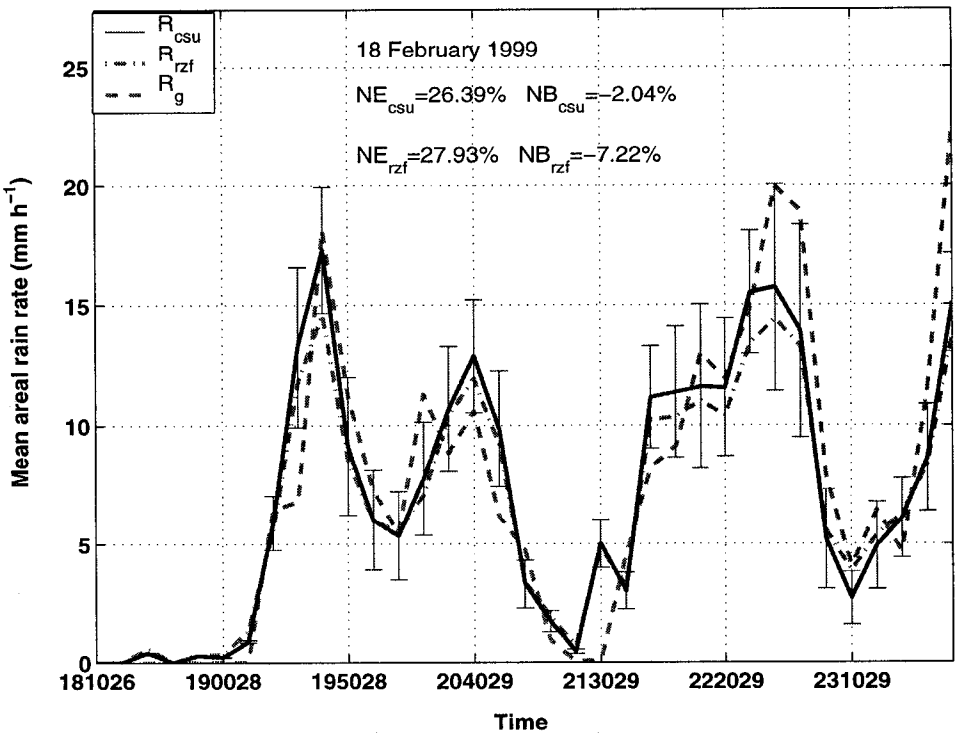

Figure 2.8: Mean areal rain rate of $\bar{R}_{csu}$, $\bar{R}_{rzf}$ and gage rain rate $\bar{R}_g$ versus time for the storm event of 18 February 1999. The error bar on $\bar{R}_{csu}$ includes both the parameterization error and measurement error.

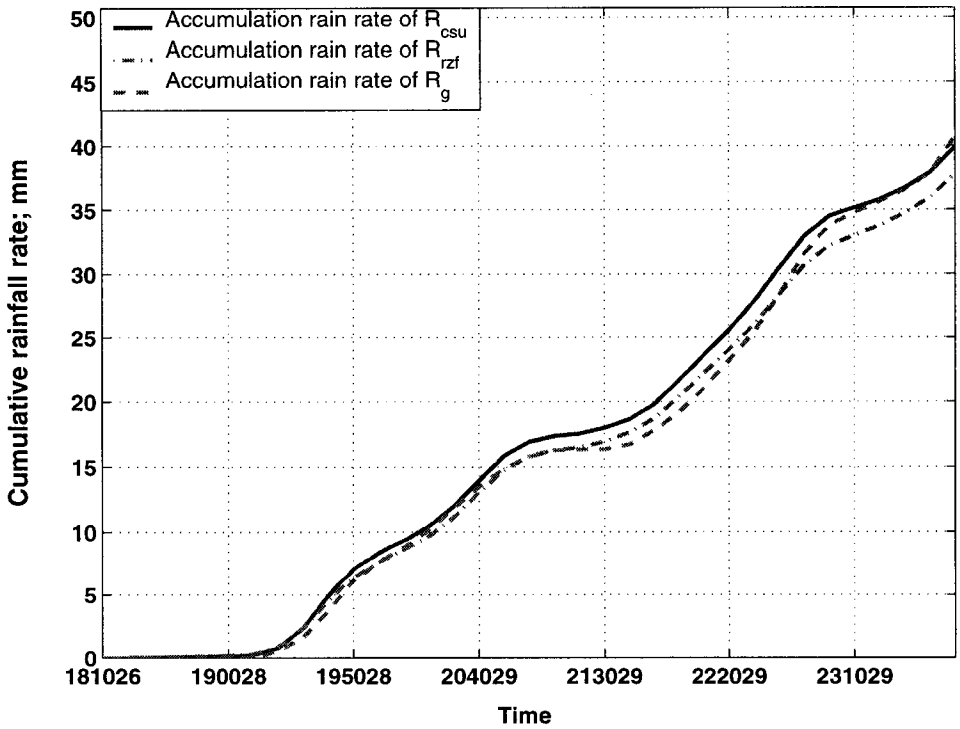

Figure 2.9: Accumulation rain rate of $\bar{R}_{csu}$, $\bar{R}_{rzf}$ and $\bar{R}_g$ versus time.

$$NB = \frac{(1/N)\sum_{i=1}^{N} \bar{R}_{csu} - \bar{R}_g}{(1/N)\sum_{i=1}^{N} \bar{R}_g} \tag{2-31b}$$

Fig. 2.8 and 2.9 show a typical time series of $\bar{R}_{csu}$, $\bar{R}_{rzf}$ and $\bar{R}_g$ and their accumulation from one event on 18 February 1999. The standard error bar on $\bar{R}_{csu}$ includes both parameterization error (ϵ_p) and radar measurement error (ϵ_m). Moreover, the error bar also accounts for the fact that the parameterization error has been reduced by the number of uncorrelated samples. This number is calculated as $(10/3)^2 \approx 11$, where $10 \times 10\ km^2$ is the area and $3\ km$ is a typical decorrelation distance for convective cells in this region (Maki et al. 1999)[32].

Table 2.3 shows the NE and NB for the 12 events. As expected, the two algorithms are high correlated, i.e., for those events where the CSU algorithm had lower NE and NB, the Ryzhkov-Zrnić formula also shows lower error. Fig. 2.10 compares $\bar{R}_{csu}$ with $\bar{R}_g$. The normalized error is 37% and normalized bias is 5%. Generally, the parameterization error (ϵ_p) is larger than the measurement error (ϵ_m) and is expected to be around $0.35/\sqrt{11} \approx 10\%$ where 0.35 is $\sigma(\epsilon_p)$ with $R \approx 20\ mm\ h^{-1}$ based on $R = cK_{dp}^{b}$ and 11 is the number of uncorrelated samples in the area mentioned above. So the error excluding parameterization error is around 27%. There are several possible sources which may account for the 27%, for example, (1) gage measurement error, (2) sampling error of the gage and (3) radar/gage sampling volume mismatch.

Fig. 2.11 compares rainfall accumulation from radar ($\bar{R}_{csu}$, $\bar{R}_{rzf}$ and R-Z_h) and gage ($\bar{R}_g$). The rain accumulation from gage is based on 10 minutes sampling and is averaged over 2 minutes interval. The normalized error is 14.1% for CSU and 21% for Ryzhkov-Zrnić estimator, and normalized bias is 5.6% for CSU and 11.4% for Ryzhkov-Zrnić. Because the sampling error of the gage network is expected to be around 5-7% (Silverman et al. 1981)[49], the results show that both CSU and

DATE	Delay Time (minute)	NE (%)	NB (%)
Jan. 02, 1998	0	55.22	12.60
		61.74	30.48
Dec. 09, 1998	1	26.12	-6.45
		34.29	14.84
Jan. 15, 1999	3	28.36	10.97
		39.11	25.36
Jan. 21, 1999	1	63.06	3.06
		65.51	3.24
Jan. 22, 1999	-1	58.93	-44.14
		59.05	-46.01
Feb. 09, 1999	2	64.82	-30.90
		63.91	-29.62
Feb. 18, 1999	1	26.39	-2.03
		27.93	-7.22
Feb. 19, 1999	1	12.58	3.58
		13.98	2.85
Feb. 25, 1999	-1	47.72	33.27
		46.63	34.84
Mar. 01, 1999	1	26.75	10.86
		25.69	11.45
Mar. 17, 1999	0	51.97	19.12
		67.81	39.36
Mar. 21, 1999	0	24.02	13.76
		20.85	12.08

Table 2.3: NE and NB of 12 events from Darwin, Australia. In each event, the first column is using the CSU algorithm and the second one is using the Ryzhkov-Zrnić algorithm.

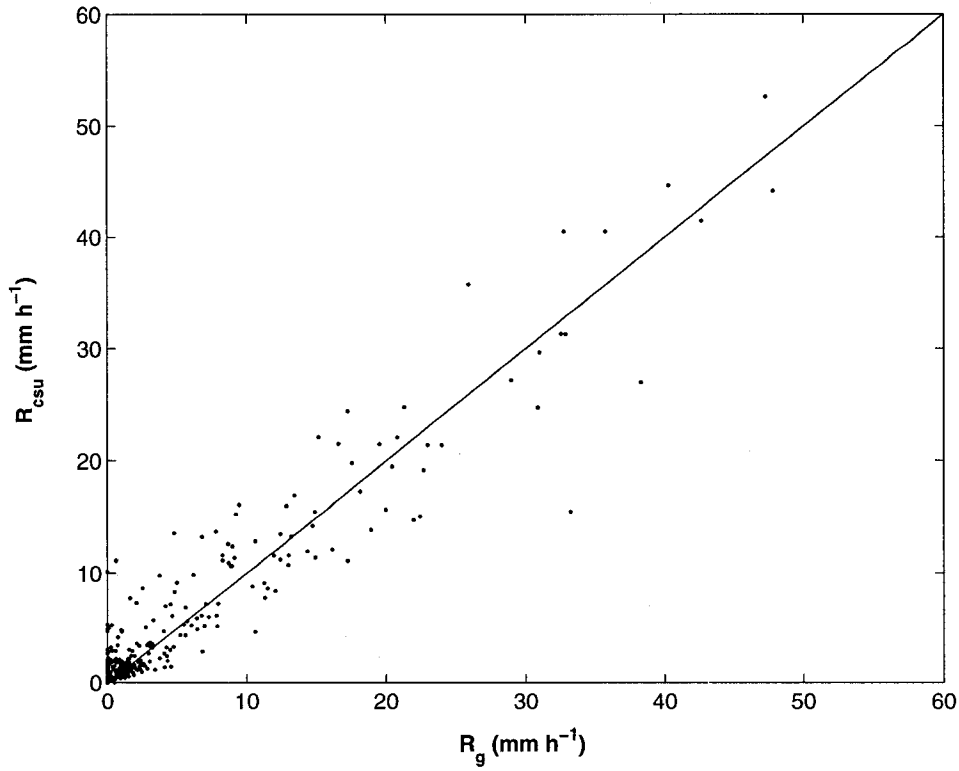

Figure 2.10: Scatterplot of $\bar{R}_{csu}$ versus $\bar{R}_g$ from 12 events. The normalized error is 37% and the normalized bias is 5%.

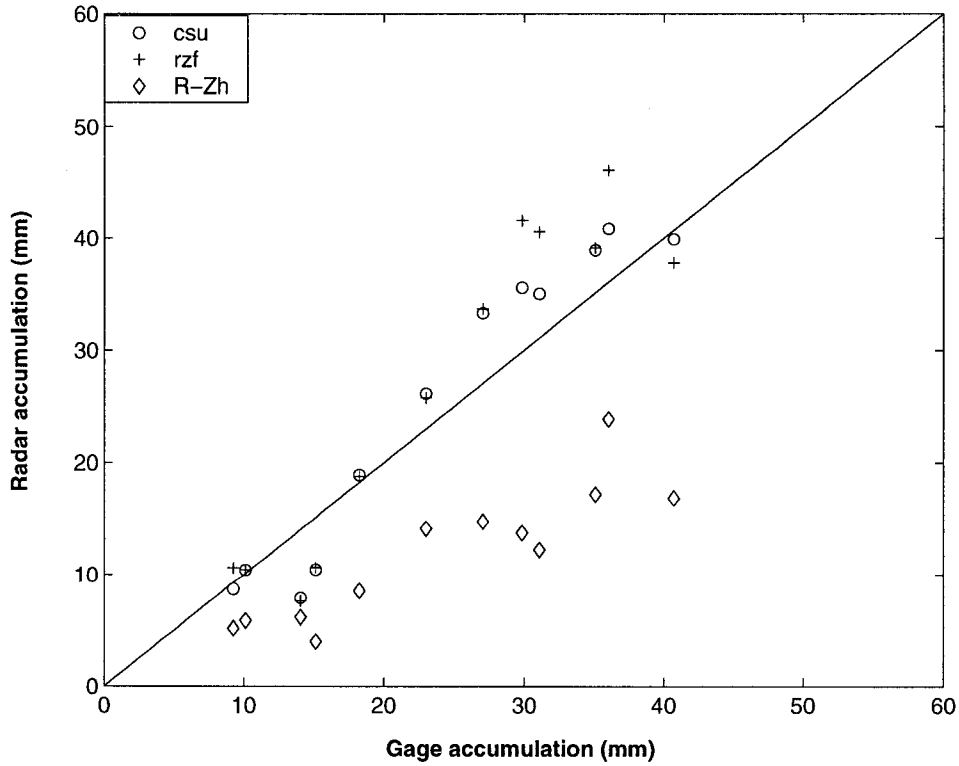

Figure 2.11: Rain accumulation from radar compared with gage network for 12 events. The normalized error is 14.1% and the normalized bias is 5.6% for CSU algorithm.

Gage Network #1 Ji Parana Airport	Gage Network #2 Ematar	Gage Network #3 Fazenda Triangula	Gage Network #4 Fazenda Sao Jose
43.6 $km/20^o$	54.2 $km/339^o$	79.3 $km/332^o$	115.7 $km/327^o$

Table 2.4: Approximate range/azimuth angle of 4 gage networks relative to the S-pol radar

Ryzhkov-Zrnić estimator are very accurate and much better than the fixed Z-R relation. Moreover, the results also show that CSU algorithm has less error than Ryzhkov-Zrnić algorithm which agrees with the simulation results (see Fig. 2.3 and 2.4).

2.3.2 S-band Data from Brazil

A field experiment which was supported by NASA/TRMM was held in Amazonia from 1 November 1998 to 28 February 1999. During this period, the NCAR S-pol radar was located at 11^o $13'$ 16.5" South and 61^o $59'$ 53.5" West. There were 4 sets of gages north of the S-pol radar. Each gage measured the rainfall rate and rain accumulation every minute. The range and azimuth of the 4 gage sets are shown in Table 2.4. The event we studied is focused on gage network #1 which was near Ji Parana Airport. The location of gage network #1 and the polar area used to estimate the areal rainfall rate are shown in Fig. 2.12.

On 15 February 1999, the S-pol radar observed a storm event that started around 01:00 (UTC). The first event hit gage network #1 around 03:45. From 04:21 to 07:13 (UTC), three events swept through the estimated area. Fig 2.13 shows the Z_h vs. Z_{dr} scatter plot from the low elevation angle data. The system Z_{dr} bias was estimated to be 0.15 dB (measured Z_{dr} was reduced by 0.15 dB). Fig 2.14 shows the R vs. K_{dp} scatter plot based on the Joss disdrometer data in Darwin, Australia and simulated at S-band. The simulation uses Andsager et al. model (1999)[1] for $1 < D < 4$ mm and Beard-Chuang model (1987)[7] for

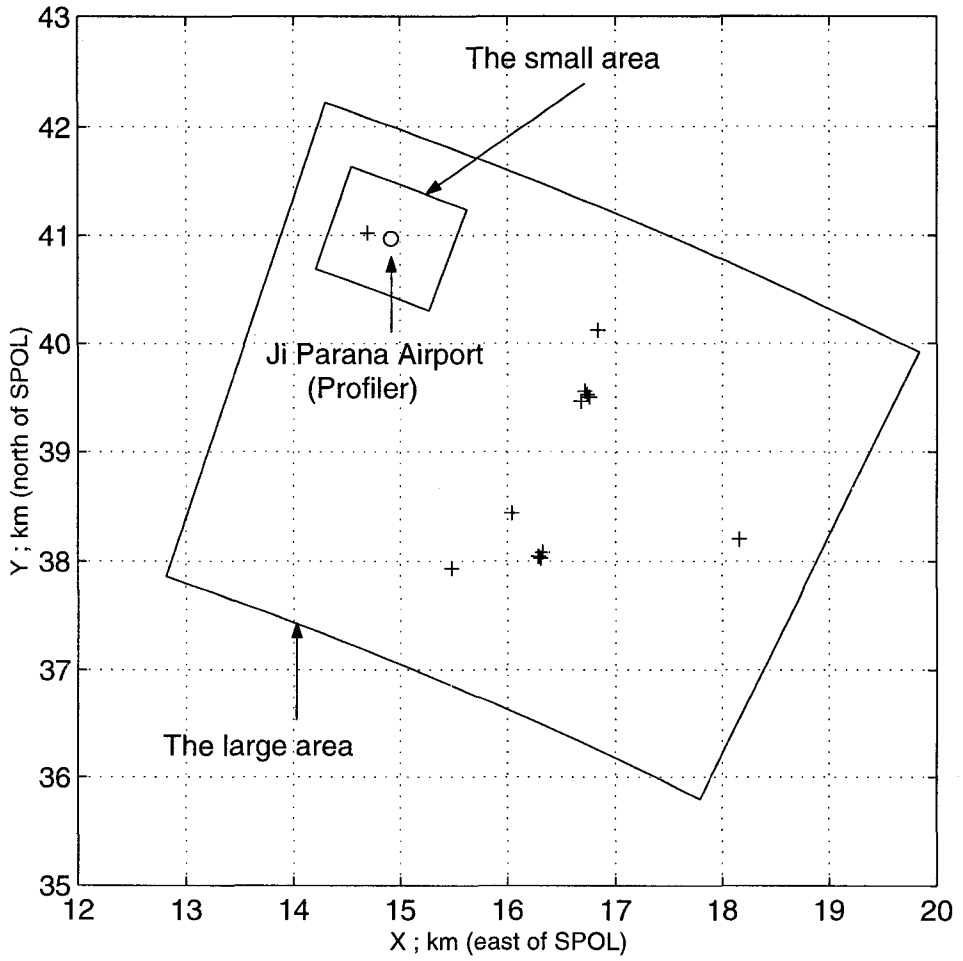

Figure 2.12: The location of gages in gage network #1. Note that S-POL radar is located at the origin of coordinates.

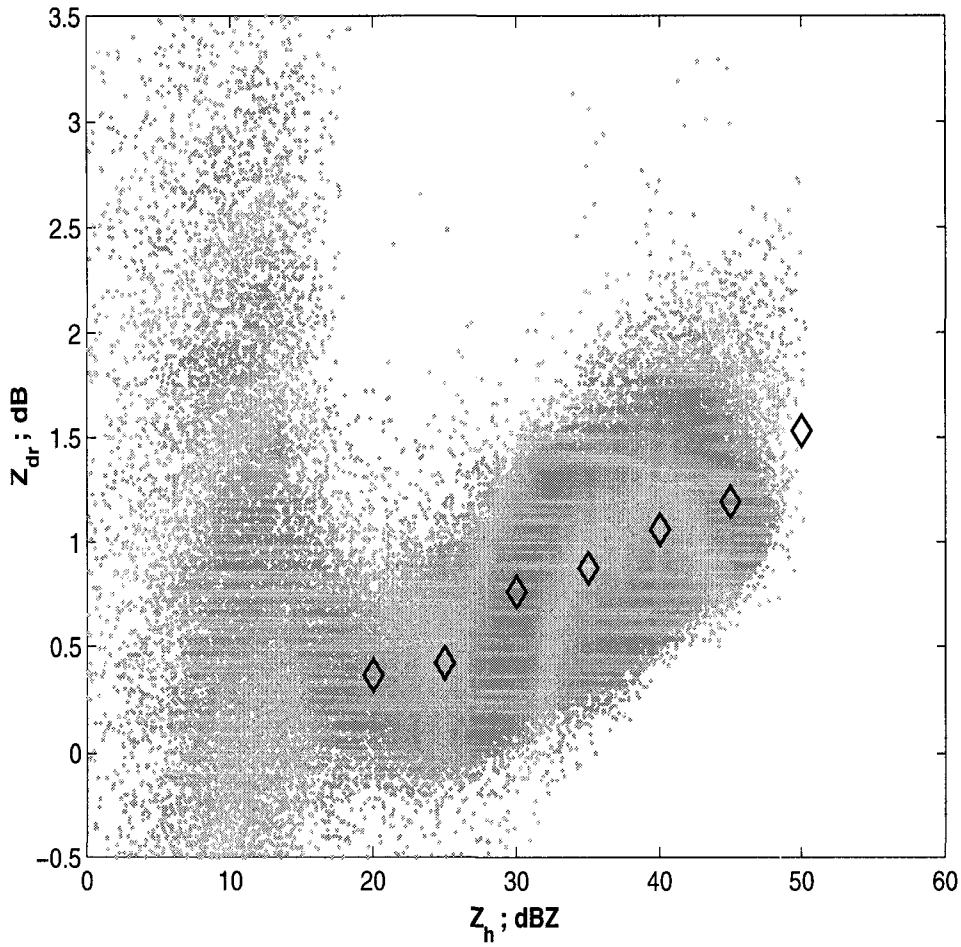

Figure 2.13: The Z_h vs. Z_{dr} scatter plot. Note that diamond shape dots show the mean Z_{dr} corresponding to Z_h in 5 dB intervals.

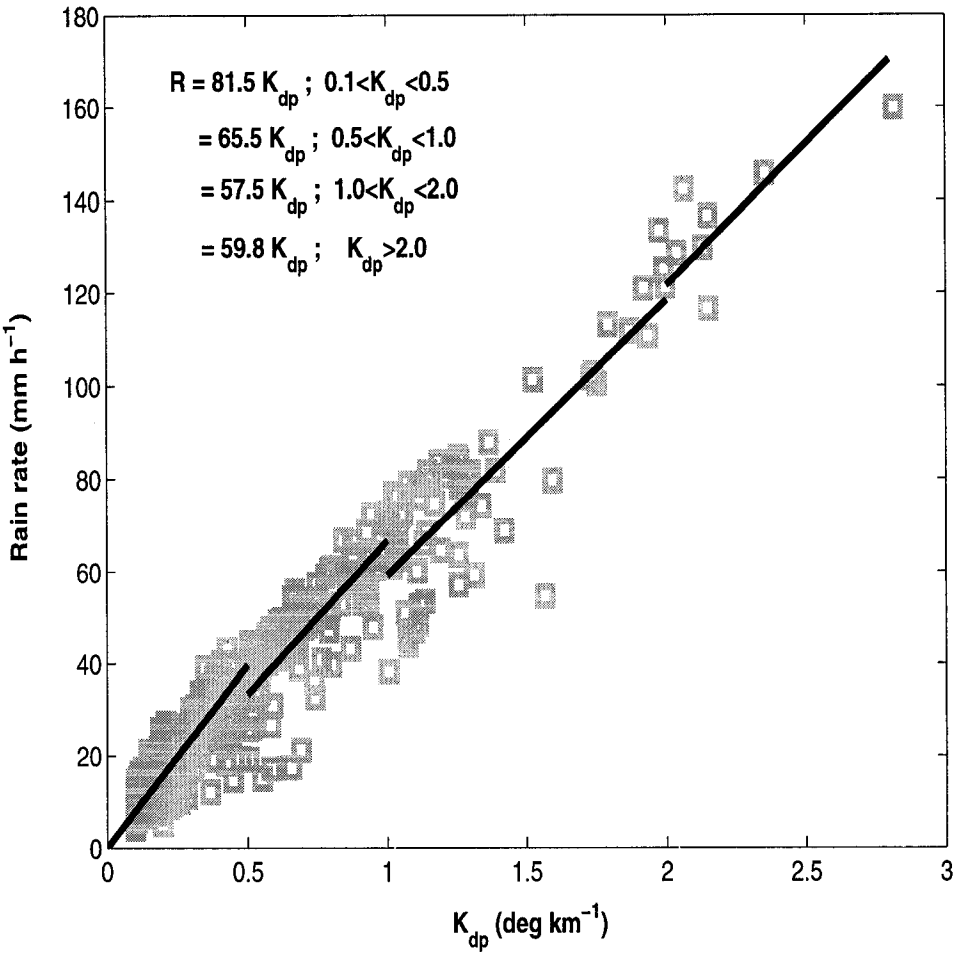

Figure 2.14: The R vs. K_{dp} scatter plot based on Darwin (Joss) disdrometer data and simulated at S-band. Note that dark solid lines are the piece-wise linear fit for S-band.

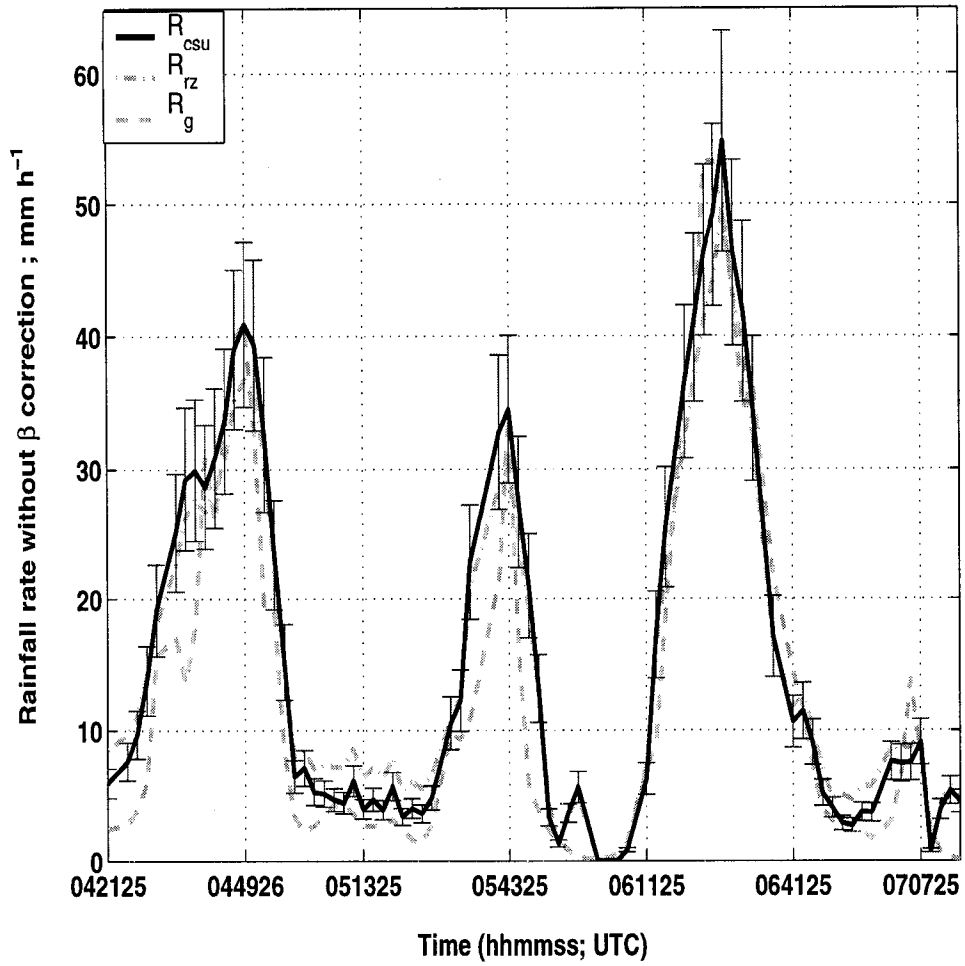

Figure 2.15: Time series of mean areal rain rate ($\bar{R}_{csu}$ and $\bar{R}_{rz}$) versus gage rain rate ($\bar{R}_g$) for the storm of 15 February 1999.

$D < 1$ or $D > 4$ mm. The canting angle model is assumed to be Gaussian with zero mean and 10^o standard deviation. By applying a piece-wise linear fit, we get the coefficients for R_{csu} which is shown in Table 2.1 whereas the non-linear R-K_{dp} relation is $R(K_{dp}) = 56.2K_{dp}^{0.8}$. The mode of β based on the same simulation is 0.0450 and this value would be the default β.

In this case, the radar sampling interval was not uniform (the minimum was 11 seconds, the maximum was 375 seconds and typical value was 33 seconds) whereas the rain gages recorded rain rate every minute. In order to compare R_g with radar estimates (R_{csu} and R_{rzf}), we first calculated R_{csu} and R_{rzf} by applying

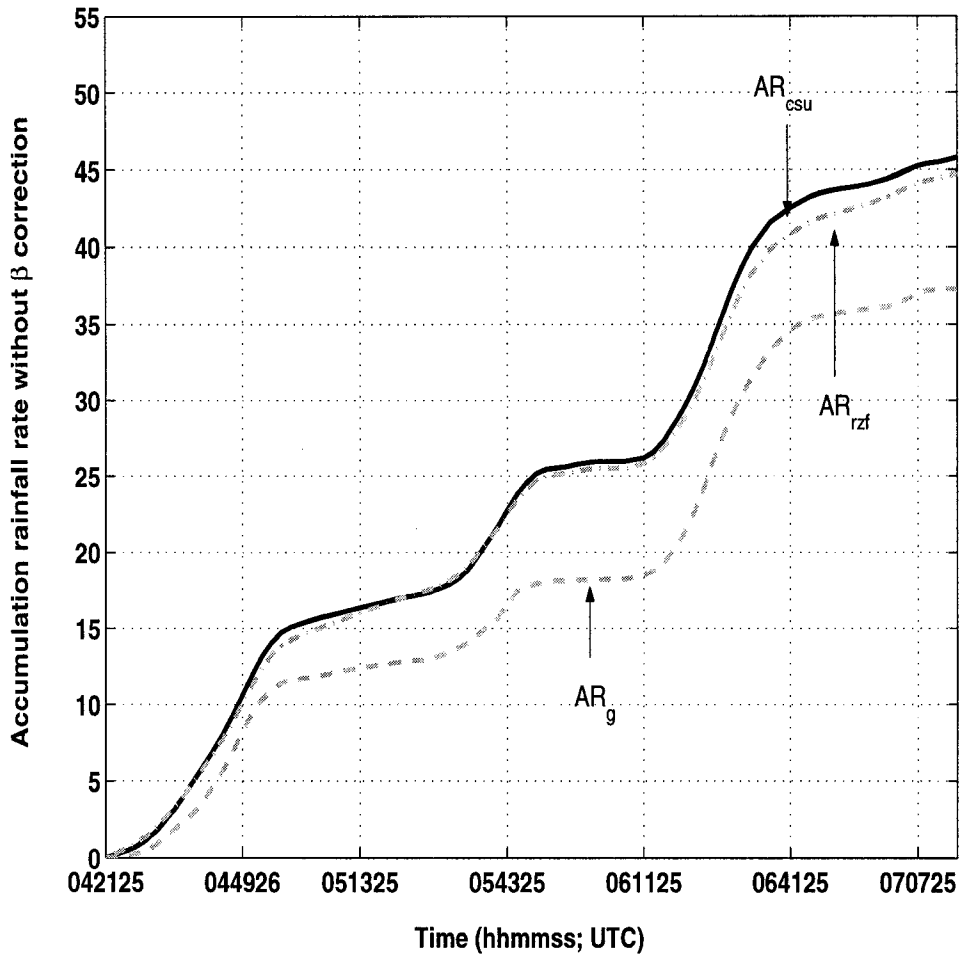

Figure 2.16: The comparison of rain accumulation over the estimated area.

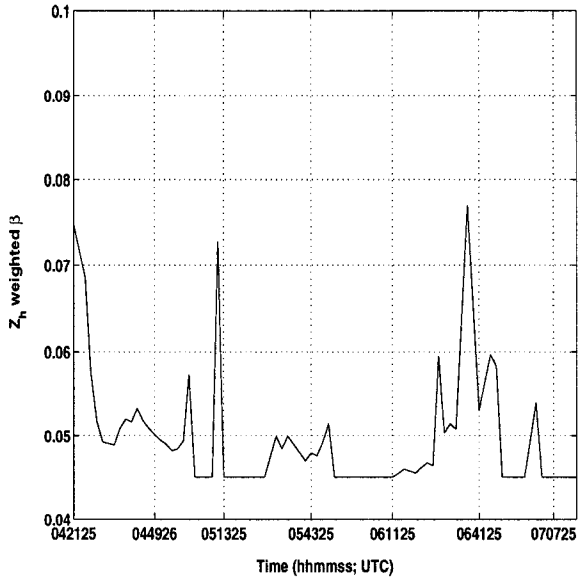

Figure 2.17: The effective β vs. time.

(2-13) and (2-11) in each radar sweep. Next, we divided whole duration time (from 04:22:26 to 07:14:26) into 77 2-minutes intervals $(t_1, t_2 \cdots t_{77})$. Finally, we computed $\bar{R}_{csu,rzf}(t_n)$ by averaging $R_{csu,rzf}$ over $t_n \pm 1$ minutes interval where n is $1 \leq n \leq 77$. To calculate gage rain rate, a time delay, τ, is introduced as we did for C-band data (see Section 2.3.1). The $\bar{R}_g(t_n)$ is averaged R_g over $t_n + \tau \pm 1$ minutes interval. In this case, optimal time delay was found to be 3 minutes. Fig. 2.15 shows the radar estimated areal rain rate and gage areal rain rate versus time. The normalized error (NE) is 30.01% for CSU estimator and 34.38% for Ryzhkov-Zrnić algorithm. Fig. 2.16 shows the comparison of rain accumulation over the estimated area. The normalized bias (NB) is 22.87% for CSU estimator and 20.10% for Ryzhkov-Zrnić algorithm.

As mentioned above, the radar sampling interval is 33 seconds. There are around 3 or 4 sweeps in a 2-minute interval. This higher time resolution comparing to C-band data (10 minutes per sweep) allowed us to estimate β for each 2-minute interval. In order to estimate β, we set the threshold as $Z_h \geq 30\ dBZ$, $Z_{dr} \geq 0.5\ dB$ and $K_{dp} \geq 0.1\ ^o/km$. First, we calculate β for all resolution volumes which

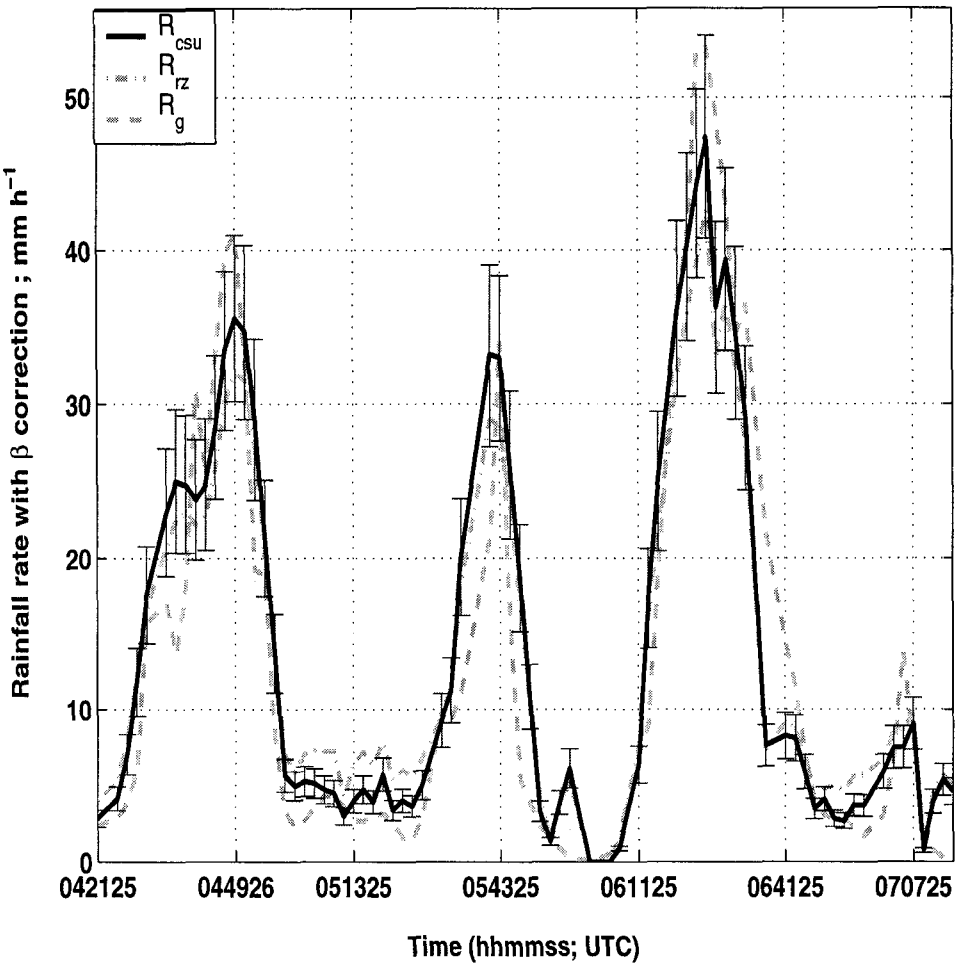

Figure 2.18: The radar areal rainfall rate after β correction.

	Normalized Error	Normalized Bias
CSU Estimator without β correction	30.01%	22.87%
CSU Estimator with β correction	28.74%	7.87%
Ryzhkov-Zrnić Estimator without β correction	34.38%	20.10%
Ryzhkov-Zrnić Estimator with β correction	34.84%	5.31%

Table 2.5: The normalized error and bias for the storm event of 15 February 1999.

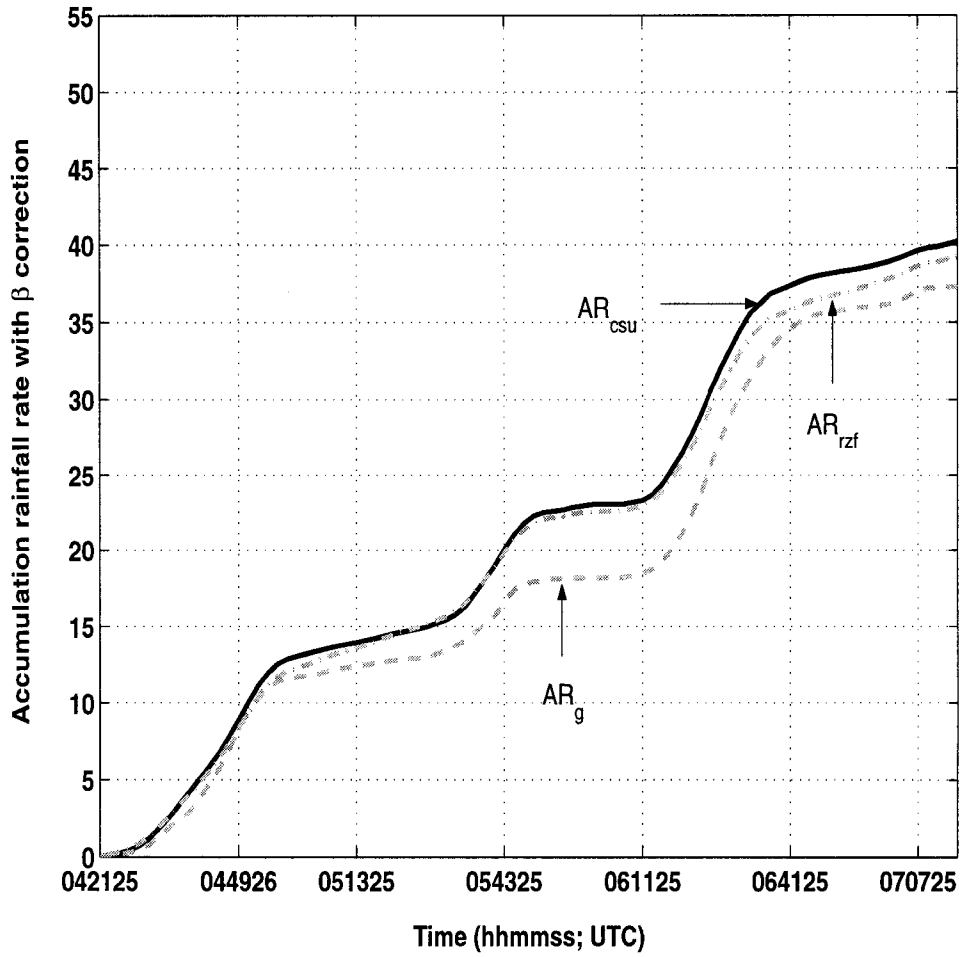

Figure 2.19: The rainfall accumulation after β correction

satisfy threshold by using (2-23). Second, in any time interval whose center time is t_n, $\beta(t_n)$ is the mode of β. If amount of qualified βs (satisfied threshold) in the time interval are less than one tenth of total amount of resolution volumes available in the time interval, we let $\beta = 0.0450$ (default value for tropical rain). Fig. 2.17 shows β versus time and Fig. 2.18 and 2.19 show the rainfall rate and rain accumulation compared with gage data after β correction. The NE and NB are in Table 2.5. The NB of CSU estimator reduces from 22.87% to 7.87% and the NB of Ryzhkov-Zrnić estimator reduces from 20.10% to 5.31%. The NE improves slightly (around 1.3%). As expected, the Ryzhkov-Zrnić estimator is more accurate comparing with the Darwin case because the integrated path is shorter (4.6 km in Brazil and 10 km in Darwin). These results show that β correction can improve NB significantly by reducing the bias between R_{csu} and R_g.

2.4 Summary

In this chapter, an areal rain rate algorithm is proposed based on differential phase shift (Φ_{dp}). This algorithm assumes a "locally" linear R-K_{dp} relation to simplify the formula. However, the actual R-K_{dp} relation is non-linear and follows a power law. In order to reduce the bias due to linear fit, we suggest using a piece-wise linear fit by carefully selecting K_{dp} segments. Moreover, we compare the CSU estimator with another areal rain rate algorithm proposed by Ryzhkov-Zrnić which assumes that K_{dp} is constant over the range segment but uses the power law R-K_{dp} relation. Both simulations and case study analysis show that the CSU algorithm lead to less error than Ryzhkov-Zrnić the algorithm.

In addition, we also consider the bias introduced due to drop oscillations by considering the β correction, where β is the slope of axis ratio versus equi-volume diameter of drops (Gorgucci et al. 2000)[17]. The S-band radar data have sufficient high time resolution and we found that we can apply the β correction on an areal

basis. The results show that β correction can reduce the bias in rain rate estimation significantly. More details of the β adjustment procedure will be discussed in the next chapter.

Chapter 3

ESTIMATION OF GAMMA RAIN DROP SIZE DISTRIBUTION PARAMETERS BY POLARIMETRIC RADAR

The drop size distribution (dsd) model directly connects to the microphysical properties of precipitation. Therefore, any physically-based rain rate algorithm based on radar observations has to consider the dsd model. The dsd model varies spatially and temporally within a storm event and it also varies in different storm types and climatic regimes. Traditionally, surface disdrometers and aircraft imaging probes are used to collect dsd data. By analyzing dsd data and combining with radar observables, it is possible to derive algorithms for retrieval of the dsd parameters. Since radar observations can offer not only high spatial and temporal resolution but also large areal coverage, it is important to develop radar-based algorithms for retrieving the dsd parameters.

There are two commonly used dsd models, namely, exponential distribution (with parameters N_o and Λ; Marshall and Palmer 1948)[34] and gamma distribution (with parameters N_o or N_w, D_o or D_m and μ, Ulbrich 1983; Willis 1984; Testud et al. 2001)[54, 57, 50]. In early dsd studies, researchers focused on the relation between D_o (or D_m) and Z_{dr} (Seliga and Bringi 1976; Aydin et al 1987; Bringi et al. 1998)[47, 6, 10]. It is well known that the functional relation between D_o and Z_{dr} is related to the mean axis ratio (r) versus drop diameter (D) relation and it is also true of the relation between rain rate and K_{dp}. The axis ratio in

steady air flow is related to its terminal velocity, surface tension and gravity (see Section 2.1.3), and is a function of the equivalent spherical diameter (D). Equation (2-20) shows a linear fit to wind-tunnel data by Pruppacher and Beard (1970)[40]. The actual shape of drops in unsteady air flow is different. Field studies conducted by Tokay and Beard (1996)[51] show that drop sizes from 1 to 4 mm will oscillate. Moreover, with wind shear and turbulence , the canting angle may be non-zero. These effects tend to force the axis ratio to be more spherical. In order to overcome the effects of axis ratio and drop orientation, Gorgucci et al. (2000, 2001, 2002) [17, 18, 14] suggested that the total effect of drop shapes (oscillation and turbulence) will bias the axis ratio and the relation between mean axis ratio (r) versus drop size (D), but it is possible to get a linear model for the relation by defining a effective slope (β_{eff}) of r versus D. The effective slope can be estimated by the radar measurement set (Z_h, Z_{dr} and K_{dp}). Based on this theory, we can extend the application to estimate gamma dsd parameters (N_w, D_o and μ).

Although we can estimate dsd parameters by using radar measurement set and β, at low rain rates, however, the Z_{dp} and K_{dp} tend to be very noisy. In this case, the effective β can not be used to retrieve dsd parameters. However, Z_{dr} and K_{dp} data may still be available by averaging these data spatially to reduce the noise. By assuming that μ is equal to zero (averaging dsd data over a longer period will tend to exponential distribution), we may convert radar measurements to dsd parameters. To examine the validation of our algorithms, we compare the retrieved dsd data with NOAA profiler data. Moreover, we can estimate the coefficient of a Z-R relationship and compare with gage data.

3.1 Theoretical Basis

3.1.1 Drop Size Distribution

Consider rain drops inside a resolution volume with different equivalent spherical diameters (D) which can be expressed as (2-19). We divide D into several

diameter intervals ($D - \Delta D$,$D + \Delta D$) and count the number ($N(D)$) of drops whose diameter are inside the corresponding interval. The functional relation of $N(D)$ versus D is known as drop size distribution (dsd) and can be written as,

$$N(D) = n_c f_D(D) \tag{3-1}$$

where n_c is concentration and $f_D(D)$ is pdf of drop diameters. A commonly used form of $N(D)$ is the exponential distribution and can be expressed as,

$$N(D) = N_o exp(-\Lambda D) \tag{3-2}$$

where Λ is the slope of exponential distribution and is related to median volume diameter (D_o). The D_o is defined as those raindrops with diameters less than D_0 that contribute to half of total water content (W),

$$\frac{\pi}{6}\rho_w \int_0^{D_0} D^3 N(D) dD = (\frac{1}{2})\frac{\pi}{6}\rho_w \int_0^{\infty} D^3 N(D) dD = \frac{1}{2}W \tag{3-3}$$

where ρ_w is water density and $\Lambda D_o = 3.67$. Exponential dsd usually arises when dsd data are averaged spatially or temporally. A gamma distribution can represent the "instantaneous" dsd model and written as (Ulbrich, 1983)[54],

$$N(D) = N_o D^{\mu} exp(-\Lambda D) \qquad ; \mu > -1 \tag{3-4}$$

where $\Lambda D_o = 3.67 + \mu$ and μ is the shape parameter. This form is un-normalized.

The other parameter which plays the same role as D_o is mass-weighted mean diameter (D_m) and defined as,

$$D_m = \frac{\int D^4 N(D) dD}{\int D^3 N(D) dD} \tag{3-5}$$

It is ease to show that $\Lambda D_m = 4 + \mu$ and the relation between D_o and D_m is,

$$D_o = \frac{3.67 + \mu}{4 + \mu} D_m \tag{3-6}$$

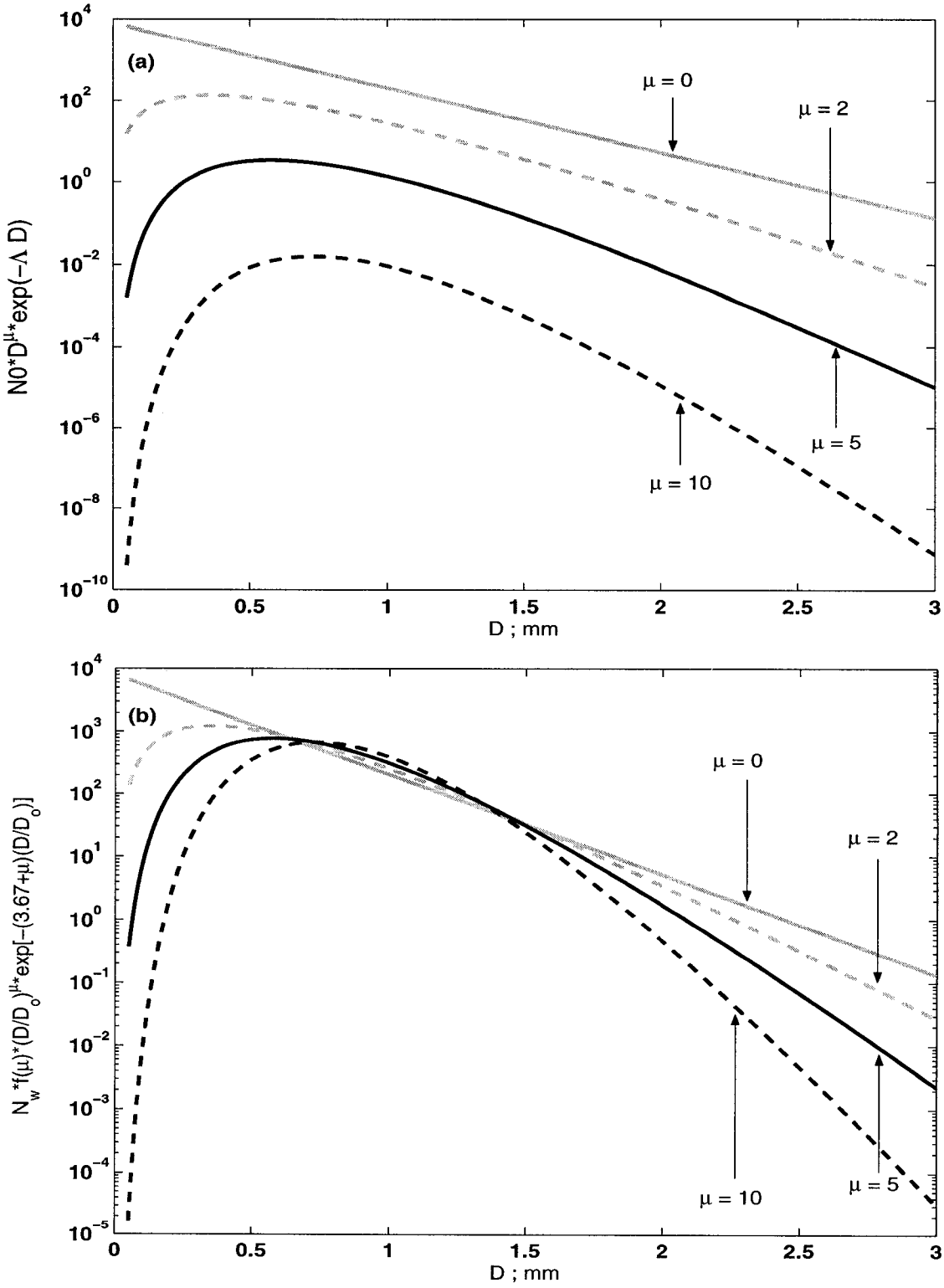

Figure 3.1: Two gamma dsd forms with $\mu = 0$, 2, 5 and 10. **(a)** gamma dsd form suggested by Ulbrich (1983, also see (3-4)) where $N_0 = 8000\ mm^{-1-\mu}\ m^{-3}$ and $D_0 = 1\ mm$. **(b)** Gamma dsd form suggested by Willis (1984, also see (3-7)) where $N_w = 8000\ mm^{-1}\ m^{-3}$ and $D_o = 1\ mm$.

From (3-4), it is obvious that the unit of N_o depends on μ. If we fixed N_o and D_o and changed μ, the shape parameter, the plots of $N(D)$ versus D would be as shown in Fig. 3.1a (Illingworth et al. 1999)[26]. Willis (1984)[57] proposed a normalized gamma form which uses normalized diameter (D/D_o) and normalized intercept parameter by water content. The normalized gamma distribution can be expressed as,

$$N(D) = N_w f(\mu)(\frac{D}{D_o})^{\mu} exp\left[-(3.67+\mu)\frac{D}{D_o}\right] \tag{3-7}$$

where N_w is the "new" intercept parameter and $f(\mu)$ is,

$$f(\mu) = \frac{6}{(3.67)^4}\frac{(3.67+\mu)^{\mu+4}}{\Gamma(\mu+4)} \tag{3-8}$$

Note that $f(0) = 1$ and (3-7) will reduce to (3-2).

3.1.2 Dsd Parameter Retrieval

As shown in Section 2.1.3, all radar parameters, including Z_h, Z_{dr} and K_{dp}, can be expressed as moments of the dsd (see (2-18)). In the Rayleigh scattering limit, Z_h is related to the 6th moment of dsd, Z_{dr} is related to the reflectivity-weighted mean axis ratio, and K_{dp} is related to the product of the water content (W) and the deviation of mass-weighted mean axis ratio from unity (Jameson 1983, also see Chapter 7 of Bringi and Chandrasekar 2001)[27, 9]. Moreover, if the relation between mean axis ratio versus D is fixed, then Z_{dr} can be related to reflectivity-weighted mean diameter of the dsd, and K_{dp} can be related to the product of water content and D_m (or D_o). Although the relation between axis ratio and D is non-linear when we consider the drop oscillations (due to resonance maintained by vortex shedding or collisions) and canting (due to turbulence), an equivalent linear model can be proposed as,

$$r = b/a = 1.03 - \beta_{eff} D \tag{3-9}$$

where β_{eff} is an "effective" slope parameter. Note that given the product of W and D_m and adjusted β_{eff}, the equivalent linear model will result in the same K_{dp} as the actual model. Gorgucci et al. (2000)[17] found that the effective slope can represent the net effect of drop oscillations and canting. They have developed an algorithm to calculate β from Z_h, Z_{dr} and K_{dp} (see (2-23)). In Chapter 2, we also showed that rainfall rate estimation can be improved significantly by using β correction.

Extending the application of β, Gorgucci et al. (2001, 2002)[18, 14] developed several algorithms to retrieve N_w, D_o and μ from β and the radar measurement set (Z_h, Z_{dr} and K_{dp}). We summarize their work briefly as follows: In the early research of Gorgucci et al. (1994)[15], the D_o was expressed as,

$$D_o = a_1 Z_h^{b_1} (\xi_{dr})^{c_1} \tag{3-10}$$

Noted that ξ_{dr} is Z_{dr} in linear scale ($\xi_{dr} = 10^{0.1 Z_{dr}}$). Apply a gamma dsd model with parameters that vary randomly over following range :

$$0.5 \leq \quad D_o \quad \leq 3.5; \quad mm \tag{3-11a}$$

$$3 \leq \quad log_{10} N_w \quad \leq 5 \tag{3-11b}$$

$$-1 \leq \quad \mu \quad \leq 5 \tag{3-11c}$$

and a equivalent linear axis ratio model with β varying between extreme values of 0.02 to 0.1 mm^{-1}. Once the dsd and axis ratio model were selected, they computed Z_h, Z_{dr} and K_{dp} directly, and then used nonlinear regression analysis to estimate coefficients (a_1) and exponents (b_1 and c_1) of (3-10). The results at S-band are,

$$a_1 = 0.56 \tag{3-12a}$$

$$b_1 = 0.064 \tag{3-12b}$$

$$c_1 = 0.024\beta^{-1.42} \tag{3-12c}$$

Similarly, the normalized intercept parameter is given as,

$$log_{10}N_w = a_2 Z_h^{b_2}(\xi_{dr})^{c_2} \quad (3\text{-}13a)$$

$$a_2 = 3.29 \quad (3\text{-}13b)$$

$$b_2 = 0.058 \quad (3\text{-}13c)$$

$$c_3 = -0.023\beta^{-1.389} \quad (3\text{-}13d)$$

After D_o is estimated, the shape parameter was estimated as,

$$\mu = \frac{a_3 D_o^{b_3}}{(\xi_{dr}-1)} - c_3(\xi_{dr})^{d_3} \quad (3\text{-}14a)$$

$$a_3 = 203\beta^{1.89} \quad (3\text{-}14b)$$

$$b_3 = 2.23\beta^{0.0388} \quad (3\text{-}14c)$$

$$c_3 = 3.16\beta^{-0.046} \quad (3\text{-}14d)$$

$$d_3 = 0.374\beta^{-0.355} \quad (3\text{-}14e)$$

Note that the thresholds using here are $Z_h > 35\ dBZ$, $Z_{dr} > 0.2\ dB$ and $K_{dp} > 0.3\ ^o/km$.

At low rain rates, the Z_{dr} and K_{dp} are known to be very noisy. Therefore, we cannot estimate β by using (2-23). Subsequently, we are not able to estimate dsd parameters. In order to retrieve dsd parameters at low rain rates (those radar measurements sets that do not satisfy the threshold), we have developed other algorithms which do not depend on β (i.e. a fixed β-value is assumed).

During TRMM/Brazil field campaign, dsd data from a 2D-video disdrometer and a RD-69 were available. These two instruments and a NOAA profiler (a 915 MHz vertically pointing Doppler radar) were located close to each other at Ji Parana Airport. Due to the technical difficulties, the 2D-video disdrometer was

not operating continuously in the field campaign but limited data were available in both convective rain (164 two minute-averaged dsd samples) and stratiform rain (49 two minute-averaged samples). The classification of rain type was based on manual examination of profiler reflectivity/velocity images. On the other hand, the RD-69 disdrometer was operated more or less through whole field campaign. In this research, the RD-69 data was used only when 2D-video disdrometer data was also available. A comparison between these two instruments is available in Tokay et al. (1999) and Williams et al. (2000)[52, 56]. These studies show that the D_m and R from two instruments at low rain rates ($Z_h < 40\ dBZ$) are in very good agreement. Small drops measured by 2D-video disdrometer can be affected by wind (Nespor et al. 2000)[39]. So we carefully examined the spatial distribution of drops across the sensor area to make sure the 2D-video data was not distorted due to wind. In addition, we also apply a terminal velocity filter which will reject any data whose terminal velocity exceeds a specified "band" around the theoretical value ($v(D) = 9.65 - 10.3exp(-0.6D)\ m\ s^{-1}$; Atlas et al. 1973)[4].

In the following analysis, only 2D-video data were used in convective rain and both 2D-video and RD-69 data were used in stratiform rain to increase the sample size. The gamma dsd parameters set, (N_w, D_m, μ), are estimated by using the procedure suggested by Bringi et al. (2000a)[12] and briefly summarized as follows:

1. Calculate the water content (W; $g\ m^{-3}$) and mass-weighted mean diameter (D_m; mm) from dsd measured data.

2. Compute N_w as $N_w = (256/\pi)(10^3 W/D_m^4)$.

3. Construct normalized gamma dsd form as $N_{norm}(D_i/D_m) = N_{meas}(D_i/D_m)/N_w$ and estimate μ by minimizing the error function expressed as,

$$Error = \min_{-3 \le \mu \le 15} |log_{10} N_{norm}(x_i) - log_{10}[f(\mu) x_i^{\mu} exp - (4+\mu) x_i]| \quad (3\text{-}15)$$

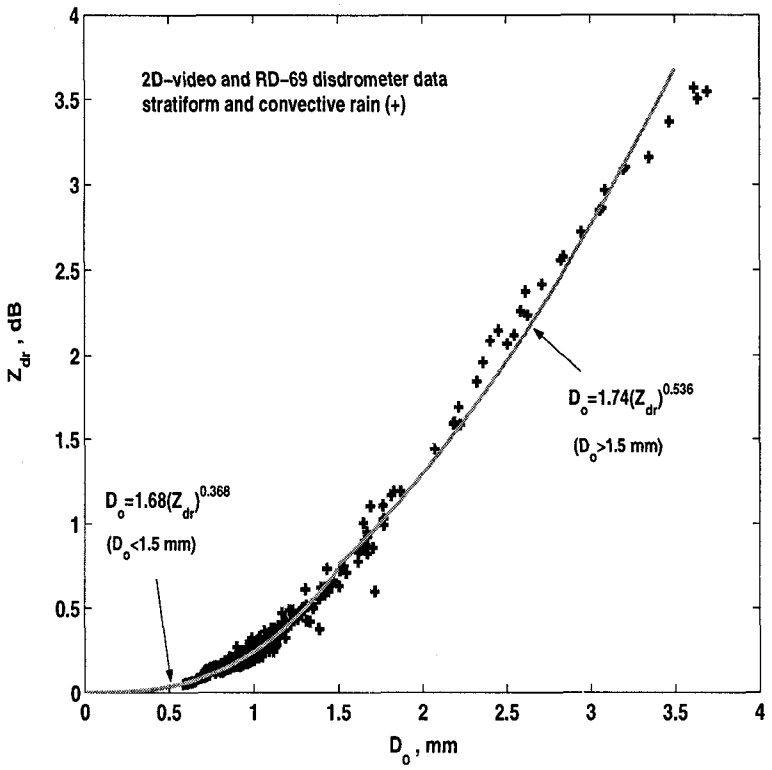

Figure 3.2: Scatterplot of Z_{dr} versus D_o based on the measured dsd data from TRMM/Brazil field campaign. There are 164 2D-video samples for convective rain and 152 samples from both 2D-video and RD-69 for stratiform rain. Two power-law fits for $D_o < 1.5$ and $D_o > 1.5$ mm

After dsd parameters were obtained, we compute Z_h, Z_{dr} and K_{dp} directly at 2.8 GHz assuming that

- mean axis ratio fit suggested by Andsager et al. (1999)[1] for $1 \leq D \leq 4$ mm and by Beard and Chuang (1987)[7] for $D < 1$ and $D > 4$ mm.
- Gaussian canting angle distribution with zero mean and 10^o of standard deviation.
- size integration upto $D_{max} = 2.5D_m$.

Fig 3.2 shows the scatterplot of Z_{dr} versus D_o (D_m and D_o are exchangeable by using (3-6)) and two power-law fits. From the power-law fitting, we can express D_o as a function of Z_{dr} as,

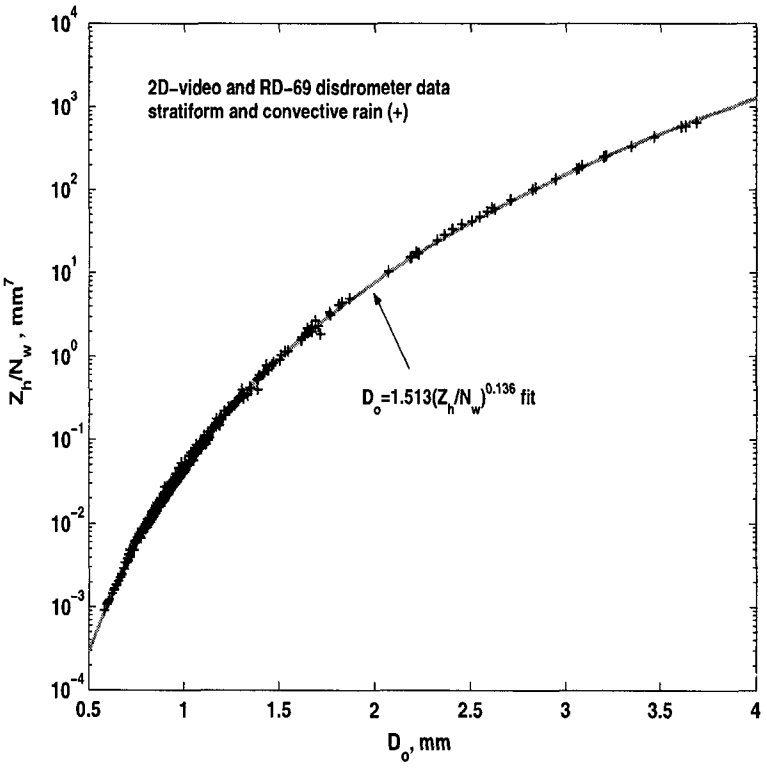

Figure 3.3: As in Fig. 3.3 except Z_h/N_w versus D_o.

$$D_o = 1.68(Z_{dr})^{0.368};\ \ D_o < 1.5mm \tag{3-16a}$$

$$D_o = 1.74(Z_{dr})^{0.536};\ \ D_o > 1.5mm \tag{3-16b}$$

Note that $D_o = 1.5\ mm$ corresponds to $Z_{dr} \approx 0.7\ dB$. In addition, the D_o is proportional to $Z_{dr}^{0.368}$ (or $Z_{dr}^{0.536}$). Therefore, Z_{dr} should be greater than or equal to zero for meaningful D_o. Considering that measurement fluctuations can be around 0.2 dB, the threshold of Z_{dr} for using (3-16a,b) is 0.2 dB. Fig. 3.3 shows the scatterplot of Z_h/N_w versus D_0 and a power-law fit which is

$$D_o = 1.513(Z_h/N_w)^{0.136} \tag{3-17}$$

where Z_h is in $mm^6\ m^{-3}$. Note that we used Z_h/N_w instead of Z_h because the relation between Z_h/N_w and D_o has much less scatter than the relation between Z_h and D_o. The exponent is close to theoretical value $(1/7 = 0.143)$ which is valid for Rayleigh scattering by spherical drops. The exponent in (3-17) is smaller because the drops are oblate. From (3-17), we can express N_w in terms of Z_h and D_o as,

$$N_w = \frac{21 Z_h}{D_o^{7.353}} \tag{3-18}$$

For radar measurements with $Z_h < 35\ dBZ$ and $Z_{dr} < 0.2\ dB$, we can combine (3-16a) and (3-17) to eliminate D_0 and get the relation between Z_h and Z_{dr} as $Z_{dr} = \alpha Z_h^{\delta}$ where $\delta = .136/.368 \approx 0.37$. The coefficient α can be estimated easily as $\hat{\alpha} = < Z_{dr} > / < Z_h^{0.37} >$ where angle brackets denote a spatial average. Fig. 3.4 shows the scatterplot of Z_{dr} versus Z_h combining with a power-law fit to estimate $\hat{\alpha}$. These data are from a stratiform rain on 15 February 1999. After estimating $\hat{\alpha}$, the D_o can be retrieved by using (3-16a) as,

$$D_o = 1.68(\hat{\alpha})^{0.368}(Z_h)^{0.136};\ \ mm \tag{3-19}$$

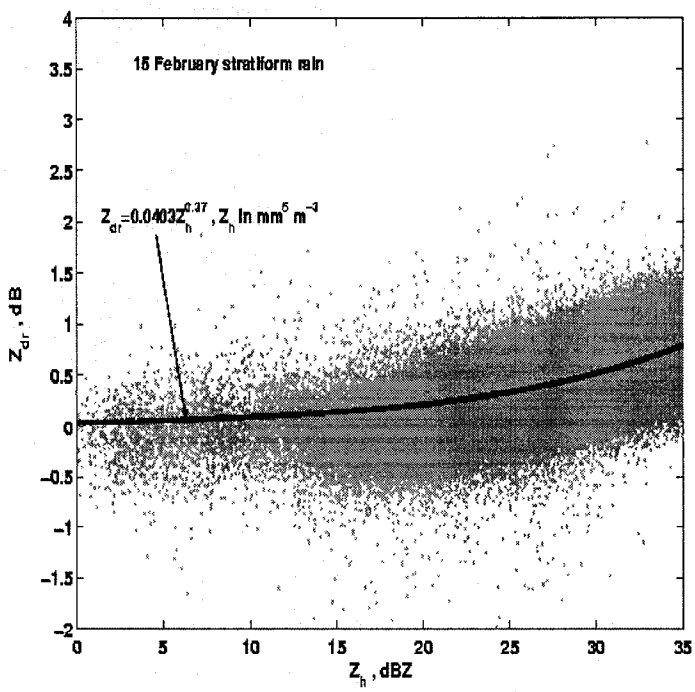

Figure 3.4: S-POL radar measurements of Z_h versus Z_{dr} from stratiform rain on 15 February 1999. The power-law fitting shows the $\hat{\alpha} = 0.0403$.

Subsequently, N_w can be obtained by using (3-18).

To summarize, if radar measurements satisfy thresholds which are $Z_h > 35$ dBZ, $Z_{dr} > 0.2$ dB and $K_{dp} > 0.3$ $^o/km$, the algorithms using β are used to retrieved N_w, D_o and μ. If $Z_h < 35$ dBZ and $Z_{dr} > 0.2$ dB, (3-16a,b) and (3-18) would be used to retrieved D_o and N_w. If $Z_h < 35$ dBZ and $Z_{dr} < 0.2$ dB, (3-19) and (3-18) will be used to obtain N_w and D_o. The dsd shape parameter (μ) is not retrieved in the low rain rate case. We assume that dsd shape is exponential so the μ is assumed to be zero in this case.

3.1.3 Z-R Relationship

In Chapter 2 we have shown that areal rainfall estimate can improve rain rate estimation significantly. However, there is a tradeoff. We reduce the noise by estimating rain rate over the area, but, at the same time, we also lose spatial resolution. On the other hand, the traditional rain rate estimator, such as $R(Z_h, Z_{dr})$, can estimate rain rate at each individual resolution volume but would be biased by noise, measurement fluctuations and variation of mean axis ratio versus D (due to oscillation or turbulence). The Z-R estimator is the most widely used rain rate algorithm and can be expressed as,

$$Z = aR^b \tag{3-20}$$

where Z is reflectivity factor in $mm^6\ m^{-3}$. The Z-R relation is easy to use because it only involves power measurements; it is less affected by noise because the reflectivity signal is strong relative to Z_{dr} or K_{dp}. However, the coefficient, a, varies considerably mainly depending on N_w. By knowing the dsd parameters, we can continuously adjust the coefficient of the Z-R robustly. So it may be possible to improve both accuracy and resolution.

The rain rate (R) in terms of the dsd model and in units of $mm\ h^{-1}$ can be written as,

$$R = (0.6 \times 10^{-3}\pi) \int v(D) D^3 N(D) dD \tag{3-21}$$

where $v(D)$ is the drop terminal velocity and expressed as (Atlas and Ulbrich 1977)[5],

$$v(D) = 3.78 D^{0.67}; \quad ms^{-1} \tag{3-22}$$

Combining the gamma dsd form shown in (3-7), the rain rate (R) becomes,

$$\begin{aligned} R &= (0.6 \times 10^{-3}\pi) \int_0^\infty 3.78 D^{0.67} D^3 N_w f(\mu) (\frac{D}{D_o})^\mu exp - (3.67 + \mu) \frac{D}{D_0} dD \\ &= (0.6 \times 10^{-3}\pi)(3.78) N_w f(\mu) \Gamma(4.67 + \mu) \frac{D_o^{4.67}}{(3.67 + \mu)^{4.67+\mu}} \end{aligned} \tag{3-23}$$

Therefore, the R/N_w can be expressed in terms of μ and D_o as,

$$\frac{R}{N_w} = F_R(\mu) D_o^{4.67} \tag{3-24}$$

where $F_R(\mu)$ is,

$$F_R(\mu) = (0.6 \times 10^{-3}\pi)(3.78) f(\mu) \frac{\Gamma(4.67 + \mu)}{(3.67 + \mu)^{4.67+\mu}} \tag{3-25}$$

Similarly, the reflectivity factor (Z) is the 6th moment of dsd and can be expressed as,

$$\begin{aligned} Z &= \int_0^\infty D^6 N_w f(\mu) (\frac{D}{D_o})^\mu exp - (3.67 + \mu) \frac{D}{D_0} dD \\ &= N_w f(\mu) \Gamma(7 + \mu) \frac{D_o^7}{(3.67 + \mu)^{7+\mu}}; mm^6 m^{-3} \end{aligned} \tag{3-26}$$

The Z/N_w also can be expressed in terms of μ and D_o as,

$$\frac{Z}{N_w} = F_Z(\mu) D_o^7 \tag{3-27}$$

where $F_Z(\mu)$ is,

$$F_Z(\mu) = \frac{f(\mu)\Gamma(7+\mu)}{(3.67+\mu)^{7+\mu}} \tag{3-28}$$

Using (3-24) and (3-27) to eliminate D_o then,

$$\begin{aligned} \frac{Z}{N_w} &= \frac{F_Z(\mu)}{F_R(\mu)^{\frac{7}{4.67}}} \left[\frac{R}{N_w}\right]^{\frac{7}{4.67}} \\ &= \alpha \left[\frac{R}{N_w}\right]^b \end{aligned} \tag{3-29}$$

where $b = 7/4.67 \approx 1.5$. Finally, the Z-R relationship in terms of N_w is,

$$Z = \alpha (N_w)^{1-b} R^b \tag{3-30}$$

The coefficient of Z-R is $a = \alpha (N_w)^{1-b}$ and the exponent is $b \approx 1.5$.

3.2 Case Study

In this section, we analyze two cases, one is a storm from TRMM/Brazil on 15 February 1999 and is the same case we studied in Section 2.3.2. The second is a storm from TRMM/TEFLUN-B (Florida) on 17 September 1998. In each case, we have analyzed two situations, a large area which includes all gages in the gage network and usually includes more than 600 resolution volumes, and a small area which is 1x1 km^2 with the NOAA profiler located in the center of the area. Usually, there are 16-20 resolution volumes in the small area. The dsd parameter set, (N_w, D_o, μ), is averaged over the area under study.

Fig. 3.5 shows the scheme we use to calculate the dsd parameters for an individual resolution volume. Fig. 3.6 shows the averaging scheme of dsd parameters.

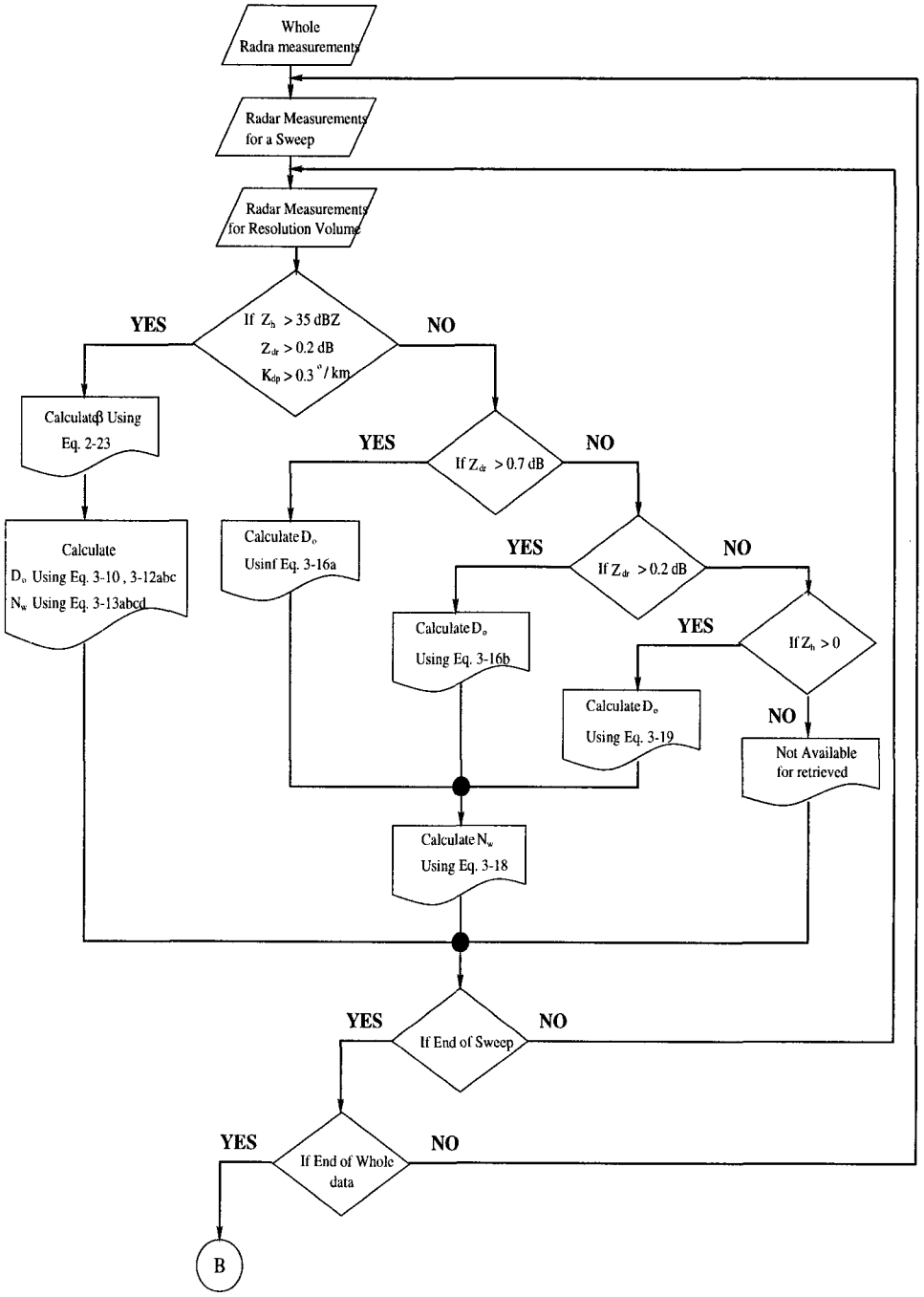

Figure 3.5: The flowchart of dsd parameters retrieval for individual resolution volumes. Note that the threshold for β is for a small area.

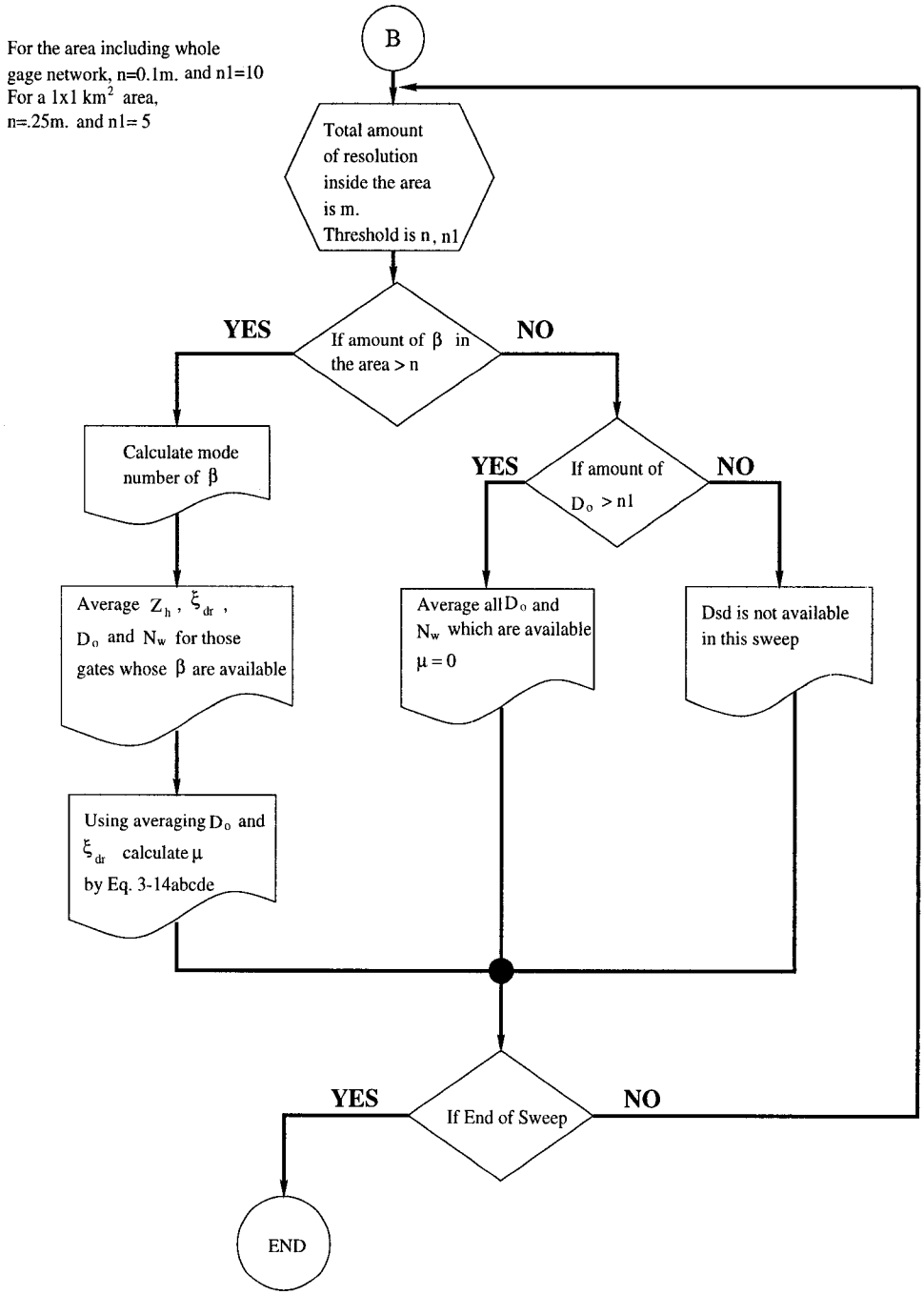

Figure 3.6: The flowchart of dsd parameters averaged over an area.

Since those radar measurements which satisfy the β threshold are stronger signals, they should better represent the drop size distribution. Therefore, if a sweep includes sufficient resolution volumes which satisfy the β threshold, we retrieved N_w and D_o using the β method ((3-10), (3-12abc) and (3-13abcd)). We pre-set the sufficient number of resolution volumes as being 10% of the total resolution volumes for the large area and 25% for the small area. In addition, the modal β is used to represent the areal β for the large area, whereas average β is used for the small area. For those radar sweeps where the available β values are not sufficient in number, we average all available D_o and N_w values directly to get the areal N_w and areal D_o with μ set to zero.

3.2.1 S-band Data from Brazil

The first case we analyzed is a storm event from TRMM/Brazil on 15 February 1999. A brief description of field experiment was given in Section 2.3.2. Fig. 2.12 shows the location of the gage network. The large area which includes all gages in the network is a polar area around 4.6x5.7 km^2 located north-east of the S-POL radar. The range is from 39.97 km to 44.57 km and the azimuth angle is from 18.71^o to 26.42^o. Generally, each sweep over the area includes 19 rays and 31 gates in each ray. So there are around 600 resolution volumes in a sweep. The NOAA profiler (the circle mark) is located at the north-west corner of the gage network and near the gage #26 (the cross mark). The small area is a polar area around 1x1 km^2 and has the NOAA profiler in the center. Normally, there are 2 rays in the small area and 6 gates in each ray.

Fig. 3.7 shows three dsd parameters (N_w, D_o and μ) and averaged gage rain rate (R_g) versus time for the large area. There are three strong rain cells ($R > 10$ $mm\ h^{-1}$). The first cell is from 4:31 to 4:56 (4.52 to 4.92 in fractions of hour) and peak rain rate is 41.1 $mm\ h^{-1}$ at 4:49. During this period, $log_{10}N_w$ increases from

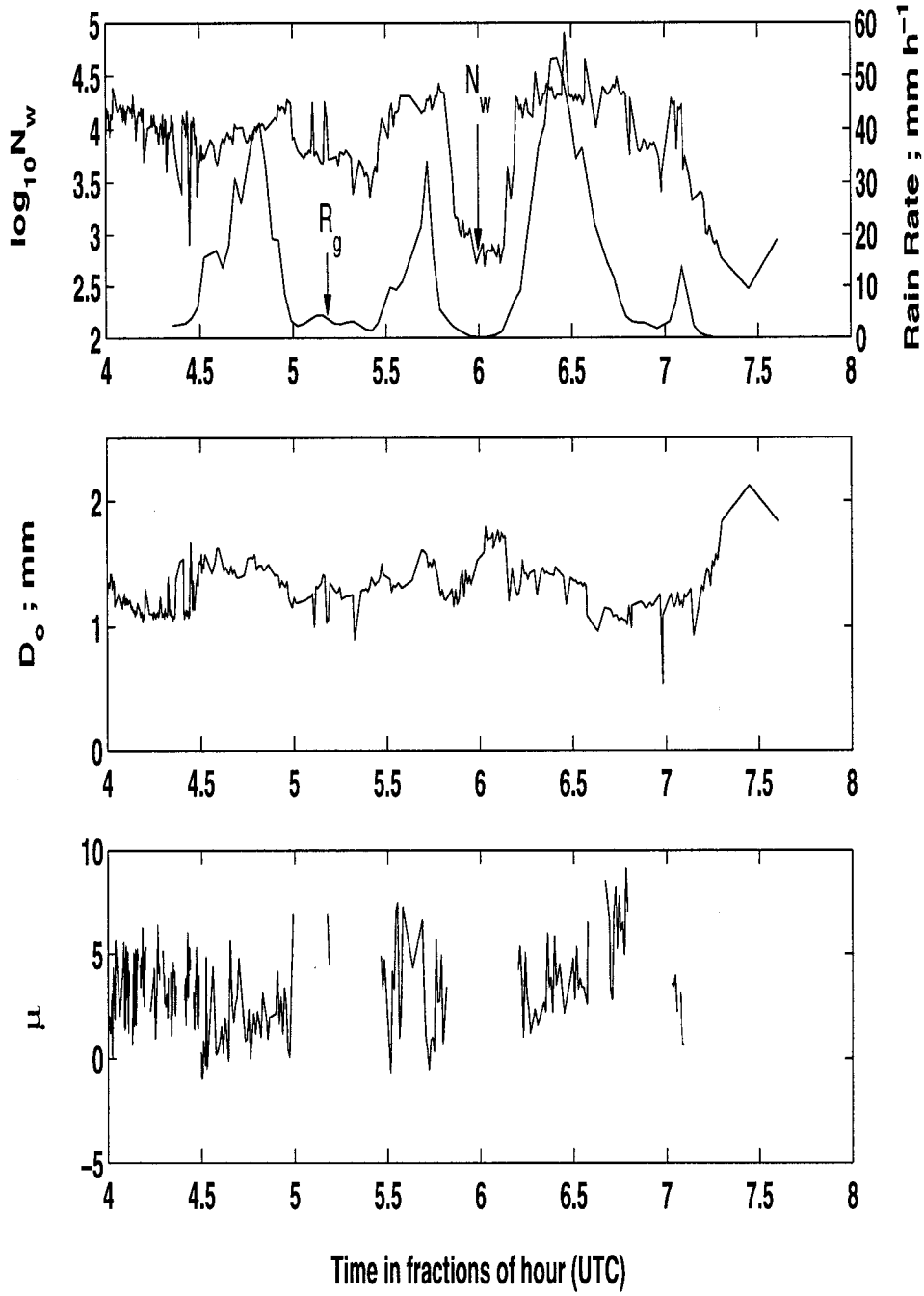

Figure 3.7: The gage rain rate and radar-retrieved dsd parameters (N_w,D_o,μ) for the large area on 15 February 1999 in Brazil. Note that gage rain rate (R_g) is averaged over all gages in the network within a 2-minute time interval. The N_w is in log scale.

3.7 to 4.1, D_o varies between 1.4 to 1.6 mm with mean of 1.5 mm, and μ varies between 0 to 5 with mean of 1.8. Between the first and second cells, $log_{10}N_w$ drops from 4.2 to 3.4 and D_o varies between 1.2 and 1.5 mm with mean of 1.3 mm. In the low rain rate regions, the corresponding Z_h is low (less than β threshold which is 35 dBZ). Therefor, μ is not available in these regions and assumed to be zero. The second intensive cell is from 5:35 to 5:45 (5.59 to 5.76). During this period, $log_{10}N_w$ is around 4.2, D_o is around 1.5 mm and μ varies between -0.5 and 7 with mean of 2.0. Between the second and third cells, $log_{10}N_w$ is around 2.9 and D_o varies between 1.2 and 1.8 mm with mean of 1.4 mm. The third cell is from 6:15 to 6:43 (6.26 to 6.72). In this period, $log_{10}N_w$ varies between 4 to 4.9 with mean of 4.3, D_o is between 1 and 1.5 mm and is around 1.4 mm around the peak, and μ is between 1 and 7 with mean of 3.7.

Fig. 3.8 shows the gage rain rates compared with the Z-R relation for the large area. The coefficient of the Z-R relation is based on N_w and μ (see (3-30)). The N_w is averaged over the large area. After obtaining the coefficient of the Z-R relation, we calculate rain rate for each radar resolution volume, and then compute the average rain rate for the whole area. Fig. 3.8 shows that the radar rain rates agree with gage rain rates very well except an underestimate near the peak. Fig. 3.9 compares the cumulative rainfall; the cumulative error (CE) is 15.37% underestimate.

Fig. 3.10 and Fig. 3.11 show the comparison of radar retrieved dsd parameters and profiler retrieved dsd parameters for the small area. The profiler dsd parameters are estimated by two different methods (Williams, personal communications), the statistic method (refer as "stat", the plus marks) and single Doppler spectrum (refer as "sds", the diamond marks). In addition, profiler dsd parameters are averaged over the three lowest heights (411 m, 621 m and 831 m) and over a 3-minute interval. We find that the radar and the profiler (especial the sds method) agree

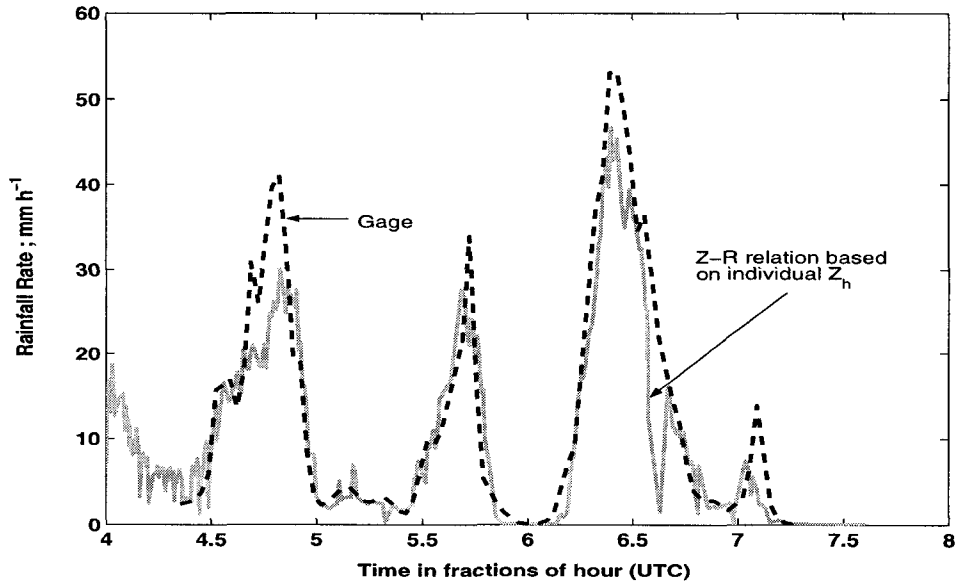

Figure 3.8: The gage rain rate (R_g) and $R(Z_h)$ versus time for large area on 15 February 1999 in Brazil. The coefficient of $R(Z_h)$ is based on averaging N_w, and then the rain rate is calculated for each resolution volume.

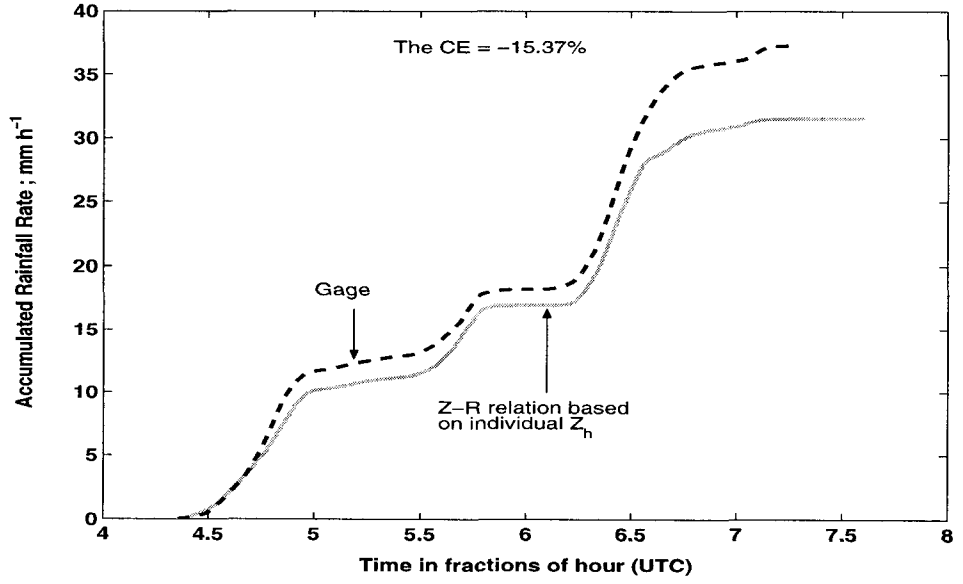

Figure 3.9: As in Fig. 3.8 except for cumulative rainfall. The NB is 15.37% (underestimate).

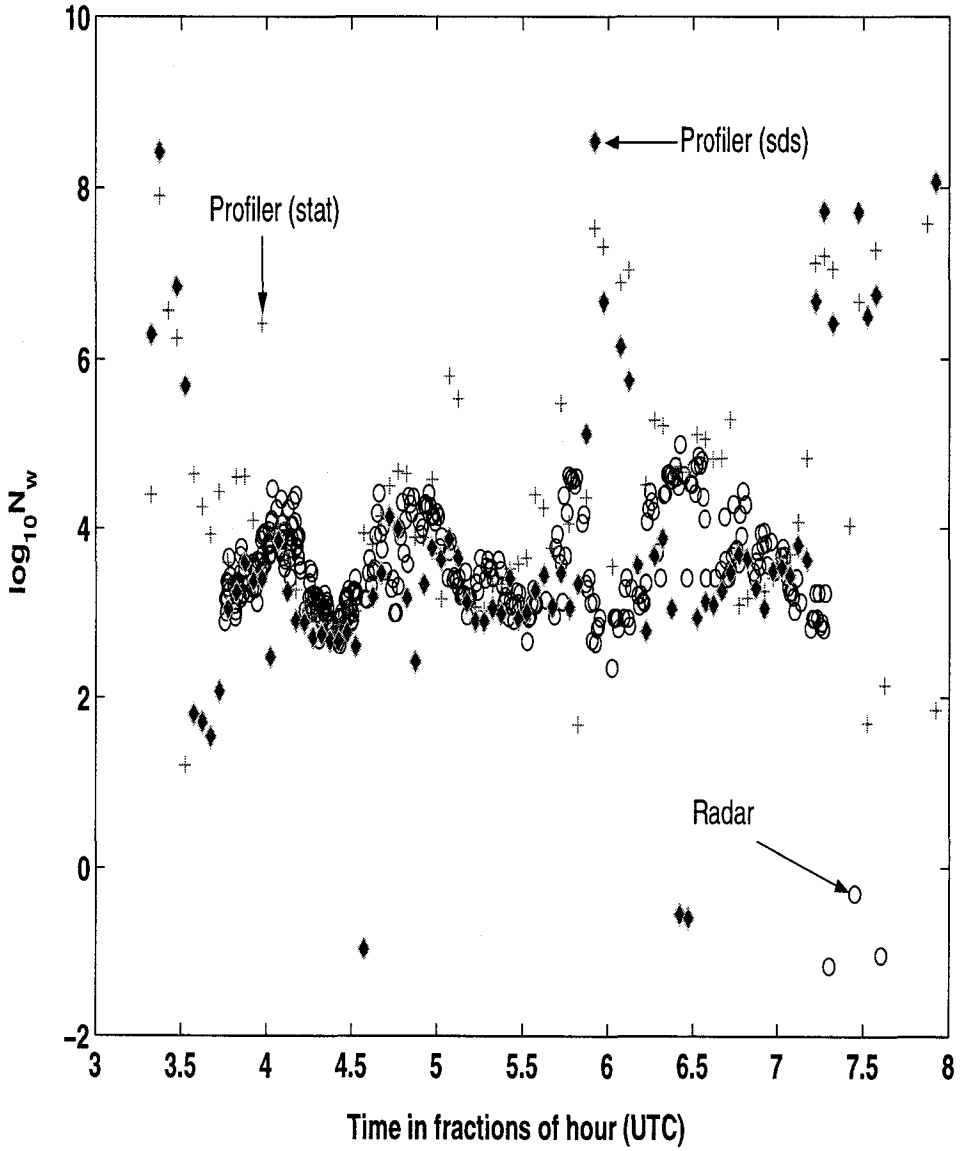

Figure 3.10: The radar retrieved N_w and profiler retrieved N_w for the small area on 15 February 1999. The profiler N_w is averaged over the three lowest heights (411 m, 621 m and 831 m) and over a 3-minute interval.

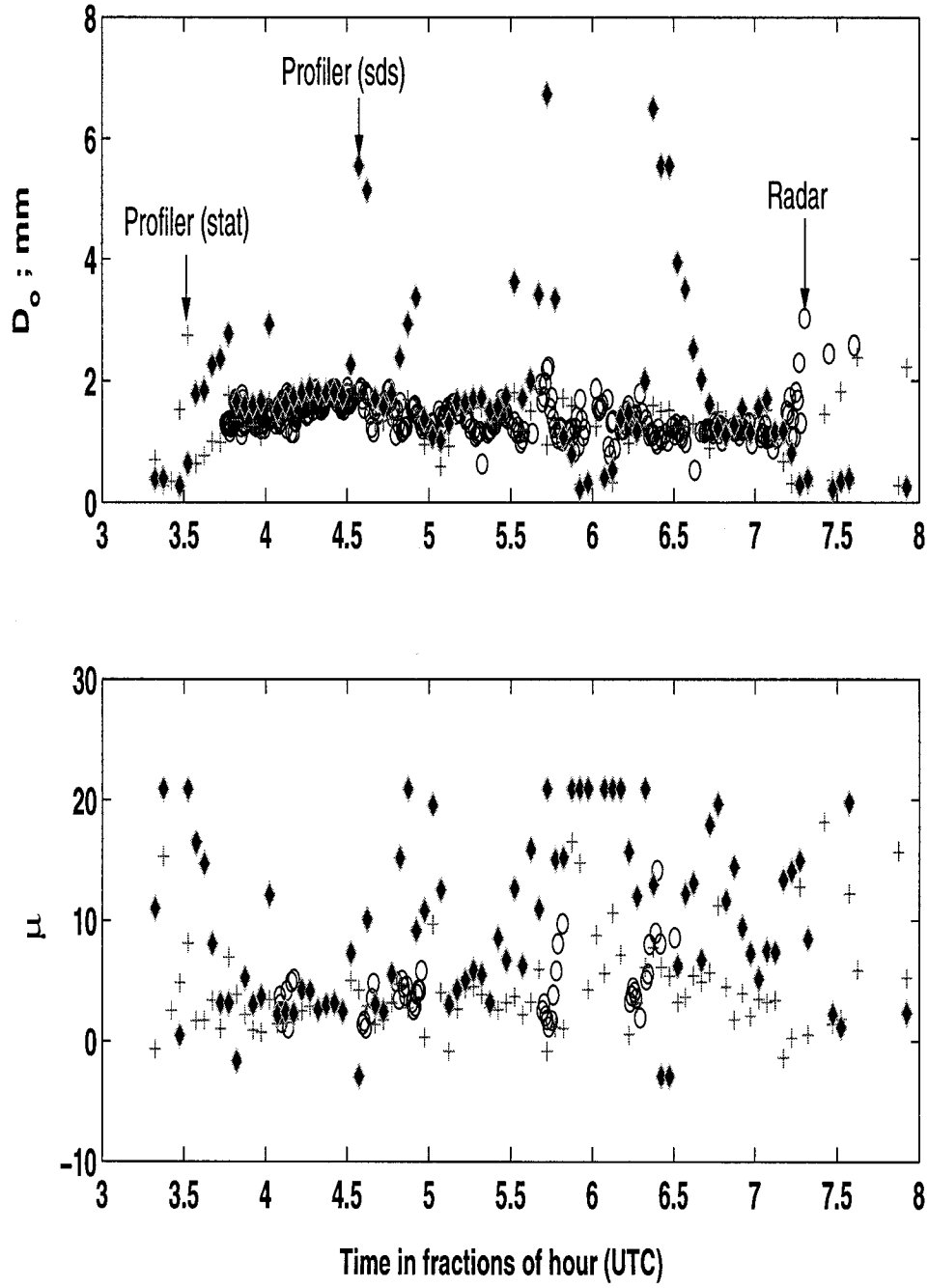

Figure 3.11: As in Fig. 3.10 except for D_o and μ.

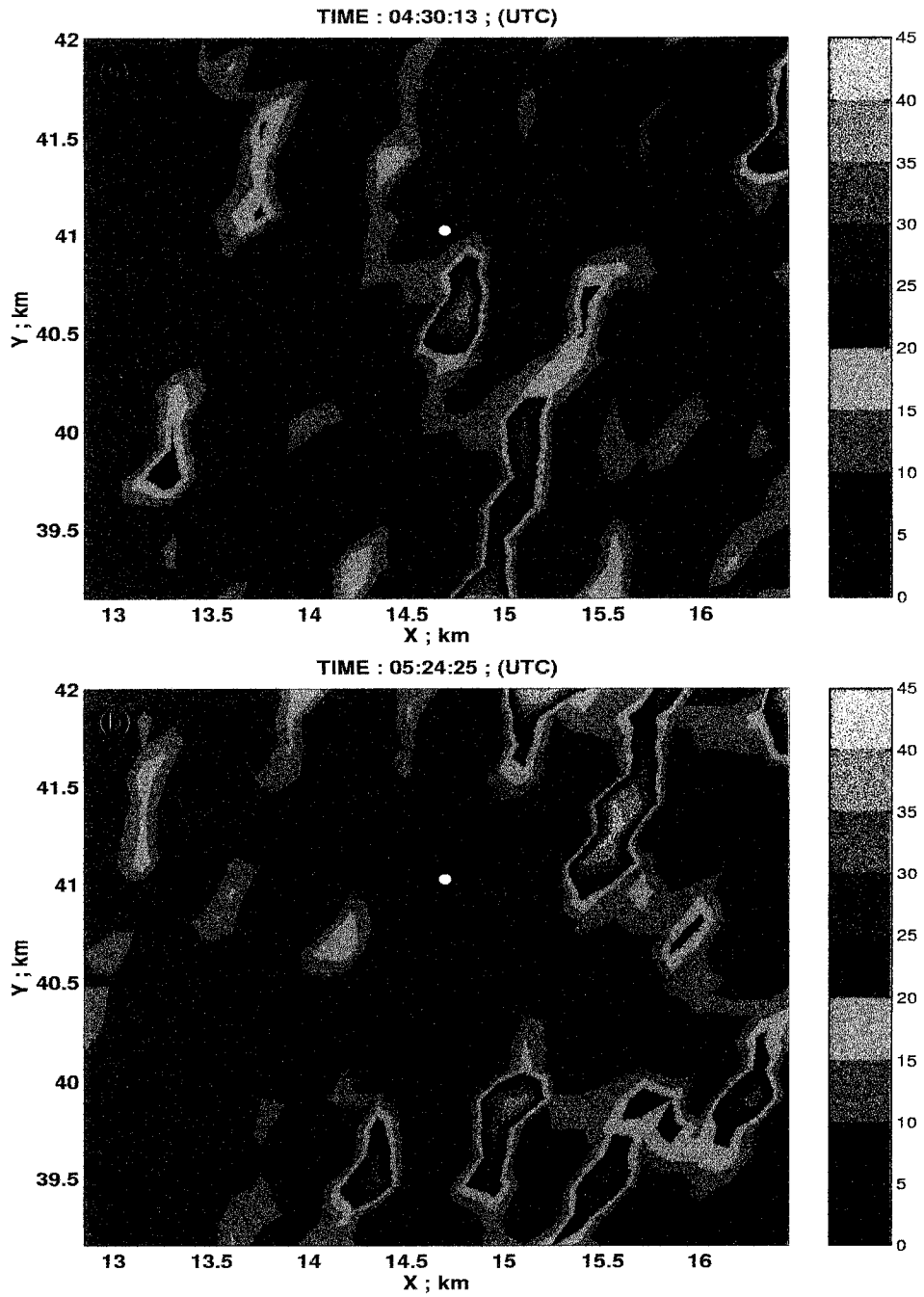

Figure 3.12: **(a)** The amplitude of Z_h gradient at 4:30 (UTC) on 15 February 1999. The white dot is the location of profiler. **(b)** As in (a) except that time is 5:24 (UTC).

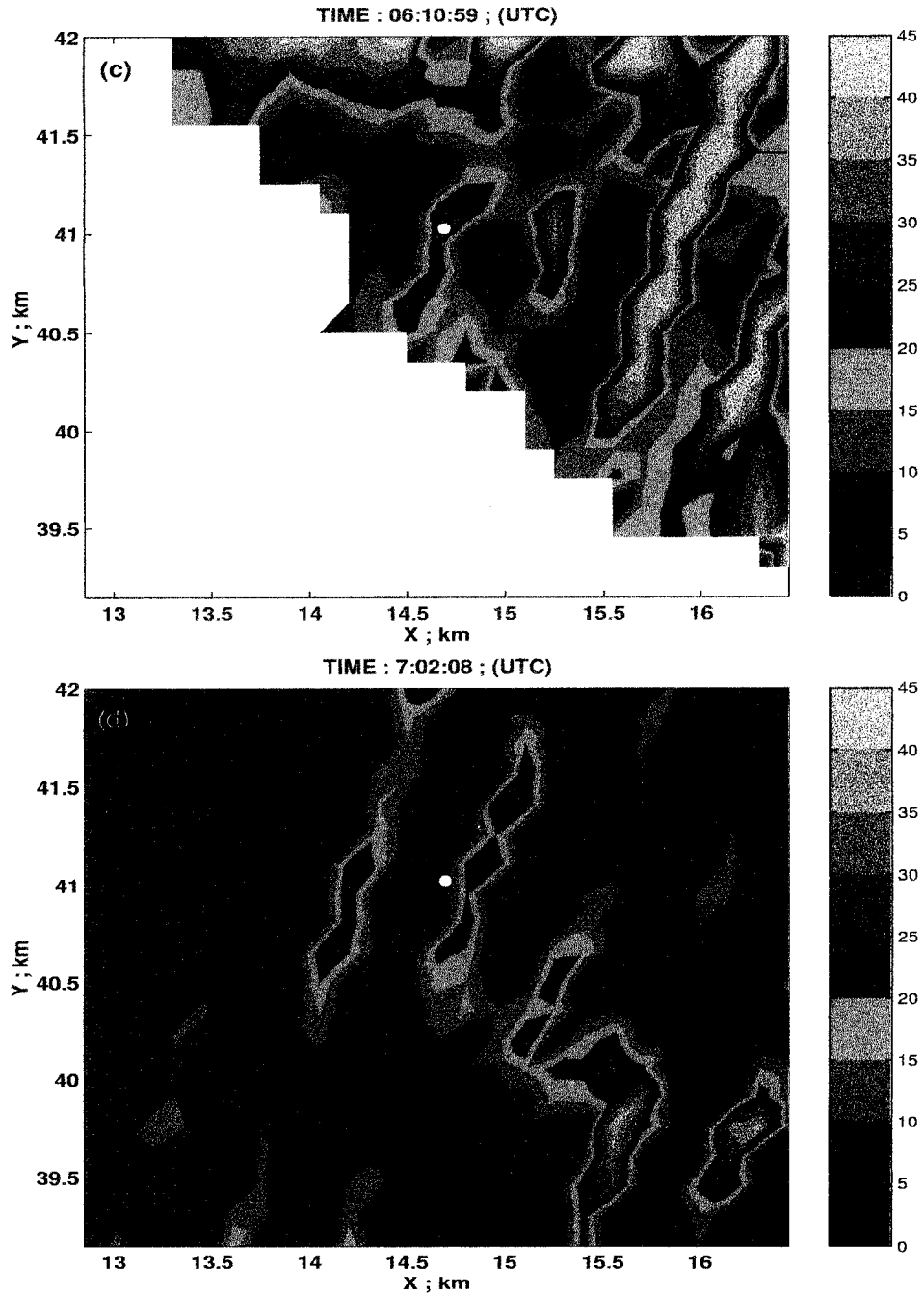

Figure 3.12: **(c) (d)** As in (a) except that time is 6:10 and 7:02 (UTC).

with each other most of the time except from 5.8 (5:48) to 6.2 (6:12) and after 7.0 (7:00). Fig. 3.12a and b show the amplitude of the Z_h gradient when radar and profiler generally agree with each other (at 4:30 and 5:24 UTC). We found that there are no high gradient areas near the profiler (white dot mark) . On the other hand, Fig. 3.12c and d show the amplitude of Z_h gradient when radar disagrees with profiler. At 6:10 UTC, profiler is located within a high gradient region (25-30 dBZ/km). At 7:02, the profiler is located near the edge of low gradient region and very close to a high gradient region. Since radar area and the profiler area may be mismatched, the high Z_h gradient may lead to the deviation between radar and profiler. In addition, high Z_h gradient will increase radar measurement error due to the antenna pattern (e.g. the mainlobe points to a low Z_h area but the sidelobe points to high Z_h area). Therefore, we suspect that the high Z_h gradient may be the reason for the disagreement between radar and profiler retrieved dsd parameters.

Fig. 3.13 compares gage rain rate with $R(Z_h)$ whose coefficient is based on averaging N_w and μ over the 1x1 km^2 area. The result shows the $R(Z_h)$ generally agrees with gage rain rates except that the peaks are underestimated (especially on three main peaks). Since the antenna beamwidth of S-POL is 0.91^o and gage #26 is 43.5 km away from radar, the radar sensing area is around 690x150 m^2 and is much larger than the area that the gage can represent. So radar would tend to average down the peak rain rate especially near the small rain cells. Fig. 3.14 shows the comparison of rain accumulations; the cumulative error is 43.3% underestimate. The large underestimation, as expected, is mainly due to underestimation of the three peaks.

3.2.2 S-band Data from Florida

During 1 August to 30 September 1998, a field experiment known as TRMM/TEFLUN-B was held in Florida. Surface-based facilities for TEFLUN-B include the Mel-

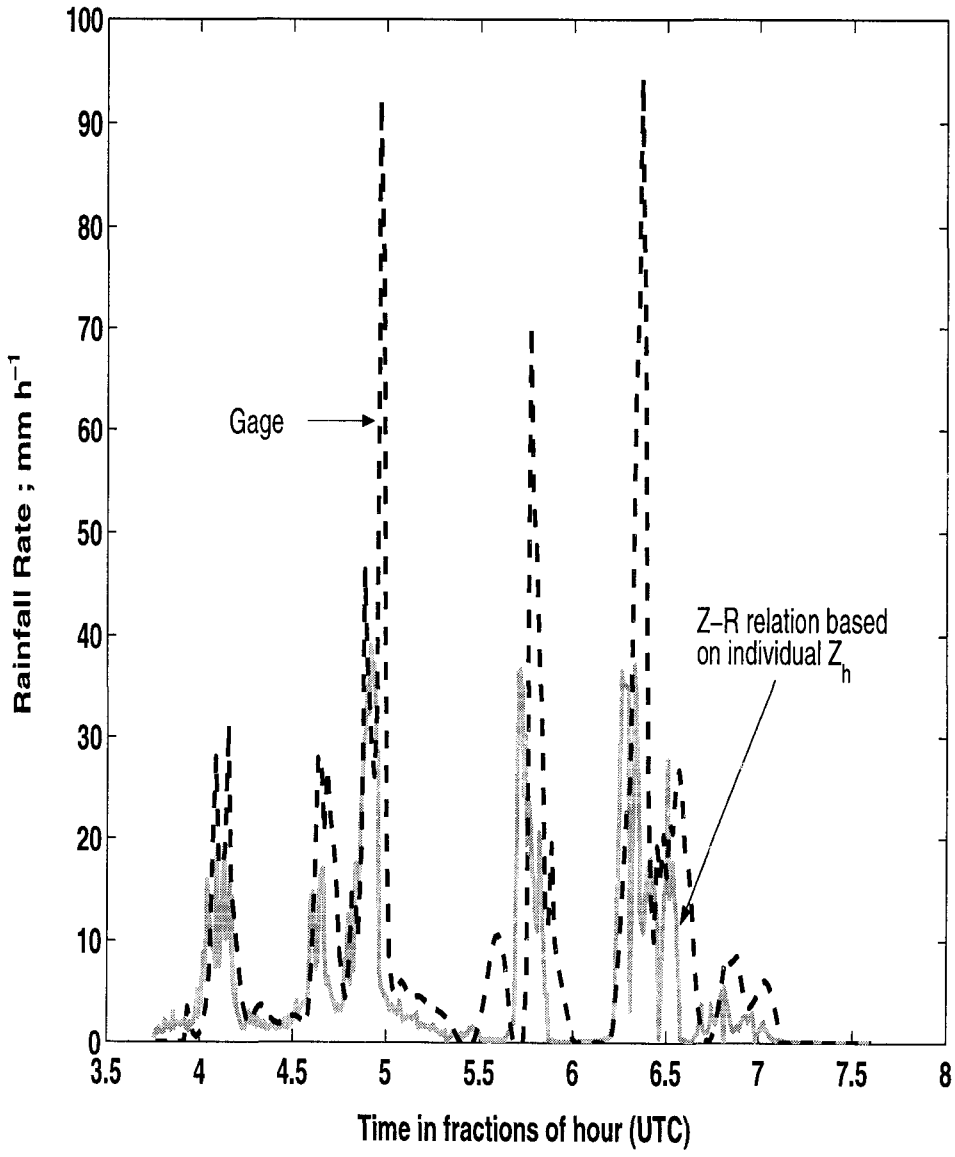

Figure 3.13: Gage rain rates compare with $R(Z_h)$ on 15 February 1999. Note that the coefficient of $R(Z_h)$ is based on averaging N_w and μ over a 1x1 km^2 area.

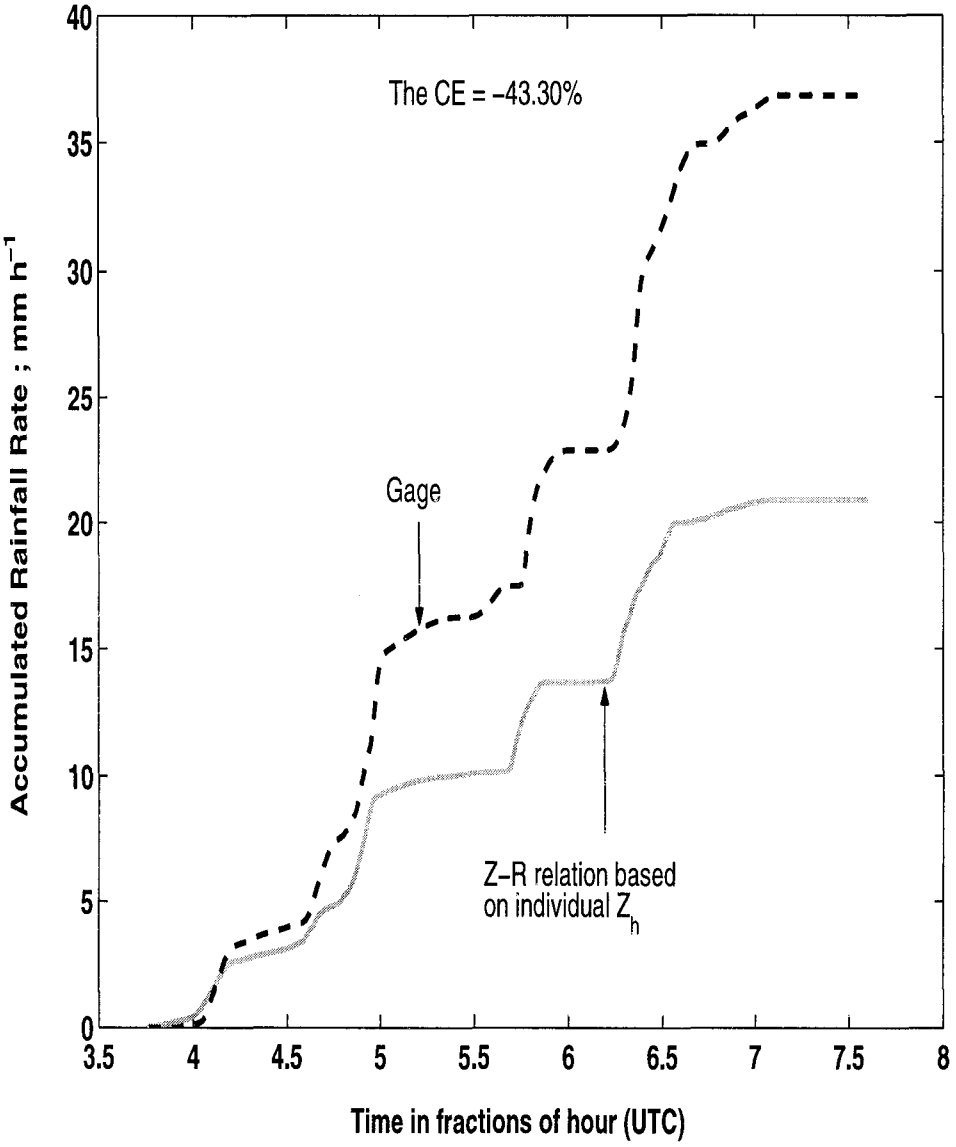

Figure 3.14: As in Fig. 3.13 except for cumulative rainfall.

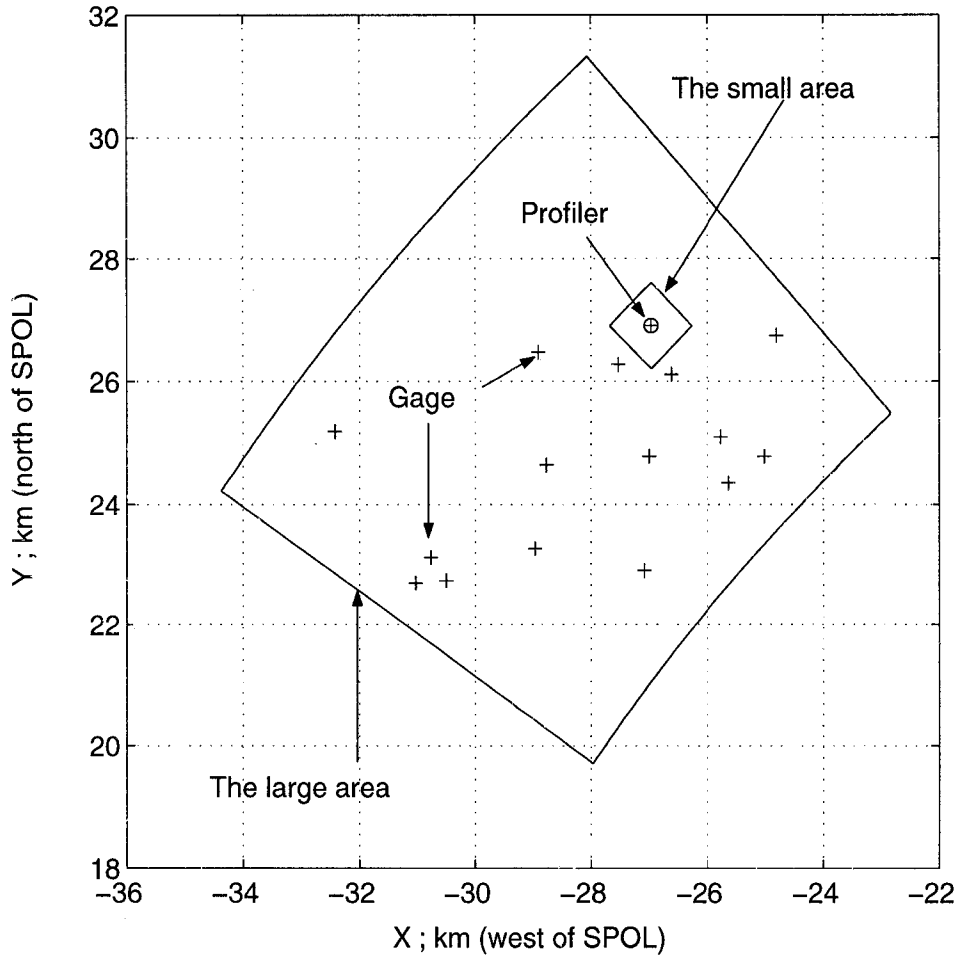

Figure 3.15: The location of gages in DRGN. The circle marks the NOAA Profiler which is located near gage #101. The S-POL radar was located at origin of coordinates.

bourne NEXRAD, the NCAR S-POL and NOAA AL Profiler system. The S-POL radar was located at 27^o $53'$ 21.6" North and 80^o $44'$ 44.16" West. There were two groups of gages operating during the field campaign. The rain gages were tipping bucket type, and offer rain rate and accumulative rain every minute. One group was located at the Kennedy Space Center (KSC gage network). The other group was located north-west of S-POL near Hollopaw, Florida (refer as "DRGN"-dense rain gage network; or "TFB"). The case we analyze in this section involved gage data from DRGN. Fig. 3.15 shows the location of gages (cross marks) in DRGN, location of NOAA profiler (circle mark) and the area under study (both large and small polar areas). The gage # 101 is located very near the profiler. The azimuth angle of the large area is from 305.17^o to 318.14^o and usually includes 19 rays. The range of the large area is from 34.22 km to 42.06 km and includes 52 gates in each ray. So the large area is around 7.8x8.6 km^2 and includes around 988 resolution volumes. The small area is a 1x1 km^2 polar area, and includes 2 rays and 6 gates for each ray. So the small area usually involved only 12 resolution volumes.

On 17 September 1998, a storm was moving into the south-west of S-POL at 17:00 (UTC). This system moved to the north-east along the azimuth angle sector of 210^o-30^o. The radar image can be found at the UCAR website[1]. Fig. 3.16 shows the averaged gage rain rate and three dsd parameters (N_w, D_o and μ) averaged over the larger area. There are two strong rain cells ($R > 10$ mm h^{-1}), the first occurring at 19:08 (19.15) to 19:34 (19.58). The peak gage rain rate is 47.72 mm h^{-1} at 19:16 (19.28). During this period, N_w is around 4.7 in log scale, D_o is around 1.6 mm from 19:08 to 19:24 and then gradually reduces to 1.4 mm, and μ varies between 0 to 4 with mean of 2.05. In between the two cells, N_w reduces to around 3.7 in log scale, D_o varies between 1.1 and 1.3 mm with mean of 1.2 mm

[1]http://www.atd.ucar.edu/rsf/PRECIP98/quicklook/spol_p98.htm

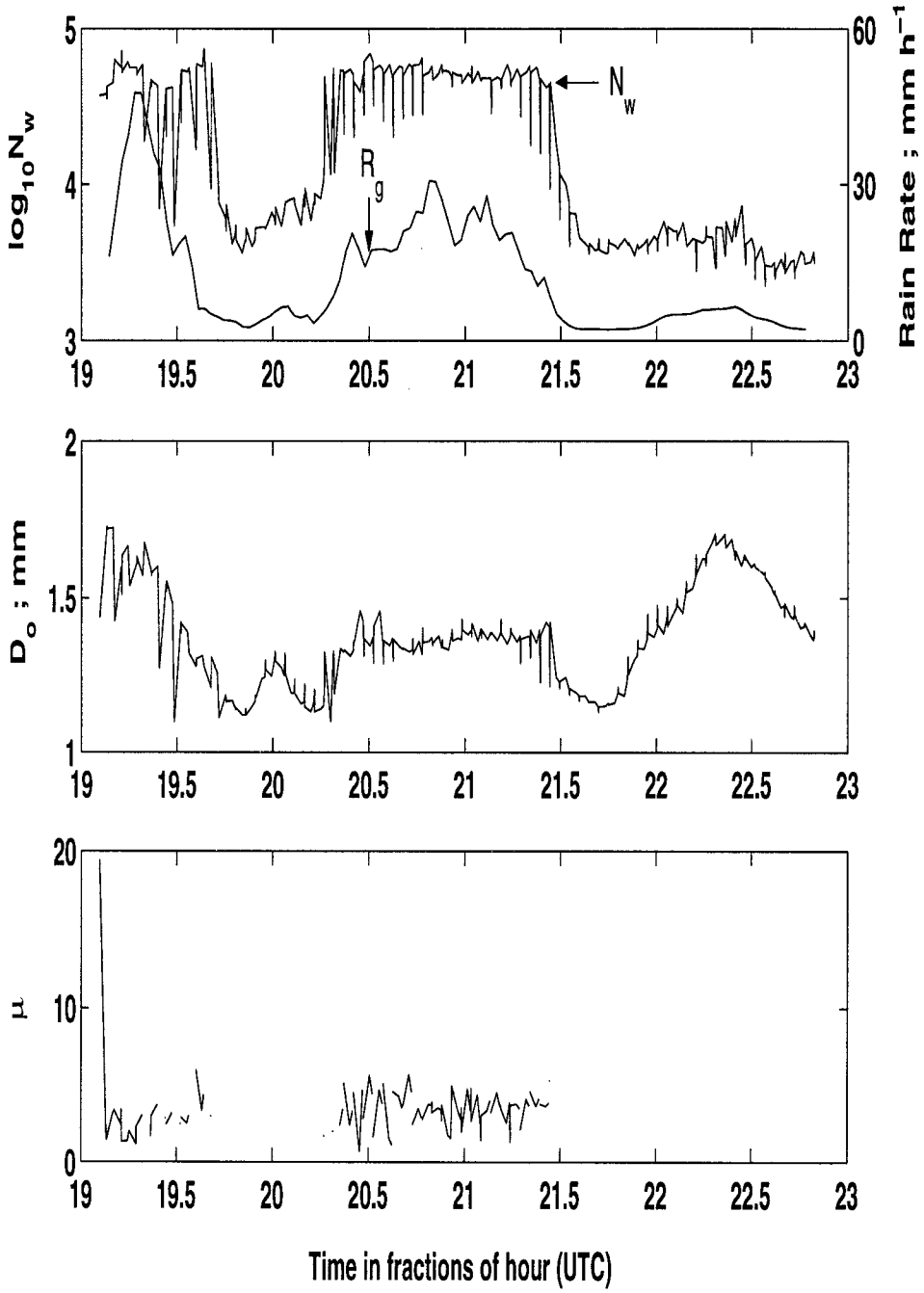

Figure 3.16: The gage rain rate and radar retrieved dsd parameters (N_w,D_o,μ) for the large area on 17 September 1998 in Florida. Note that gage rain rate (R_g) is averaged over all gages in the network within a 2-minute time interval. The N_w is in log scale.

and μ is zero as default value because Z_h is less than threshold. The second rain cell occurs from 20:20 (20.35) to 21:24 (21.41). The peak rain rate is 30.58 $mm\ h^{-1}$ at 20:48 (2.81). During this period, N_w is around 4.7 in log scale, D_o varies between 1.3 to 1.45 mm with mean of 1.36 mm, and μ varies between 0 to 6 with mean of 2.9. After 21:24, N_w reduces to around 3.6 in log scale. At the same time, D_o reduces form 1.4 to 1.15 mm, and then increases to 1.7 mm at 22:18 (22.31). After 22:18, D_o gradually reduces to 1.35 mm. As expected, μ is zero as default value because of low Z_h.

Fig. 3.17 shows the comparison of average gage rain rate (averaging over all gages and over a 2-minute interval) with $R(Z_h)$ for the large area. As in the Brazil case, the coefficient of $R(Z_h)$ is based on averaging N_w and μ over the large area. The $R(Z_h)$ generally agrees with gage rain rate except near the peaks. Fig. 3.9 shows the cumulative rain comparison; the cumulative error is 27% overestimate.

Fig. 3.19 and Fig. 3.20 show the radar-retrieved dsd parameters compared with the profiler-retrieved dsd parameters for the small area. The results show that the radar retrievals of the dsd generally agree with profiler dsd (either sds or stat method). There are two time intervals where the radar significantly disagrees with the profiler (both sds and stat method). The first portion is from 21:00 to 21:45 and the second one is after 22:00. As we did for TRMM/Brazil case, we examine the amplitude of the Z_h gradient at these times. Fig. 3.21a,b show the amplitude of Z_h gradient at 19:31 and 20:30 when radar dsd agrees with the profiler. In both figures, the profiler is located near relative low gradient areas. Fig. 3.21c,d show the amplitude of Z_h gradient at 21:29 and 22:15 when radar retrieval disagrees with the profiler. At 21:29, the profiler is located at the edge of a high gradient region. At 22:15, the profiler is located near a high gradient region. These results are similar to the TRMM/Brazil case. They support our hypothesis that Z_h gradient can lead to mismatch between radar and profiler retrievals.

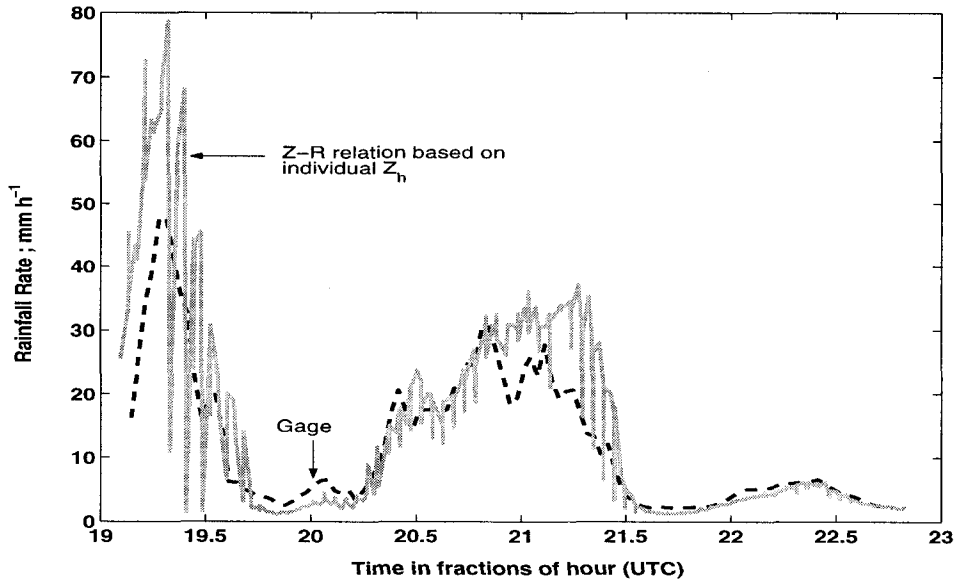

Figure 3.17: The gage rain rate (R_g) and $R(Z_h)$ versus time for large area on 17 September 1998. The coefficient of $R(Z_h)$ is based on averaging N_w, and then rain rate is calculated for each resolution volume.

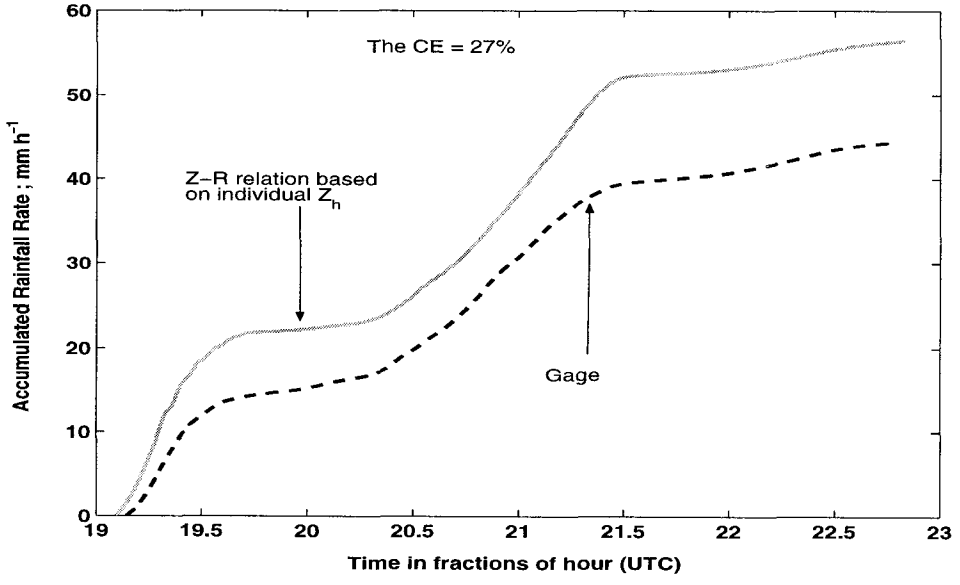

Figure 3.18: As in Fig. 3.17 except for cumulative rainfall. The NB is 27% (overestimate).

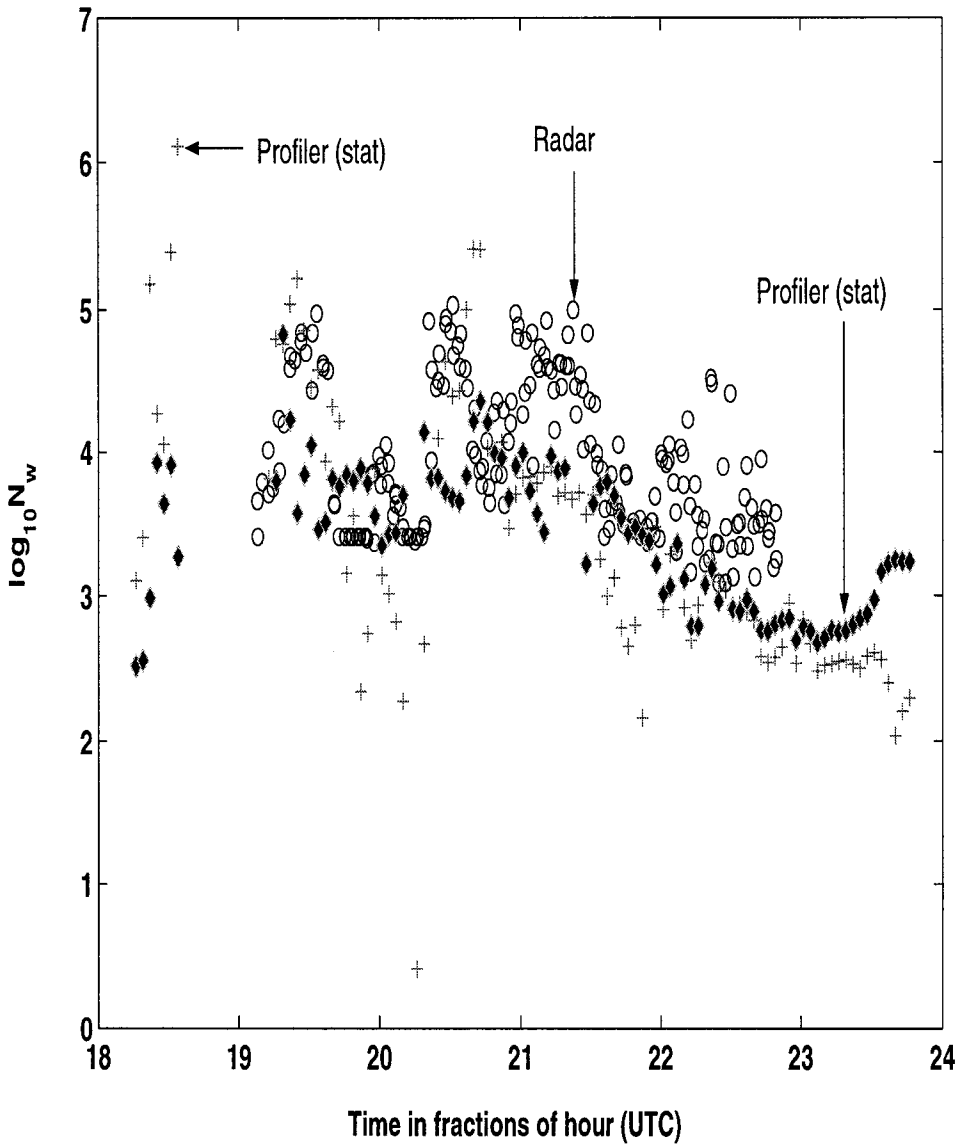

Figure 3.19: The radar retrieved N_w and profiler N_w for the small area on 17 September 1998 at Florida. The profiler N_w is averaged over three lowest height (308 m, 413 m and 518 m) and 3-minute interval.

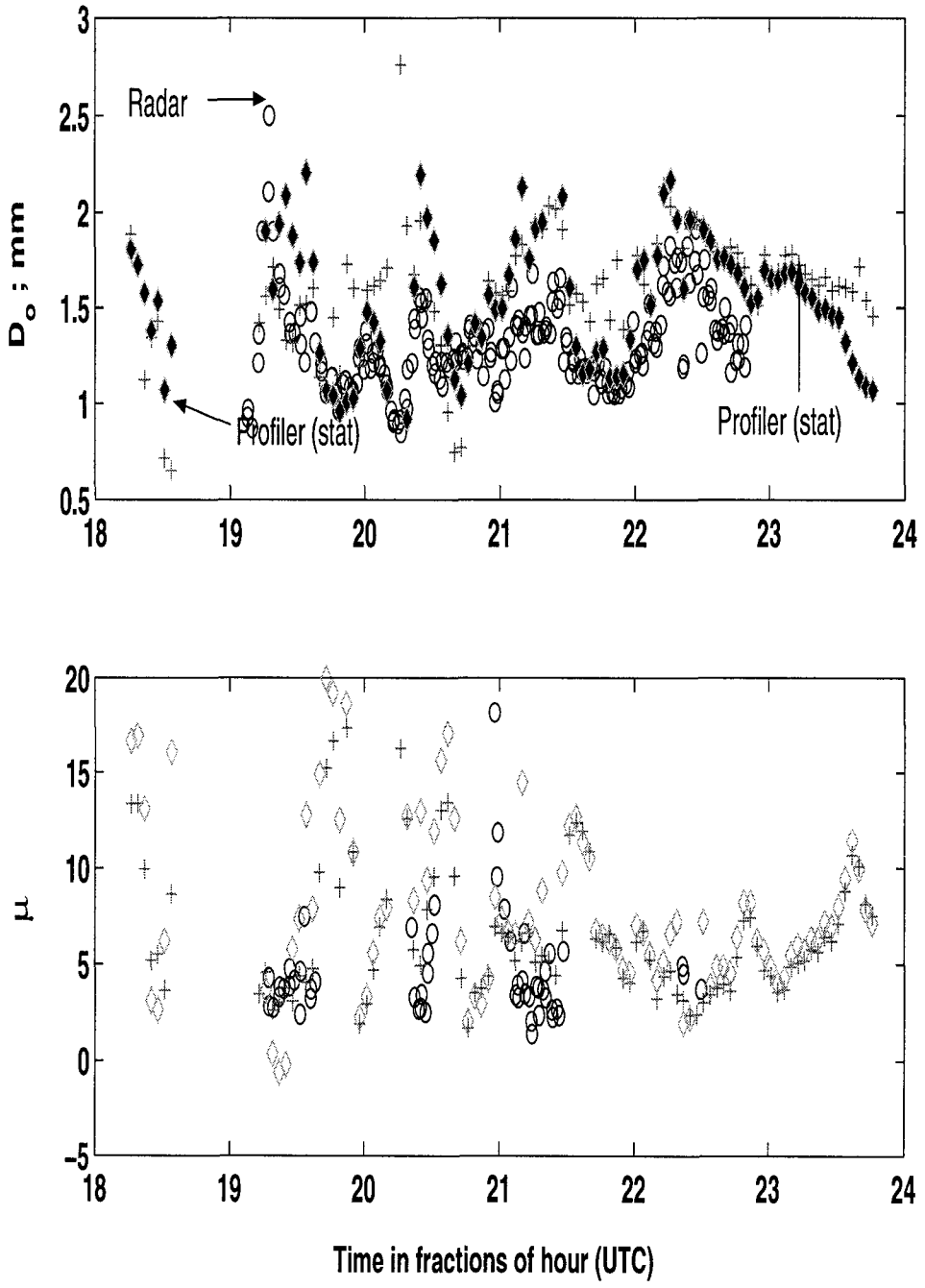

Figure 3.20: As in Fig. 3.19 except for D_o and μ.

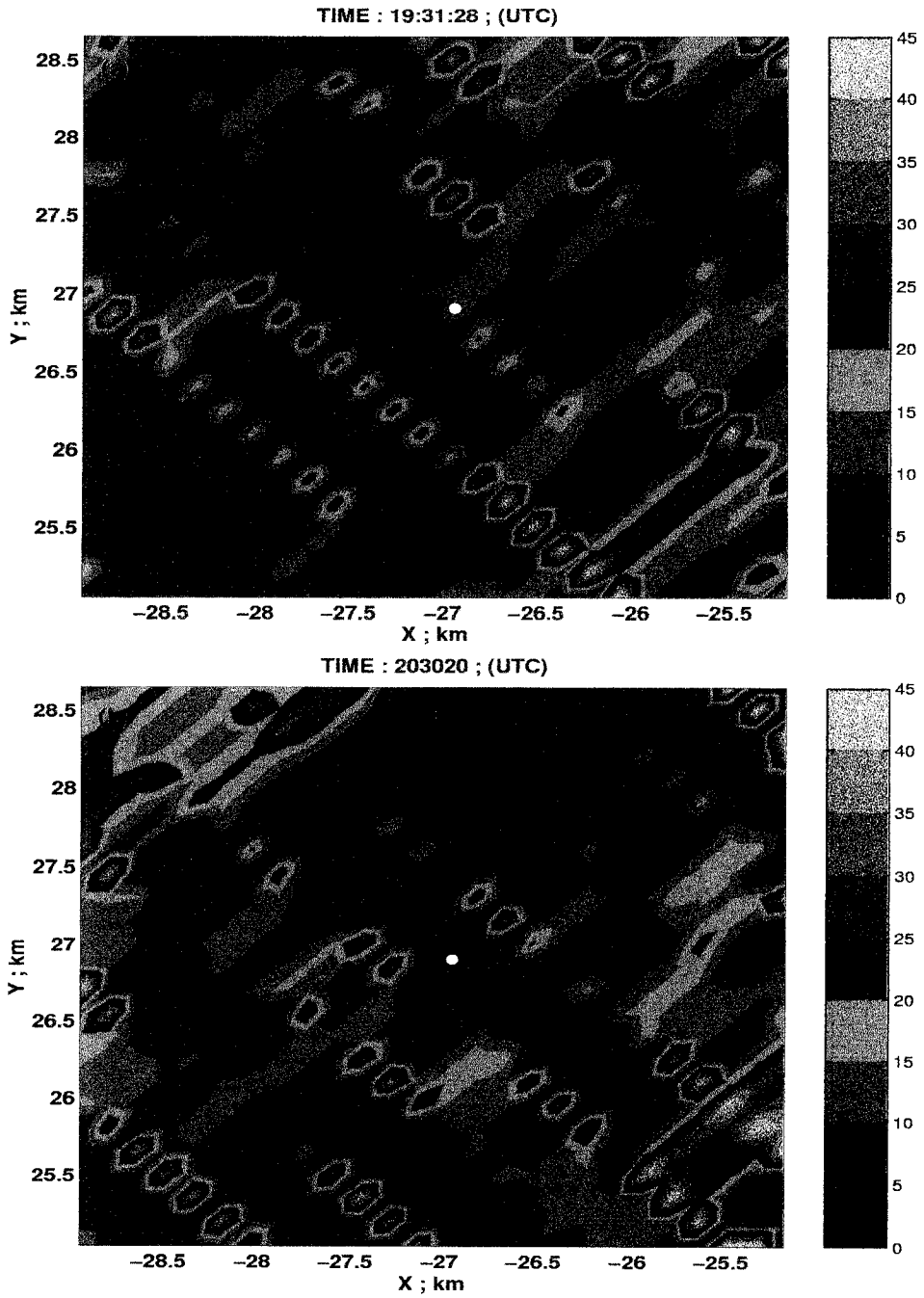

Figure 3.21: **(a)** The amplitude of Z_h gradient at 19:31 (UTC) on 17 September 1998. The white dot is the location of the profiler. **(b)** As in (a) except that time is 20:30 (UTC).

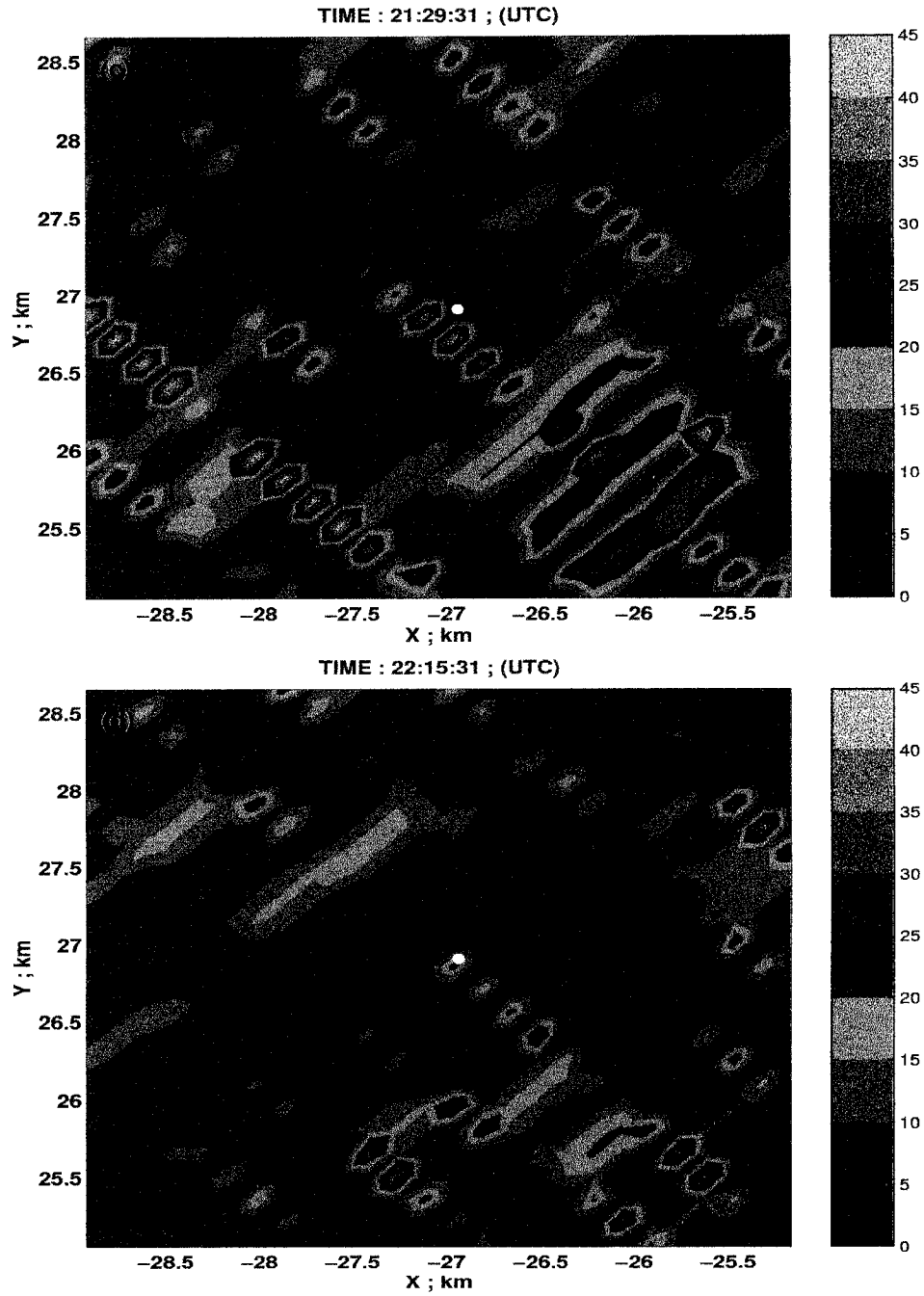

Figure 3.21: **(c) (d)** As in (a) except that time is 21:29 and 22:15 (UTC).

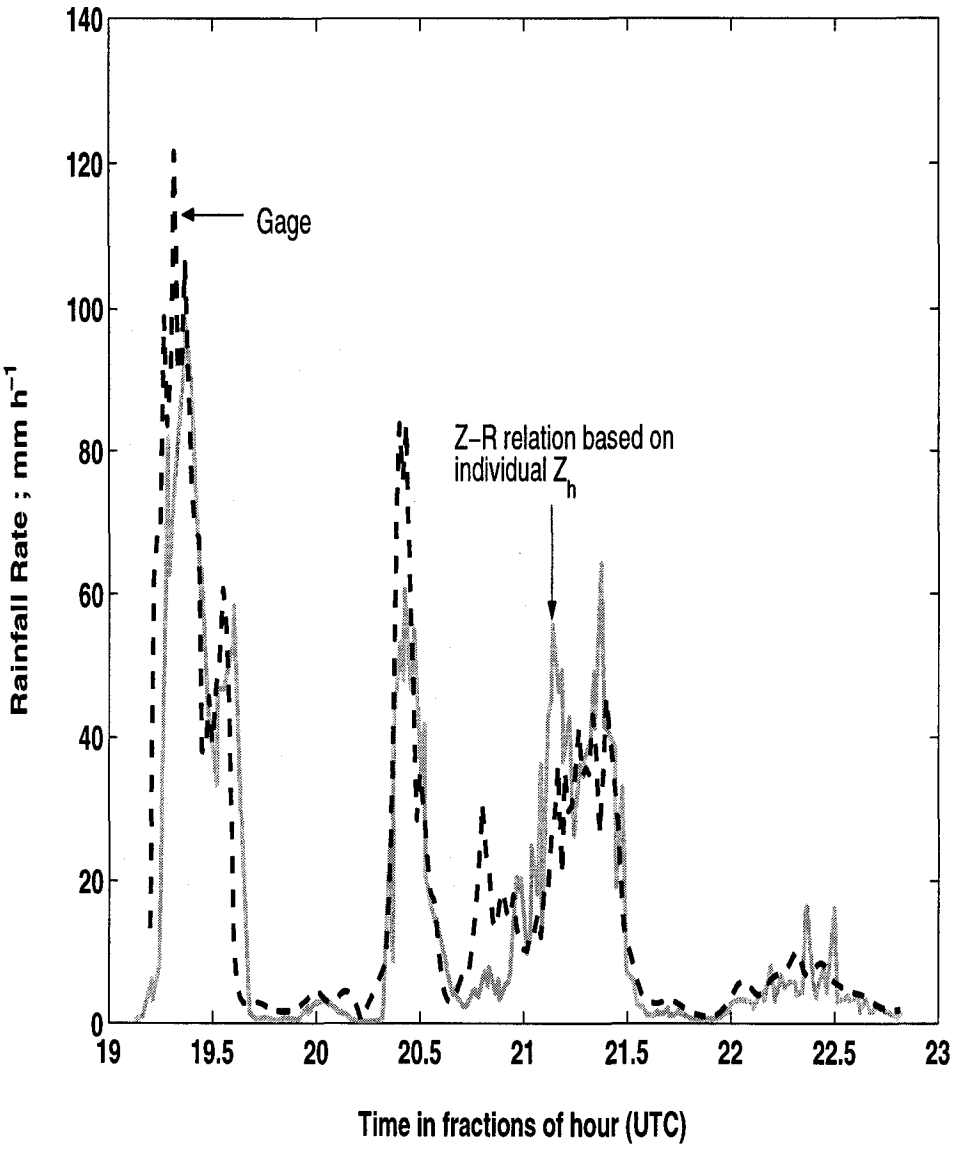

Figure 3.22: Gage rain rates compare with $R(Z_h)$ on 17 September 1998. Note that the coefficient of $R(Z_h)$ is based on averaging N_w and μ over a 1x1 km^2 area.

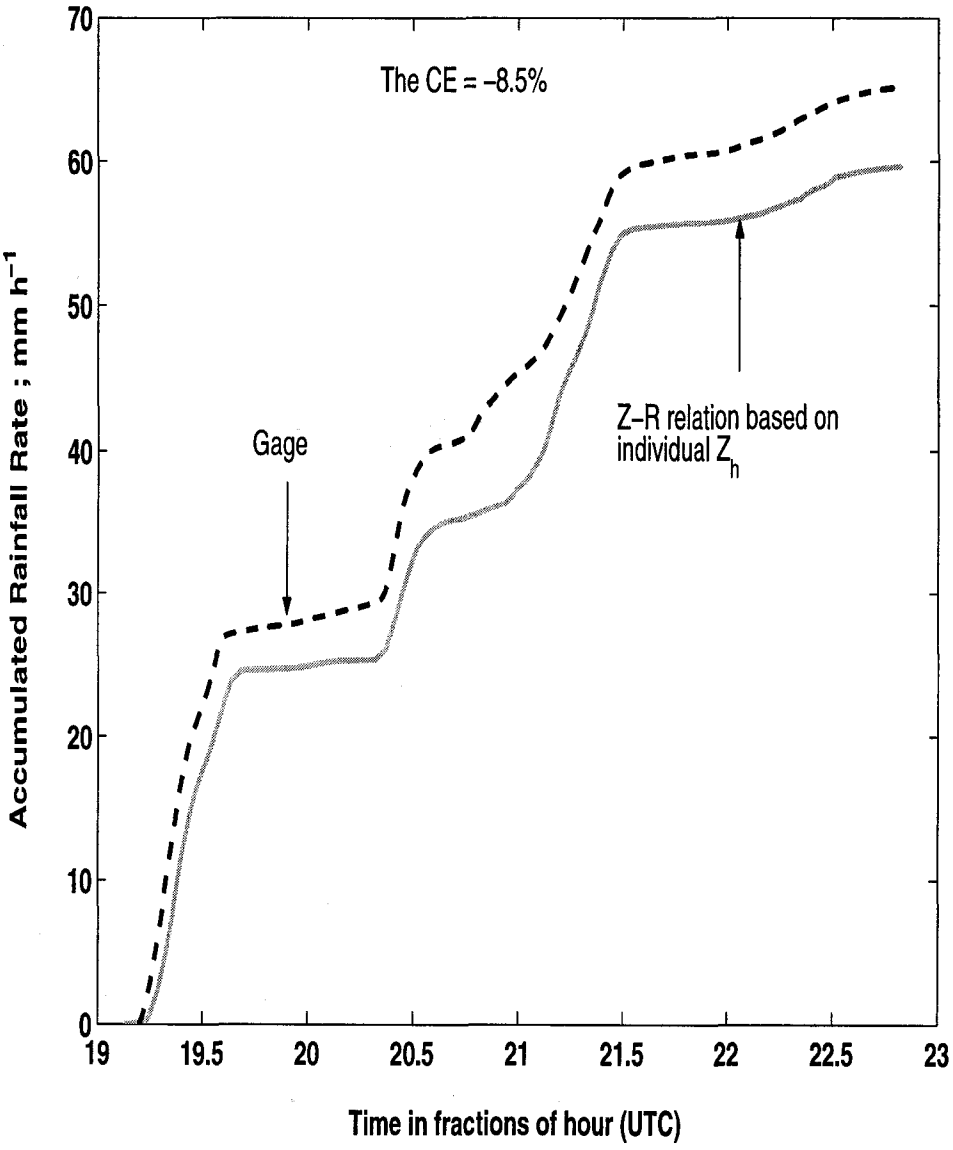

Figure 3.23: As in Fig. 3.22 except for cumulative rainfall.

Fig. 3.22 shows that the gage rain rates compare with $R(Z_h)$ whose coefficient is based on N_w and μ averaged over the 1x1 km^2 area. The Z-R agrees with gage rain rate very well except for a slight underestimate near the peaks. Again, the underestimate near the peaks may be due to radar beam smoothing. Fig. 3.23 shows the cumulative rain comparison with the cumulative error of 8.5% underestimate.

3.3 Summary

In this Chapter, we evaluated a method to retrieve dsd parameters (N_w, D_o and μ) from the radar measurement set (Z_h, Z_{dr} and K_{dp}) based on Gorgucci et al. (2001, 2002)[18, 14]. The method includes two parts. For those radar measurements which satisfy the threshold ($Z_h > 35\ dBZ$, $Z_{dr} > 0.2\ dB$ and $K_{dp} > 0.3\ ^o/km$), we estimate β by using (2-23) first, and then estimate D_0 by (3-10) and (3-12abc), N_w by (3-13abcd). The μ is estimated by using area averaging D_o, ξ_{dr} and area mode of β in (3-14abcde). For those radar measurements which do not satisfy the threshold, we assume that μ is equal to zero. The D_o is estimated by using (3-16a) ($Z_{dr} > 0.7\ dB$), (3-16b) ($0.7 > Z_{dr} > 0.2\ dB$), or (3-19) ($Z_{dr} < 0.2\ dB$ and $Z_h > 0\ dBZ$). N_w is estimated by applying D_o and Z_h in (3-18).

After retrieving the dsd parameters from radar measurements, we can calculate the coefficient of the Z-R relation for a area by applying averaged N_w and μ. Since the coefficient of the Z-R relation is estimated as an areal average, the noise and measured fluctuation could be averaged out. Moreover, we can calculate the rain rate at each individual resolution volume by applying this coefficient to a simple Z-R power law. Therefore, we gain not only the advantage of an areal rain rate algorithm but also keep the high spatial resolution. In addition, the fixed Z-R relation can cause severe bias because the fixed coefficient is not suitable for different rain types. The N_w-μ based Z-R relation proposed in this chapter can overcome this problem because its coefficient can be adjusted continuously and

robustly. Therefore, the N_w-μ based Z-R relation not only offers the simplicity of the usual Z-R relation but also can account for changes in rain types.

To validate our methodology, we analyzed two storm events, one from TRMM/LBA (Brazil) on 15 February 1999 and the other from TRMM/TEFLUN-B (Florida) on 17 September 1998. In each case, we retrieved dsd parameters from a large area which includes all gages in the gage network, and from a small area which is 1x1 km^2 with the NOAA profiler at the center. For the large area, we compared the dsd parameters and N_w-μ based Z-R relation with averaged gage rain rate (averaging over all gages and over a 2-minute interval). The dsd parameters seem to be quite reasonable and the two rain rates agree with each other very well (error less than 15.4% for the worst case). For the small area, we compared radar-retrieved dsd parameters with profiler-estimated dsd parameters. The results show that radar generally agrees with profiler (either sds or stat method). In the time interval when radar disagrees with the profiler significantly, we found that the profiler was located in a high Z_h gradient area or very close to a high Z_h gradient area. The high Z_h gradient may cause the disagreement between radar and profiler. We also compared the N_w-μ based Z-R with gage rain rate. These two rain rates agree with each other most of the time except for underestimate in the peaks. In the TRMM/LBA case, the error is large (-43.3%) because the radar values were smoothed by the beam in the strong rain cells. Since there were no such sharp rain cells in the TRMM/TEFLUN-B case, the error for the Florida case is small (-8.5%). Overall, the radar dsd parameters are very reasonable and the accuracy of N_w-μ based Z-R relation is acceptable for practical applications.

Chapter 4

DROP ORIENTATION AND CANTING ANGLE

In Section 3.1.1, we discussed one of the statistical properties of precipitation which is the drop size distribution (dsd). Other statistical properties are orientation and shape distributions. Basically, the drop shape is oblate spheroidal and the equilibrium shape is defined by the balance of drop surface tension ,gravity and aerodynamic forces (Green 1975; also see (2-19))[19]. However, falling raindrops exhibit steady state oscillations. There are two fundamental modes of oscillations, namely, the axisymmetric mode and the transverse mode. Fig. 4.1 shows a computer generated oscillation sequence for a 5 mm drop. The lower right panel shows the equilibrium shape, the two black panels show the transverse mode, the two white panels show the axisymmetric mode, and the four grey panels show multi-mode oscillations (mixture of the two fundamental modes). Since the horizontal and vertical polarization states of the radar transmitted wave are lined up along the major and minor axes of the oblate drop in the axisymmetric mode, the symmetry axis of the drop does not exhibit any orientation distribution. However, the transverse mode as well as the multi-mode oscillations will exhibit an orientation distribution with non-zero mean. This kind of orientation distribution is different from the orientation distribution due to turbulence which is known to be Gaussian distribution with zero mean and standard deviation less than about 5^o (Beard and Jameson 1983)[8].

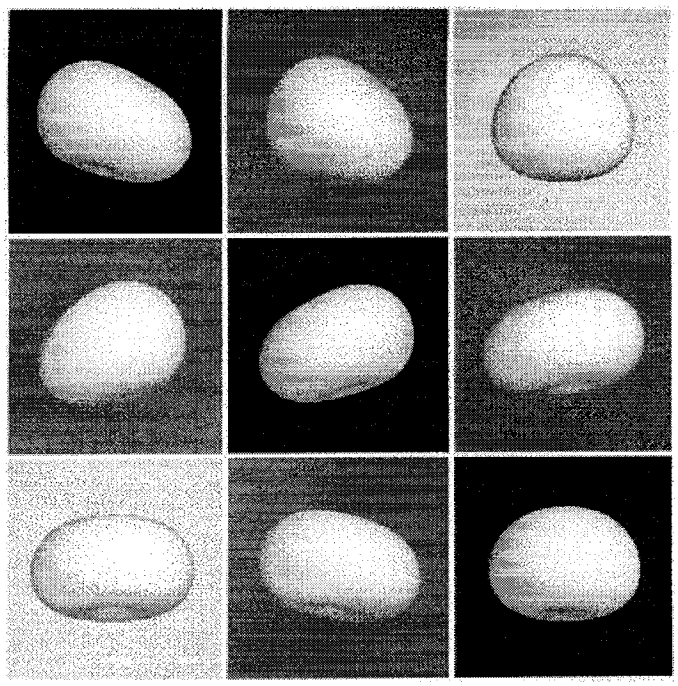

Figure 4.1: A computer-generated oscillation sequence. The lower right black panel is the equilibrium shape of a 5 *mm* drop, two other black panels (the diagonal panels) show the transverse oscillation mode, two white panels (upper right and lower left) show the axisymmetric oscillation mode, and the four grey panels show the mixed oscillation mode. Courtesy of Prof. Ken Beard, University of Illinois.

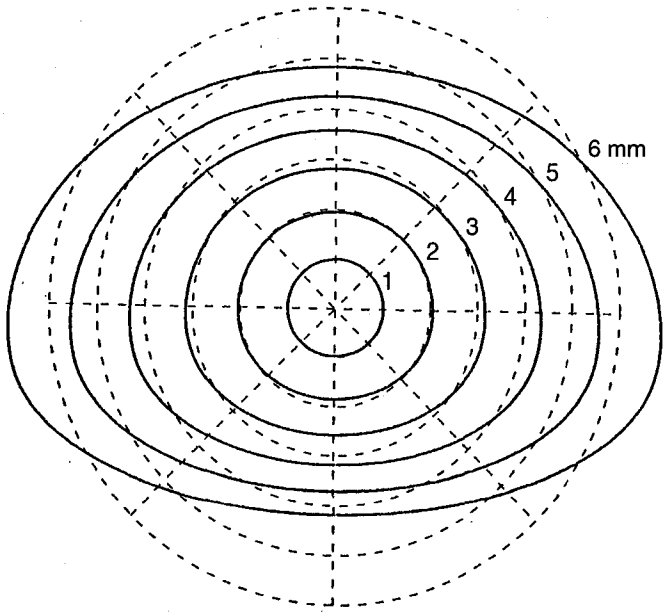

Figure 4.2: Equilibrium drop shape for drops of diameters 1-6 *mm*. From Beard and Chuang (1987)[7]

Fig. 4.2 shows the equilibrium drop shapes for diameters from 1-6 *mm*. If drops fall at their terminal velocity without wind shear or turbulence present, they will tend to be flat at the bottom with symmetry axis vertical (Beard et al. 1983)[8]. From Fig. 4.1, it is obvious that bottom planes of drops oscillating in the transverse mode or multi-mode are not parallel to the ground. It means that such drops will produce some orientation distribution in the θ direction with non-zero mean. Therefore, the canting angle distribution would be quite different from the usual Gaussian which is mainly due to turbulence. The polarization dependent radar parameters such as Z_{dr}, LDR, K_{dp} and so on are functionals of the canting angle distribution as well as the drop size distribution (dsd). Different canting angle models will impact the relation between those parameters as well as those algorithms using polarization dependent parameters. Therefore, it is important to understand the mechanism of drop orientation and corresponding radar observations. In this chapter, we will start from the relationship between drop orientation

and canting angle distribution, and then, compare different algorithms to estimate the standard deviation of the canting angle distribution. We will also try to develop a scheme to classify different canting angle models which arise due to turbulence or multi-mode oscillations.

4.1 Simulation of Canting Angle Distributions

Fig 4.3a,b illustrate the geometric relation between an axisymmetric target and the incident wave launched by the radar. Panel (a) of Fig 4.3 shows the segment **OZ** which is the local vertical and segment **ON** which is along the spheroid symmetry axis. The orientation of the axisymmetric target can be described by two angles, θ_b and ϕ_b. Note that subscript b refers to "body". The unit vectors $(\hat{h}_i,\hat{v}_i,\hat{k}_i)$ with origin **Q** are used to describe the polarization state of the incident wave launched by radar. The incident wave is assumed to propagate in the **XZ** plane along the **-X** direction. The shaded area represents the polarization plane of the incident wave. From panel (b), Ψ is the angle between $\hat{k}_i$ and $\hat{ON}$, and θ_i is the angle between segment **OZ** and $\hat{k}_i$ (see Fig 4.3b). Note that θ_i can be related to the conventional radar elevation angle ($\theta_i = 90^o$ means horizontal incidence and $\theta_i = 0^o$ means vertical incidence). Segment **QT** is the segment **ON** projected on the polarization plane, and segment **QV** is segment **OZ** projected on the polarization plane. The canting angle, β, is the angle between **QV** and **QT**.

Since $\hat{k}_i$ lies in the **XZ** plane (with $\phi_i = \pi$), it is possible to derive the following expression for $\hat{k}_i$, $\hat{v}_i$ and $\hat{h}_i$;

$$\hat{k}_i = -\sin\theta_i\hat{x} + \cos\theta_i\hat{z} \tag{4-1a}$$

$$\hat{h}_i = -\hat{y} \tag{4-1b}$$

$$\hat{v}_i = -\cos\theta_i\hat{x} - \sin\theta_i\hat{z} \tag{4-1c}$$

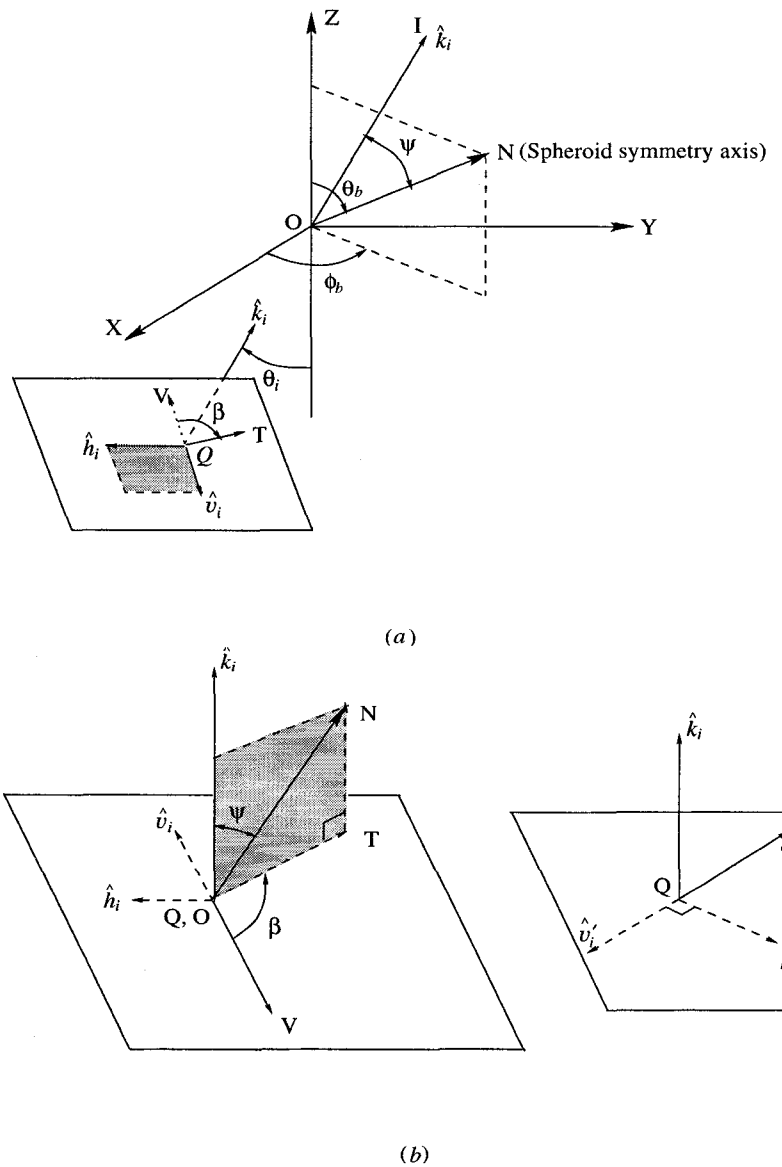

Figure 4.3: **(a)** The geometric illustration of drop orientation adapted from Holt (1984)[22]. The spheroid symmetry axis is oriented along **ON**. The incident wave propagates along **-X** direction on **XZ** plane. $\hat{k}_i$ is the incident wave vector which is orthogonal to the polarization plane (shade area and construct by $\hat{h}$ and $\hat{v}$). **(b)** The polarization plane is moved to the origin of body coordinates (**X**, **Y** and **Z**). Note that **QT** is **ON** projected on polarization plane.

The unit vector along the segment **ON** is,

$$\hat{ON} = \cos\phi_b \sin\theta_b \hat{x} + \sin\phi_b \sin\theta_b \hat{y} + \cos\theta_b \hat{z} \tag{4-2}$$

From Fig 4.3 and applying (4-1a) and (4-2), the relation between the drop orientation angle and the canting angle can be expressed as (Holt 1984)[22],

$$\cos\beta \sin\Psi = \cos\theta_b \sin\theta_i + \sin\theta_b \cos\theta_i \cos\phi_b \tag{4-3a}$$

$$\sin\beta \sin\Psi = \sin\theta_b \sin\phi_b \tag{4-3b}$$

For horizontal incidence ($\theta_i = \pi$), (4-3a,b) can be combined into,

$$\tan\beta = \tan\theta_b \sin\phi_b \tag{4-4}$$

Equation (4-4) is the simplified relation between orientation angles (θ_b and ϕ_b) and canting angle (β). This equation will be applied to simulations performed in this chapter.

4.1.1 1-D Distribution to Distribution over a Spherical Surface

Traditionally, the effects of scattering by a precipitation target is described by the scattering matrix (van de Hulst, 1950; Saxon, 1955; also see Section 1.1.2 in this thesis)[55, 46]. Holt (1984)[22] has shown that the scattered electric field can be expressed as,

$$\begin{bmatrix} E_h^s \\ E_v^s \end{bmatrix} = \begin{bmatrix} S_{11}\cos^2\beta + S_{22}\sin^2\beta & (S_{11} - S_{22})\cos\beta\sin\beta \\ (S_{11} - S_{22})\cos\beta\sin\beta & S_{11}\sin^2\beta + S_{22}\cos^2\beta \end{bmatrix} \begin{bmatrix} E_h^i \\ E_v^i \end{bmatrix} \frac{exp(jk_o r)}{r} \tag{4-5}$$

where $S_{11,22}$ are the principal plane scattering amplitude elements and β is the canting angle (see Fig. 4.3). Theoretically, $S_{11,22}$ can be computed by using the T-matrix method, Rayleigh approximations or Mie solution depending on axis ratio and drop size parameter. For an assembly of scatterers, the elements of scattering

matrix should be integrated over drop size distribution (dsd) and drop orientation distribution as,

$$S_{hh} = \int_0^{D_{max}} \int_\Omega (S_{11}\cos^2\beta + S_{22}\sin^2\beta) N(D) p_\Omega(\theta_b, \phi_b) dD d\Omega \qquad (4\text{-}6)$$

where p_Ω is probability density function (pdf) of θ_b and ϕ_b defined on a spherical surface, Ω is solid angle and $d\Omega = \sin\theta_b d\theta_b d\phi_b$. Note that β and Ψ are functions of θ_b and ϕ_b (see (4-3a)).

Since there is no evidence showing that θ_b and ϕ_b are related to each other or that ϕ_b will tend to any special angle, we usually assume that the distributions of θ_b and ϕ_b are independent and that ϕ_b is uniform from 0 to 2π. Therefore, the integral of p_Ω is,

$$\begin{aligned} \int_\Omega p_\Omega(\theta_b, \phi_b) d\Omega &= \int_\Omega p_{\theta\Omega}(\theta_b) p_{\phi\Omega}(\phi_b) \sin\theta_b d\theta_b d\phi_b \\ &= \int_{\theta_b}\int_{\phi_b} p_\theta(\theta_b) p_\phi(\phi_b) d\theta_b d\phi_b \end{aligned} \qquad (4\text{-}7)$$

From the equations above, we can directly get,

$$p_{\theta\Omega}(\theta_b) = \frac{p_\theta(\theta_b)}{\sin\theta_b} \qquad (4\text{-}8a)$$

$$p_{\phi\Omega}(\phi_b) = p_\phi(\phi_b) \qquad (4\text{-}8b)$$

Holt (1984)[22] and Jameson (1987)[28] also show a similar result as above. In the following simulation, we will study the relation of canting angle (β) and orientation angles (θ_b, ϕ_b) by combining (4-4) and (4-8a,b).

Based on turbulence theory, Beard et al. (1983)[8] have shown that the distribution of $\tan\beta$ is Gaussian with zero mean and $\sigma_\beta < 5^o$ and can be expressed as,

$$p(\beta) = \frac{1}{\cos^2\beta (2\pi\sigma^2_{\tan\beta})^{1/2}} exp(-\tan^2\beta/(2\sigma^2_\beta)) \qquad (4\text{-}9)$$

Note that the exponent of this equation was corrected by Metcalf (1988)[38]. For small σ_β, the difference between Gaussian distribution of β and Gaussian distribution of $\tan\beta$ is very small. So most researchers assume that the canting angle distribution due to turbulence is Gaussian. In order to 1) correctly separate the shape effects and orientation effects and 2) clearly describe the canting angle distribution for a nonzero elevation angle, we have to know not only the distribution of β but also the distribution of the orientation (θ_b and ϕ_b). By assuming that the distributions of θ_b and ϕ_b are independent, and ϕ_b is uniform distribution in (0,2π), Metcalf (1988)[38] and Jameson (1987)[28] have shown that a Gaussian distribution of θ_b on a spherical surface will give a Gaussian distribution of β with $\sigma_\theta = \sigma_\beta$.

Fig. 4.4 shows the results of simulations to show the relation of canting angle (β) and orientation angle (θ_b; ϕ_b is uniform distribution in (0,2π)). In these simulations, we first simulate θ_b which is Gaussian distribution on a spherical surface ($p_\Omega(\theta_b)$ is Gaussian with zero mean). Second, we simulate a uniform distribution for ϕ_b. By applying (4-4) we can compute β from θ_b and ϕ_b. The results show that σ_β is very close to σ_θ in agreement with Metcalf (1988)[38] and Jameson (1987)[28].

4.1.2 Relation between Fisher Distribution and Gaussian Distribution

As we discussed in the previous section, the Gaussian distribution is most commonly assumed to describe the orientation distribution. This description is an approximation and is only good for small σ_θ. Bringi and Chandrasekar (2001, Chapter 2.3.6)[9] suggested that the Fisher distribution function may be the best way to describe the distribution of orientation angles on a spherical surface. The Fisher distribution function (Mardia, 1972)[33] is given by,

$$g(\theta_b, \phi_b) = \frac{\kappa \sin\theta_b}{4\pi \sinh(\kappa)} e^{\kappa[\cos\bar{\theta}_b \cos\theta_b + \sin\bar{\theta}_b \sin\theta_b \cos(\phi_b - \bar{\phi}_b)]} \tag{4-10}$$

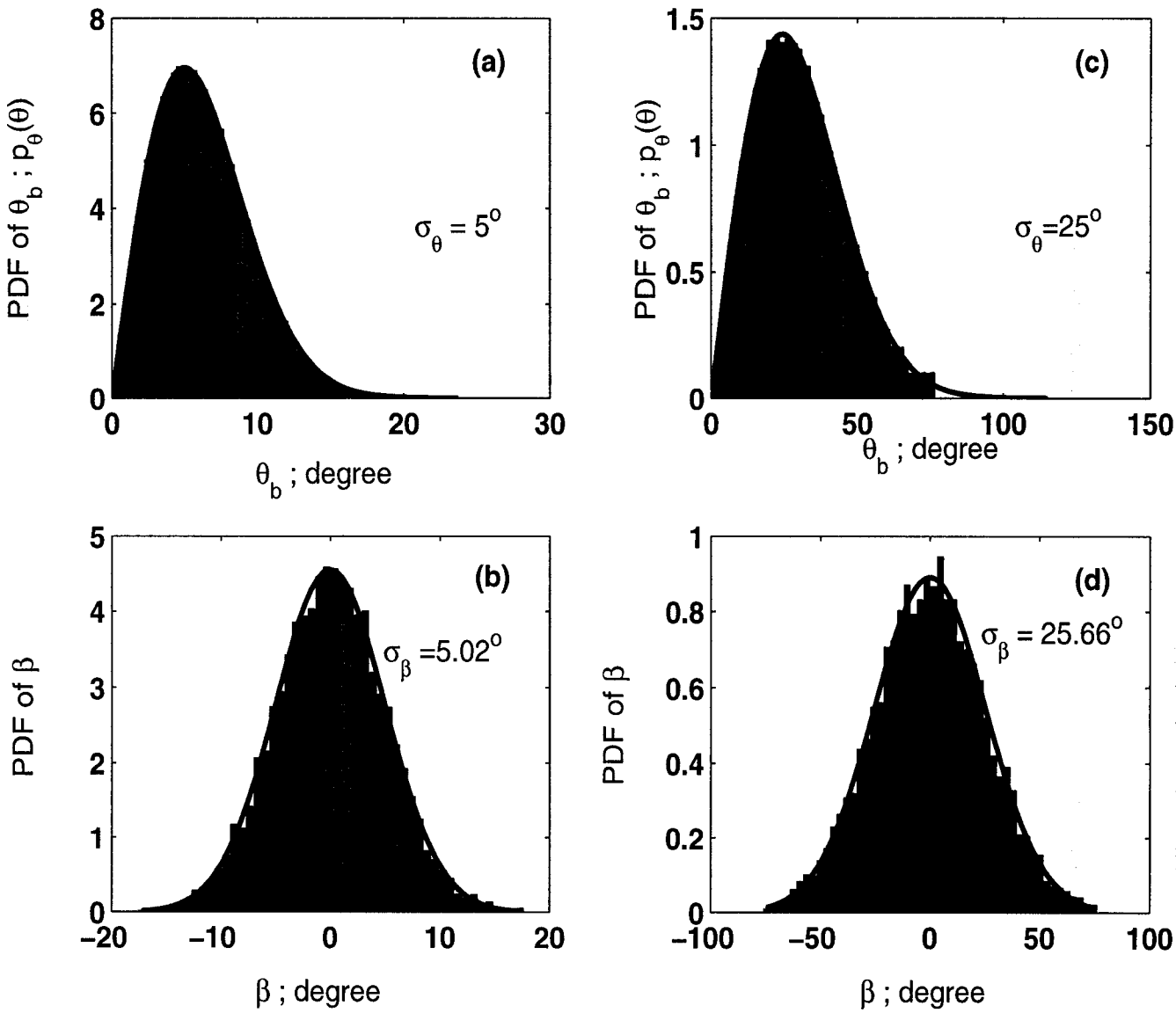

Figure 4.4: **(a),(b)** Computer simulation to express the relation between canting angle (β) and orientation angle (θ_b). The distribution of θ_b on spherical surface ($p_\Omega(\theta_b)$) is Gaussian with zero mean and $\sigma_\theta = 5^o$. Panel (a) is the normalized histogram of θ_b (bar) compared with PDF of θ_b ($p(\theta_b)$; solid line). Note that $p(\theta_b) = p_\Omega(\theta_b) \sin\theta_b$ (also see (4-8a)) and distribution of ϕ_b is uniform in $(0,2\pi)$. Panel (b) is normalized histogram of β (bar) compared with Gaussian PDF (solid line). The standard deviation of β is 5.02^o. **(c),(d)** Same as (a),(b) except $\sigma_\theta = 25^o$ and $\sigma_\beta = 25.66^o$.

where $\bar{\theta}_b$ and $\bar{\phi}_b$ are the mean of θ_b and ϕ_b, and κ is the shape parameter. If θ_b is symmetric about the vertical, then $\bar{\theta}_b$ is zero, and (4-10) becomes,

$$\begin{aligned} g_\Omega(\theta_b, \phi_b) &= \frac{\kappa e^{\kappa \cos\theta_b}}{4\pi \sinh(\kappa)} \\ &= \frac{\kappa}{2\pi(1-e^{-2\kappa})} e^{-\kappa(1-\cos\theta_b)} \end{aligned} \tag{4-11}$$

For Gaussian distribution of θ_b on a spherical surface, the PDF form should be,

$$p_\Omega(\theta_b) = Ce^{-0.5(\frac{\theta_b}{\sigma_\theta})^2} \tag{4-12}$$

where C is normalization factor. We use C instead of the standard Gaussian normalization because θ_b is physically limited in the $(0,\pi/2)$ interval. Since Gaussian distribution of θ_b with small σ_θ on a spherical surface will lead to Gaussian distribution of β on the polarization plane, it means that the Fisher distribution should be very close to the Gaussian distribution when σ_θ is small. If (4-11) and (4-12) are equal, the exponents should be the same. So the relation between κ and σ_θ is,

$$\kappa = \frac{\theta_b^2}{2(1-\cos\theta_b)\sigma_\theta^2} \tag{4-13}$$

Since σ_θ is small and $(0,2\sigma_\theta)$ interval will contribute more than 95% probability for Gaussian distribution, we found that $\theta_b^2/(1-\cos\theta_b)$ is almost constant (between 2 to 2.0832 with mean equal to 2.0285) for θ_b in $(0^o,40^o)$ interval (see Fig. 4.5). For $\sigma_\theta \leq 20^o$, we can set $\theta_b^2/(1-\cos\theta_b) \approx 2.0285$ and the relation between κ of the Fisher distribution and σ_θ is,

$$\kappa = \frac{2.0285}{2\sigma_\theta^2} \tag{4-14}$$

Fig. 4.6 compares the Fisher distribution and Gaussian distribution on a spherical surface with $\sigma_\theta = 5^o$, 10^o, 15^o and 20^o by applying (4-14). The Fisher distribution form is given by (4-11) and is the grey-bold-dash line in the figure. The

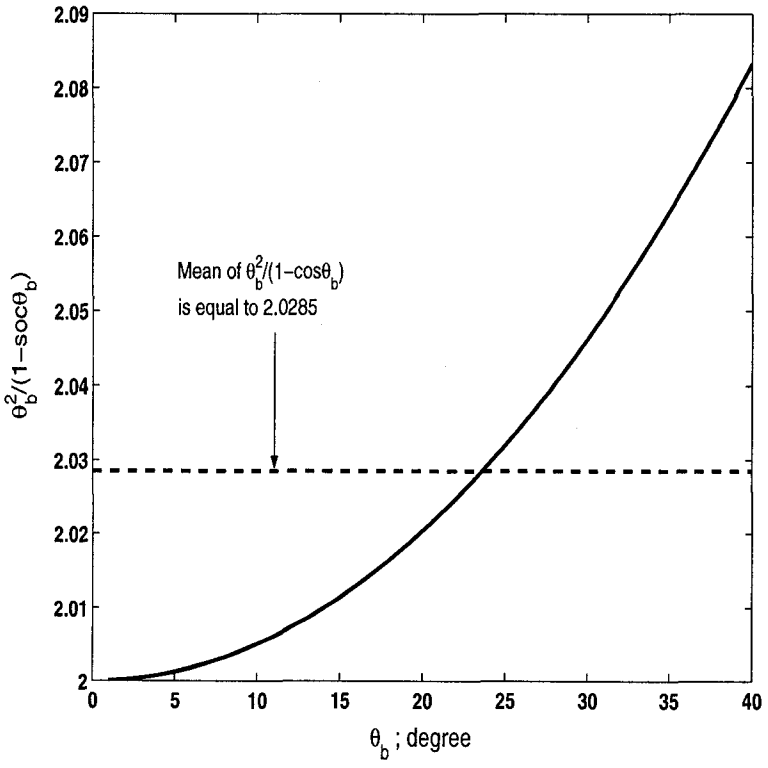

Figure 4.5: $\theta_b^2/(1-\cos\theta_b)$ versus θ_b. The dash line is the mean value and is equal to 2.0285.

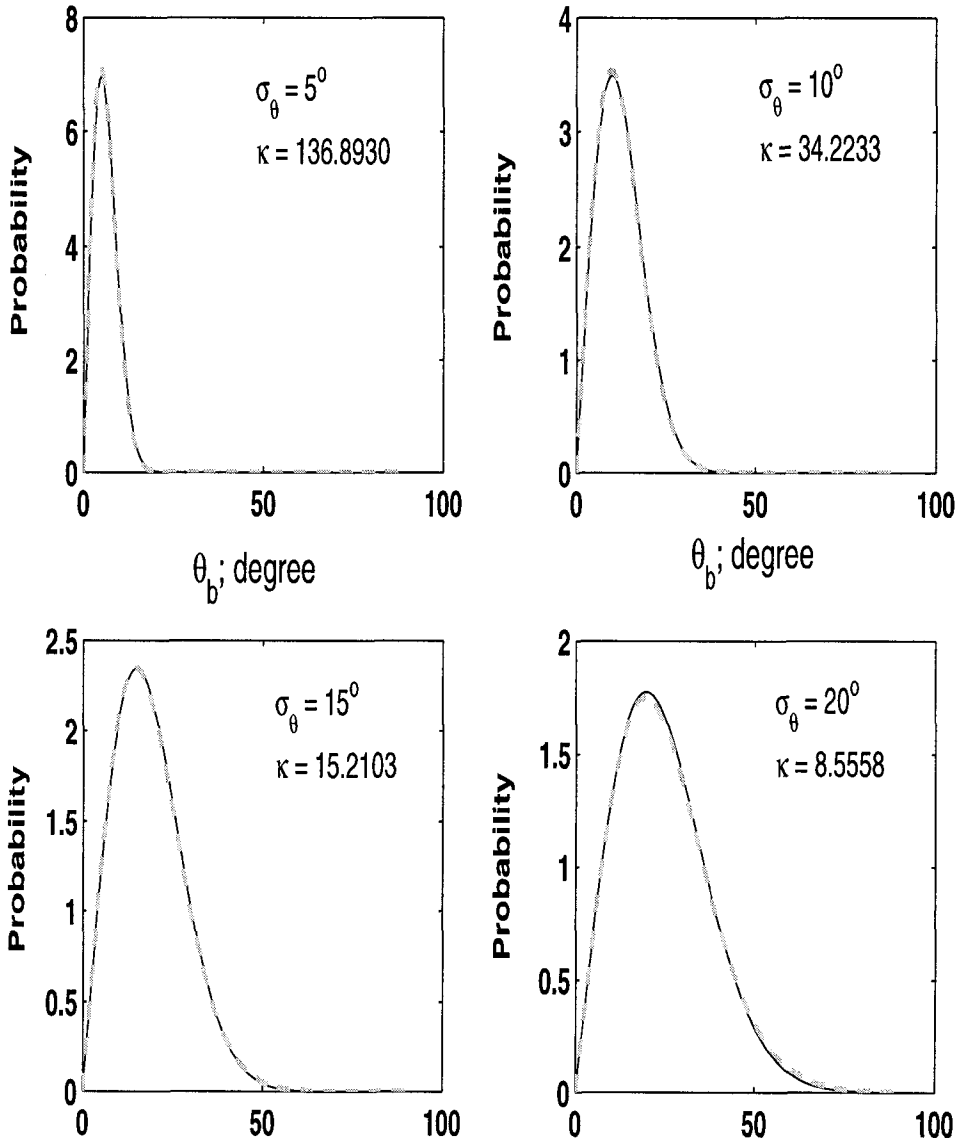

Figure 4.6: Fisher distribution compared with Gaussian distribution on a spherical surface. The grey-bold-dash line is the Fisher distribution and black-thin-solid line is the Gaussian distribution. The Gaussian form (p_Ω) is (4-12) and the solid line is $p(\theta_b) = p_\Omega(\theta_b) \sin\theta_b$ (see (4-8a))

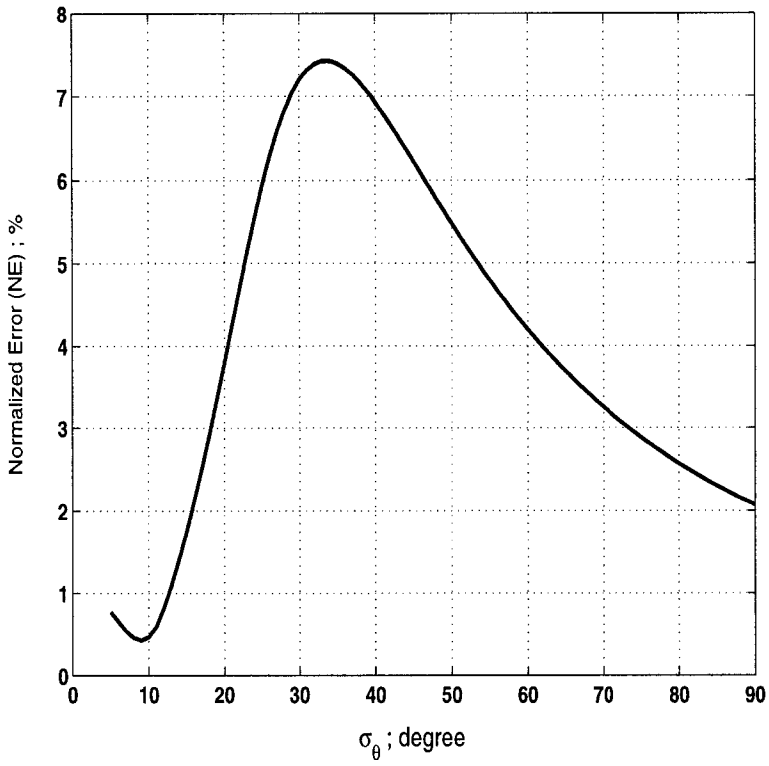

Figure 4.7: The normalized error (NE) between the Fisher distribution and the Gaussian distribution. The NE is less than 5% when σ_θ is less than 20^o.

black-thin-solid line is $p(\theta_b) = p_\Omega(\theta_b)\sin\theta_b$ where $p_\Omega(\theta_b)$ is Gaussian form given by (4-12). Fig. 4.7 shows the normalized error between Fisher distribution and Gaussian distribution on a spherical surface ($p(\theta_b)$). The normalized error (NE) was defined in (2-31a) in Chapter 2.3.1 in this thesis. The normalized error is less than 5% when σ_θ is less than 20^o. Actually, NE is never greater than 8%. So (4-14) can hold even when σ_θ is great than 20^o. To summarize, the Gaussian form is a very good descriptor to describe drop orientation over a spherical surface if $\sigma_\theta < 20^o$.

4.1.3 Holt's Distribution

Holt (1984)[22] studied the distribution of canting angles and performed angle integrations over canting angles. He suggested a way to describe the distribution of orientation angles (θ_b and ϕ_b) on a spherical surface as,

$$\begin{aligned} \Delta(\theta_b) &= \frac{\Gamma}{1 + A^2[\cos\theta_b - \cos\theta_{b0}]^2} \\ \Gamma &= \frac{A}{\tan^{-1}[A(1-x_o)] + \tan^{-1}[A(1+x_o)]} \end{aligned} \tag{4-15}$$

where $x_o = \cos\theta_{b0}$ and A is the shape parameter to control the width of the distribution. Fig. 4.8 shows $\Delta(\theta_b)$ versus θ_b with $A = 1000$, 100 and 10. The peak value of $\Delta(\theta_b)$ locates at $\theta_b = \theta_{b0}$ and the distributions are more narrow when A values1 are larger.

In order to better understand the relation between orientation distribution and canting angle distribution, we performed a series of simulations. We fixed A equal to 1000 and changed θ_{b0} from 1^o to 10^o. Since the Holt distribution function is not a common PDF such as uniform, Gaussian or Gamma distribution, it is difficult to generate random variables with this distribution directly. We know that any curve can be approximated as combination of many flat segments. First,

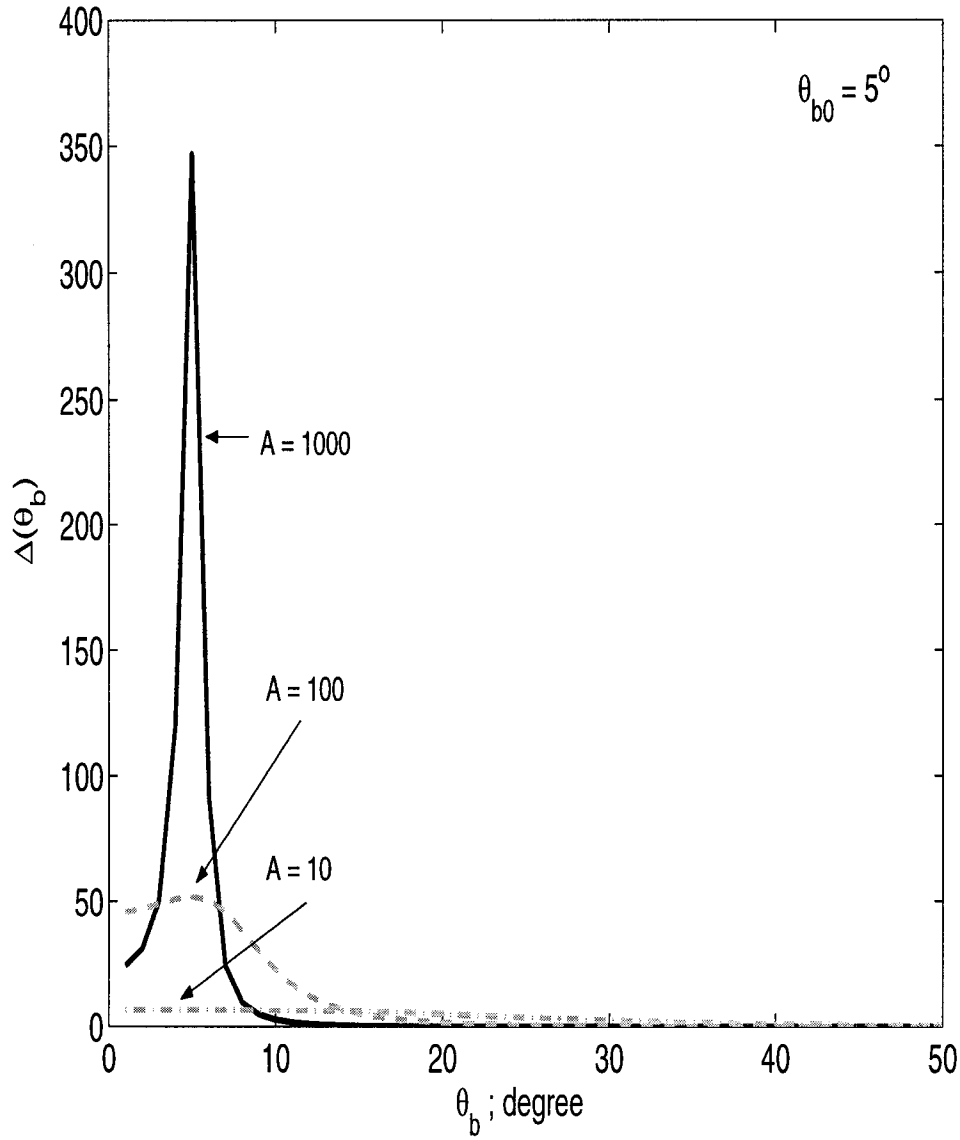

Figure 4.8: The distribution function of θ_b as suggested by Holt (1984). The θ_{b0} is 5^o and $A = 1000$, 100 and 10.

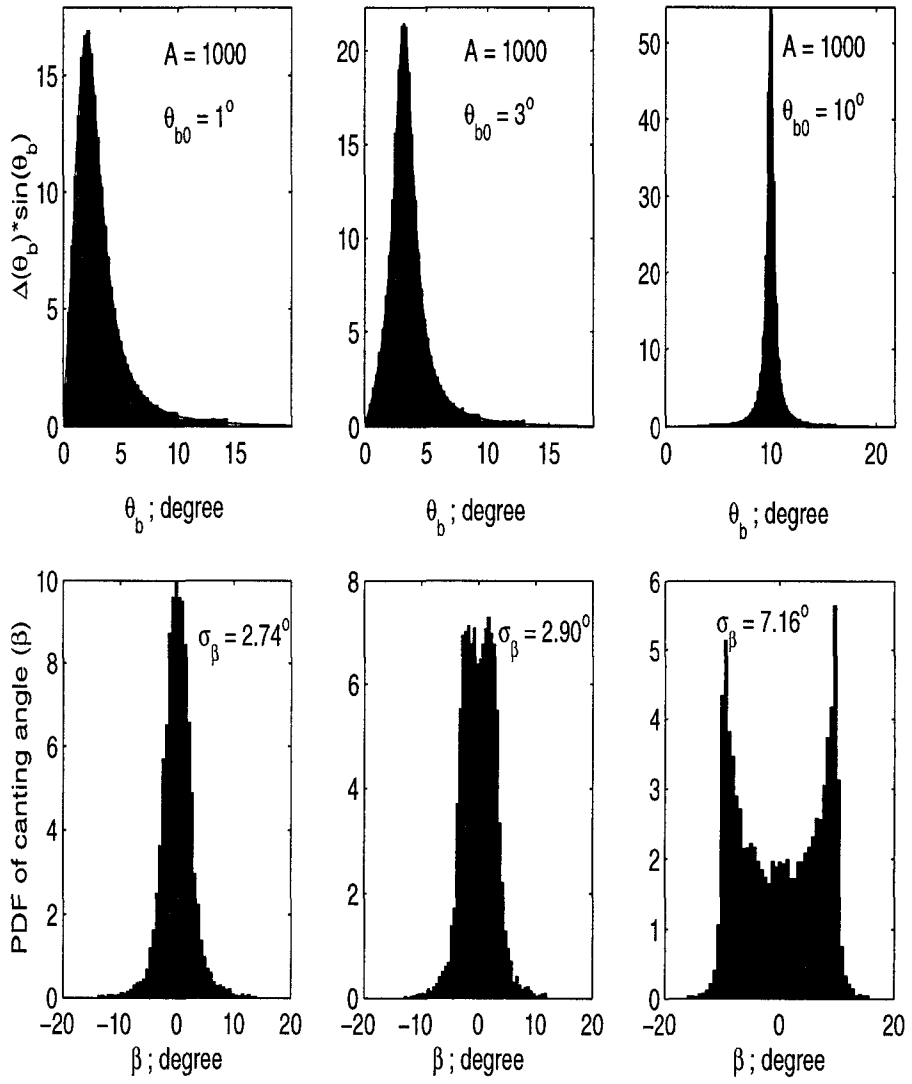

Figure 4.9: Computer simulations for orientation angles (θ_b) and canting angles (β) for different θ_{b0}. The A is fixed at 1000. Note that β is close to narrow Gaussian distribution when θ_{b0} is close to 0^o ($\theta_b = 1^o$), and becomes bi-modal when θ_{b0} becomes larger ($\theta_{b0} = 10^o$).

we divide $(0,\pi)$ into 1000 equal space intervals, and then covert Holt PDF to PMF. Second, we find the lowest and highest truncated points, $\theta_{b,min}$ and $\theta_{b,max}$, whose probabilities are $1/N$ where N the total amount of data points. Once again, we divide $(\theta_{b,min} - 0.001, \theta_{b,max} + 0.001)$ into 3000 equal space intervals and convert from Holt PDF to PMF. From Holt PMF, we calculate total amount of data points in each interval and let those data points be distributed uniformly in the interval. Finally, we redistribute all data points randomly. So θ_bs are pseudo-random variables with Holt PDF. After obtaining θ_b and ϕ_b which are uniform distributions, we can compute β and σ_β using (4-4). Since θ_bs are pseudo-random, they agree with theoretical values very well. The calculated σ_β is stable and should be very close to its theoretical value.

Fig. 4.9 shows the results. The canting angle distribution is close to narrow Gaussian with zero mean ($\sigma_\beta = 2.74^o$) when θ_{b0} is close to zero (1^o). It becomes a rectangle distribution with zero mean ($\sigma_\beta = 2.90^o$) when $\theta_{b0} = 3^o$. Finally, the canting angle distribution becomes bi-modal with symmetry along 0^o ($\sigma_\beta = 7.16^o$) when θ_{b0} is large (10^o). We will use last case with θ_{b0} equal to 10^o to test the impact of non-Gaussian distributions on different radar-based canting angle estimators.

4.2 Canting Angle Estimation Using Radar Data

Since drop orientation can affect dual-polarization radar measurements significantly, it is important to develop a good algorithm to estimate the drop canting angle. In this section we discuss two canting angle estimators proposed by Hendry et al. (1987)[20] and Ryzhkov (2001)[42]. Moreover, we propose a new algorithm based on the asymmetric ratio (A_{sy}; Kwiatkowski, 1995)[31].

4.2.1 ρ_4 Method

In order to study the impact of canting angle on radar observation, Hendry et al. (1987)[20] started with the complex voltage induced at the right-hand circular

port of a dual-circular radar. By applying basis transformations (see Chapter 1), it is possible to derive the cross-polar scattering matrix element (S'_{12}) as a function of the slant linear polarization state as (also see Chapter 6, Bringi and Chandrasekar, 2001)[9],

$$\langle |S'_{12}|^2 \rangle = \frac{\langle \eta_c |\nu|^2 \rangle}{2} [1 + \rho_4 \cos(4\beta_o - 4\phi)] \tag{4-16}$$

where η_c is back scatter cross section, ν can be related to circular depolarization ratio (CDR) as $CDR = \langle \eta_c |\nu|^2 \rangle / \langle \eta_c \rangle$ and ϕ is related to orientation angle (Ψ) as $\Psi = (\pi/4 - \phi)$ (see Fig. 4.3). The ρ_4 is an important quantity directly related to the canting angle distribution and defined as

$$\rho_4 = \int_{-\pi/2}^{\pi/2} \cos 4(\beta - \beta_o) p(\beta - \beta_o) d(\beta - \beta_o) \tag{4-17}$$

where β_o is mean canting angle, $p(\beta)$ is pdf of canting angle and is assumed to be symmetric along β_o. The advantage of using ρ_4 is that ρ_4 is measurable. From (4-16), we can calculated ρ_4 by measuring maximum and minimum of the cross-polar power (P_{cr}) as,

$$\frac{(P_{cr})_{max}}{(P_{cr})_{min}} = \frac{1 + \rho_4}{1 - \rho_4} \tag{4-18}$$

In practice, we can measure the 3x3 covariance matrix in (H,V) basis and then use (1-17) and (1-18) by setting ellipticity angle, $\tau = 0^o$, for linear polarization. After rotating the basis (changing tilt angle), we can get maximum and minimum cross-power. For a Gaussian canting angle distribution, ρ_4 is a function of standard deviation of canting angle (σ_β) as,

$$\rho_4 = \exp(-8\sigma_\beta^2) \tag{4-19}$$

Hendry et al. (1987)[20] also show that ρ_4 is not very sensitive to the form of the distribution of canting angle. Therefore, (4-19) can also be applied to a non-Gaussian distribution which is symmetric along β_o.

Instead of rotating the polarization basis, there is a simple way to estimate ρ_4. The 3x3 covariance matrix, $\mathbf{\Sigma}_o$, measured in (H,V) basis is given in (1-16). Since we are considering a linear basis, the polarization ratio, χ, can be simplified by setting $\tau = 0^o$ in (1-10a,b) and expressed as,

$$\chi = \frac{\sin 2\theta_t}{1 + \cos 2\theta_t} \tag{4-20}$$

Insert (4-20) into (1-17), the transformation matrix, $\mathbf{T}$, can be simplified as,

$$\mathbf{T}(\chi)|_{\tau=0^o} = \begin{bmatrix} \frac{1}{2}b & \frac{\sqrt{2}}{2}a & \frac{1}{2}(\frac{a^2}{b}) \\ -\frac{\sqrt{2}}{2}a & b-1 & \frac{\sqrt{2}}{2}a \\ \frac{1}{2}(\frac{a^2}{b}) & -\frac{\sqrt{2}}{2}a & \frac{1}{2}b \end{bmatrix} \tag{4-21}$$

where $a = \sin 2\theta_t$ and $b = 1 + \cos 2\theta_t$. By using basis transformation (see (1-18)), the cross-polar power is proportional to $\mathbf{\Sigma}'(2,2)$ which is expressed as,

$$\begin{aligned} \mathbf{\Sigma}'(2,2) \;=\; & \frac{1}{2}a^2\langle|S_{hh}|^2\rangle - a(b-1)\langle S_{hv}S_{hh}^*\rangle - \frac{a^2}{2}\langle S_{vv}S_{hh}^*\rangle \\ & -a(b-1)\langle S_{hh}S_{hv}^*\rangle + 2(b-1)^2\langle|S_{hv}|^2\rangle + a(b-1)\langle S_{vv}S_{hv}^*\rangle \\ & -\frac{a^2}{2}\langle S_{hh}S_{vv}^* + a(b-1)\langle S_{hv}S_{vv}^*\rangle + \frac{1}{2}a^2\langle|S_{vv}|^2\rangle \end{aligned} \tag{4-22}$$

Since ϕ_b is uniform distribution between 0^o to 360^o, the distribution of canting angle (β) should be symmetric about $\beta_o = 0^o$ no matter what the distribution of θ_b is. In this case, the minimum cross-polar power should be at $\theta_t = 0^o$, and maximum cross-power at $\theta_t = 45^o$. Therefore, the minimum and maximum cross-polar power expressions reduce to,

$$(P_{cr})_{min} \propto \mathbf{\Sigma}'(2,2)|_{\theta_t=0^o} \;=\; 2\langle|S_{hv}|^2\rangle \tag{4-23a}$$

$$(P_{cr})_{max} \propto \mathbf{\Sigma}'(2,2)|_{\theta_t=45^o} \;=\; \frac{1}{2}\langle|S_{hh}|^2\rangle + \frac{1}{2}\langle|S_{vv}|^2\rangle - Re\left[\langle S_{hh}S_{vv}^*\rangle\right] \tag{4-23b}$$

From (4-23a,b), we find that co-cross correlation coefficients do not affect ρ_4 estimation if mean canting angle, β_o, is zero. However, we should be very careful in using the simplified formula of (4-23a,b) because the tilt of the radar antenna could effectively produce an extra canting angle (Huang et al., 2001)[24]. In this case, the mean canting angle will not be zero and the simplified formula is no longer true.

4.2.2 Ryzhkov Method

Ryzhkov proposed a different method to estimate the mean canting angle and standard deviation of canting angle from the covariance matrix (Ryzhkov 2001)[42]. He started with a single drop oriented as in Fig. 4.3. By applying Rayleigh scattering, the scattering matrix in (H,V) basis can be expressed as,

$$\mathbf{S} = \begin{bmatrix} (f_a - f_b)\sin^2\Psi\sin^2\beta + f_b & (f_a - f_b)\sin^2\Psi\sin\beta\cos\beta \\ (f_a - f_b)\sin^2\Psi\sin\beta\cos\beta & (f_a - f_b)\sin^2\Psi\cos^2\beta + f_b \end{bmatrix} \quad (4\text{-}24)$$

where f_a is the scattering amplitude when $\vec{E}^i$ is parallel to symmetry axis and f_b is the scattering amplitude when $\vec{E}^i$ is perpendicular to symmetry axis. Although this equation is based on Rayleigh scattering, it holds upto 35 GHz for oblate drops when $\Psi \geq 80^o$. Since drop shapes and orientations are assumed to be independent, we can treat $f_{a,b}$ and orientation angle (Ψ and β) separately. For example, the $\langle|S_{hh}|^2\rangle$ can be expressed as,

$$\begin{aligned} \langle|S_{hh}|^2\rangle &= \langle|f_a - f_b|^2\rangle\langle\sin^4\Psi\sin^4\beta\rangle + \langle|f_b|^2\rangle \\ &\quad +2Re\left[\langle(f_a - f_b)f_b^*\rangle\right]\langle\sin^2\Psi\sin^2\beta\rangle \end{aligned} \quad (4\text{-}25)$$

If the angle $\langle\Psi\rangle$ is not close to zero (actually Ψ is close to 90^o for low elevation angles) and angle distribution is not large (less than 30^o), the orientation distribution is assumed to be 2-D Gaussian shape and the pdf is,

$$p(\Psi,\beta) = \frac{1}{2\pi\sigma\sigma_\beta}\exp\left[-\frac{(\Psi - \langle\Psi\rangle)^2}{2\sigma^2} - \frac{(\beta - \langle\beta\rangle)^2}{2\sigma_\beta^2}\right] \quad (4\text{-}26)$$

where $\sigma_\beta = \sigma / \sin\langle\Psi\rangle$. Those angle moments can be expressed as,

$$\langle\sin^2\beta\rangle = \frac{1}{2}(1 - r_\beta \cos 2\langle\beta\rangle) \tag{4-27a}$$

$$\langle\sin^4\beta\rangle = \frac{3}{8} - \frac{1}{2} r_\beta \cos 2\langle\beta\rangle + \frac{1}{8} r_\beta^4 \cos 4\langle\beta\rangle \tag{4-28a}$$

$$\langle\sin^2\Psi\rangle = \frac{1}{2}(1 - r \cos 2\langle\Psi\rangle) \tag{4-29a}$$

$$\langle\sin^4\Psi\rangle = \frac{3}{8} - \frac{1}{2} r \cos 2\langle\Psi\rangle + \frac{1}{8} r^4 \cos 4\langle\Psi\rangle \tag{4-30a}$$

$$\vdots$$

where $r = \exp(-2\sigma^2)$ and $r_\beta = \exp(-2\sigma_\beta^2)$. Using ensemble form of Rayleigh scattering and angle moments shown above, Ryzhkov was able to calculate the mean canting angle as,

$$\begin{aligned} |\langle\beta\rangle| &\approx \frac{2|\langle S_{hh}^* S_{hv}\rangle_n|}{\langle|S_{hh}|^2\rangle_n - \langle|S_{vv}|^2\rangle_n} \\ &= \frac{2|\rho_{xh}|(ldr)^{1/2}}{1 - \xi_{dr}^{-1}} \end{aligned} \tag{4-31}$$

where "n" in subscript denotes normalization by a factor of $\langle|f_b|^2\rangle$, and ρ_{xh} is the co-cross correlation function for a horizontal incident wave.

Based on (4-31), a more accurate formula can be obtained through simulations. In these simulations, the mean axis ratio model suggested by Pruppacher-Pitter (1971)[41], dsd model suggested by Ulbrich (1983)[54], fixed mean canting angle, $\langle\Psi\rangle$ between 84^o to 96^o, and σ between 0^o and 30^o were used. The more accurate formula is,

$$|\langle\beta\rangle| = 1.87 \frac{|\rho_{xh}|(ldr)^{1/2}}{1 - \xi_{dr}^{-1}} \tag{4-32}$$

Using this equation, Ryzhkov stated that this mean canting angle estimator is almost unbiased with standard deviation around 6% when mean canting angles are within 0^o to 6^o.

Using the same approach, Ryzhkov also found that he could estimate σ_β without using $|\rho_{xh}|$. The ratio of $(ldr^{1/2})/(1-\xi_{dr}^{-1})$ is only determined by r_β, if $|\langle\beta\rangle| \ll \sigma_\beta$. Based on the same simulations, the ratio is,

$$\frac{ldr}{(1-\xi_{dr}^{-1})} = 0.05\frac{1-r_\beta^4}{r_\beta^2} \tag{4-33}$$

This standard deviation of canting angle estimator is also unbiased when $\sigma_\beta > 8^o$.

4.2.3 Asymmetric Ratio Method

In this section we will propose a new algorithm to estimate standard deviation of canting angle based on asymmetric ratio (A_{sy}) with the assumption that the mean canting angle is zero. The A_{sy} was proposed by Kwiatkowski et al. (1995)[31] and was defined as the ratio of two eigenvalues of the Graves power matrix ($\mathbf{G}$). When the symmetry axis of an oblate drop is aligned along the horizontal or vertical axis of the polarization plane, the back scattering matrix ($\mathbf{S}^o$) is,

$$\mathbf{S}^o = \begin{bmatrix} S_{hh}^o & 0 \\ 0 & S_{vv}^o \end{bmatrix} \tag{4-34}$$

The Graves power matrix is defined as,

$$\begin{aligned} \mathbf{G}^o &= \mathbf{S}^{o*}\mathbf{S}^o \\ &= \begin{bmatrix} |S_{hh}^o|^2 & 0 \\ 0 & |S_{vv}^o|^2 \end{bmatrix} \end{aligned} \tag{4-35}$$

If the drop has canting angle β, the back scattering matrix becomes to,

$$\mathbf{S} = \mathbf{R}^{-1}\mathbf{S}^o\mathbf{R} \tag{4-36}$$

where $\mathbf{R}$ is rotation operator defined as,

$$\mathbf{R} = \begin{bmatrix} \cos\beta & -\sin\beta \\ \sin\beta & \cos\beta \end{bmatrix} \tag{4-37}$$

and then the Graves power matrix is,

$$\mathbf{G} = \mathbf{S}^*\mathbf{S} = \mathbf{R}^{-1}\mathbf{S}^{o*}\mathbf{S}^o\mathbf{R} = \mathbf{R}^{-1}\mathbf{G}^o\mathbf{R} \tag{4-38}$$

Obviously, the diagonal terms of $\mathbf{G}^o$ are the two eigenvalues of $\mathbf{G}$. Therefore, the asymmetric ratio can be expressed as,

$$a_{sy} = \frac{|S^o_{hh}|^2}{|S^o_{vv}|^2} \tag{4-39a}$$

$$A_{sy} = 10\log(a_{sy}) \tag{4-39b}$$

Comparing (4-39a,b) with the definition of Z_{dr}, the asymmetric ratio is Z_{dr} in the absence of canting angle. Following Kwiatkowski et al., Huang (1997)[23] has shown that the asymmetric ratio can be calculated from the power matrix which is,

$$\mathbf{P} = \begin{bmatrix} 1 & b^2 \\ b^2 & a^2 \end{bmatrix} = \begin{bmatrix} 1 & ldr \\ ldr & \xi_{dr}^{-1} \end{bmatrix} \tag{4-40}$$

The two eigenvalues of the Graves power matrix is,

$$\lambda = \frac{(1+2b^2+a^2)}{2} \pm \frac{\sqrt{(1+2b^2+a^2)^2 - 4[a^2+b^2+a^2b^2+b^4-b^2(1+a)^2]}}{2}. \tag{4-41}$$

Moreover, Huang (1997)[23] also showed that one can roughly estimate the standard deviation of canting angle by comparing $A_{sy} - Z_{dr}$ with LDR.

Since asymmetric ratio (A_{sy}) is the version of Z_{dr} without canting angle, the relation between these two parameters should contain useful canting angle information. We start with (4-36) and do the matrix multiplication. The diagonal

terms of the back scattering matrix of an oblate drop with canting angle β can be expressed as,

$$S_{hh} = S^o_{hh}\cos^2\beta + S^o_{vv}\sin^2\beta \tag{4-42a}$$

$$S_{vv} = S^o_{hh}\sin^2\beta + S^o_{vv}\cos^2\beta \tag{4-42b}$$

Because the shapes and orientations are independent, the differential reflectivity factor ($\xi_{dr} = 10^{0.1Z_{dr}}$) for an ensemble case is,

$$\begin{aligned}\xi_{dr} &= \frac{|S_{hh}|^2}{|S_{vv}|^2} \\ &= \frac{1 + \frac{\langle|S^o_{vv}|^2\rangle}{\langle|S^o_{hh}|^2\rangle}\frac{\langle\sin^4\beta\rangle}{\langle\cos^4\beta\rangle} + 2Re\left[\frac{\langle S^o_{hh}S^{o*}_{vv}\rangle}{\langle|S^o_{hh}|^2\rangle}\right]\frac{\langle\cos^2\beta\sin^2\beta\rangle}{\langle\cos^4\beta\rangle}}{\frac{\langle\sin^4\beta\rangle}{\langle\cos^4\beta\rangle} + \frac{\langle|S^o_{vv}|^2\rangle}{\langle|S^o_{hh}|^2\rangle} + 2Re\left[\frac{\langle S^o_{hh}S^{o*}_{vv}\rangle}{\langle|S^o_{hh}|^2\rangle}\right]\frac{\langle\cos^2\beta\sin^2\beta\rangle}{\langle cos^4\beta\rangle}}\end{aligned} \tag{4-43}$$

This equation includes two angle moment operators. The first one is,

$$\begin{aligned}\frac{\langle\sin^4\beta\rangle}{\langle\cos^4\beta\rangle} &= \frac{\langle(1-\cos^2\beta)^2\rangle}{\langle\cos^4\beta\rangle} \\ &= \frac{1}{\langle\cos^4\beta\rangle} - 2\frac{\langle\cos^2\beta\rangle}{\langle cos^4\beta\rangle} + 1\end{aligned} \tag{4-44}$$

If β is narrow Gaussian distribution with zero mean, $\langle\cos^4\beta\rangle$ should be close to one. The (4-44) becomes,

$$\begin{aligned}\frac{\langle\sin^4\beta\rangle}{\langle\cos^4\beta\rangle} &\approx -2(\frac{\langle\cos^2\beta\rangle}{\langle\cos^4\beta\rangle} - 1) \\ &= -2x\end{aligned} \tag{4-45}$$

The second angle moment operator is,

$$\begin{aligned}\frac{\langle \cos^2\beta \sin^2\beta \rangle}{\langle \cos^4\beta \rangle} &= \frac{\langle \cos^2\beta(1-\cos^2\beta) \rangle}{\langle \cos^4\beta \rangle} \\ &= \frac{\langle \cos^2\beta \rangle}{\langle \cos^4\beta \rangle} - 1 \\ &= x \end{aligned} \tag{4-46}$$

Finally, $\langle S^o_{hh} S^{o*}_{vv} \rangle / \langle |S^o_{hh}|^2 \rangle$ should be close to R_{co} for a zero mean canting angle distribution. The R_{co} is co-co correlation and is normalized by $|S_{hh}|^2$. Combining with two angle moment operators, (4-43) is simplified as,

$$\xi_{dr} = \frac{1 - 2x(a_{sy})^{-1} + 2x(Re[R_{co}])}{-2x + (a_{sy})^{-1} + 2x(Re[R_{co}])} \tag{4-47}$$

We can calculate x easily as,

$$x = \frac{1 - \xi_{dr}(a_{sy})^{-1}}{2(-\xi_{dr} + Re[R_{co}]\xi_{dr} + (a_{sy})^{-1} - Re[R_{co}])} \tag{4-48}$$

The angle moment operator, x, can be expressed in terms of σ_β and mean canting angle as (Ryzhkov, 2001)[42],

$$\begin{aligned} x+1 &= \frac{\langle \cos^2\beta \rangle}{\langle \cos^4\beta \rangle} \\ &= \frac{\frac{1}{2}(1 + r\cos 2\langle\beta\rangle)}{\frac{3}{8} + \frac{1}{2}r\cos 2\langle\beta\rangle + \frac{1}{8}r^4 \cos 4\langle\beta\rangle} \end{aligned} \tag{4-49}$$

where $r = exp(-2\sigma^2_\beta)$. Since β is assumed to be zero mean, $\langle\beta\rangle$ is equal to one. We can solve (4-49) and get r. The σ_β estimator is,

$$\sigma_\beta = \sqrt{\frac{log(r)}{-2}} \tag{4-50}$$

4.3 Stability of Three Canting Angle Estimators

In this section we simulate the linear dual-polarization radar observables such as reflectivity factor (Z_h), differential reflectivity (Z_{dr}), linear depolarization ratio (LDR), asymmetric ratio (A_{sy}), and so on. These simulations are done using "cantmat"[1] which was written by Dr. Chengxian Tang at the Radar and Communication Group (RCG), Department of Electrical Engineering, Colorado State University (1996). Unless otherwise specified, the following conditions are applied in the simulations:

1. Operating frequency is 2.725 GHz.

2. Rain drop temperature is 20^o C.

3. A gamma raindrop size distribution was assumed and three parameters of dsd,(N_w,D_o,μ), were derived from Joss disdrometer measurements at Darwin, Australia for the whole wet season of 1999.

4. Mean axis ratio model as suggested by Andsager et al. (1990)[1] is used for $1 \leq D \leq 4$ mm and by Beard and Chuang (1987)[7] for $D < 1$ and $D > 4$ mm.

5. The polar orientation angle distribution, $p_\Omega(\theta_b)$, is assumed to be Gaussian shape with zero mean. The azimuthal angle, ϕ_b, is assumed to be a uniform distribution in (0,2π).

6. Size integration is from $D_{min} = 0$ mm to $D_{max} = 2.5D_o$.

7. Orientation angle integration interval is (0^o,90^o) for θ_b and (0^o,360^o) for ϕ_b.

---

[1]See http://www.radar.colostate.edu/scattering

Algorithm		$\sigma_\beta = 5^o$	$\sigma_\beta = 10^o$	$\sigma_\beta = 15^o$	$\sigma_\beta = 20^o$
ρ_4	$\sigma_{\bar{\sigma}_\beta}$	0.002^o	0.001^o	0.001^o	0.001^o
	$\bar{\sigma}_\beta$	4.85^o	10.40^o	15.14^o	20.28^o
Ryzhkov	$\sigma_{\bar{\sigma}_\beta}$	0.079^o	0.149^o	0.192^o	0.207^o
	$\bar{\sigma}_\beta$	4.59^o	9.48^o	14.30^o	19.28^o
Asymmetric Ratio	$\sigma_{\bar{\sigma}_\beta}$	0.103^o	0.115^o	0.122^o	0.111^o
	$\bar{\sigma}_\beta$	5.35^o	10.43^o	14.49^o	17.80^o

Table 4.1: Fluctuation of estimated σ_β due to drop size distribution variations.

After calculating the radar observables, we can estimate the standard deviation of canting angle ($\hat{\sigma}_\beta$) by using the three algorithms which were discussed in the previous section, and compare them with σ_{θ_b} which we set in the simulation program ($\sigma_{\theta_b} = \sigma_\beta$, see Section 4.1.1).

4.3.1 $\bar{\sigma}_\beta$ Fluctuation due to Precipitation Models

a. Drop Size Distribution

In order to study the affect of drop size distribution on the canting angle estimators, we use 2159 measured dsd data to simulate radar observables and to estimate σ_β. The orientation angle distribution ($p_\Omega(\theta_b)$) was assumed to be of Gaussian shape with $\sigma_{\theta_b} = 5^o$, 10^o, 15^o and 20^o for θ_b, and uniform distribution for ϕ_b. Table 4.1 shows the results. From the results we found that the three algorithms were negligibly affected by the drop size distribution variation (the maximum standard deviation of $\bar{\sigma}_\beta$ is 0.207^o for Ryzhkov formula). The ρ_4 algorithm is the most stable and almost unbiased (0.8% overestimate on average). The Ryzhkov formula underestimates by 5.4% on average. We suspect that the underestimate is because his formula is based on Rayleigh scattering whereas our simulations are mainly based on the T-matrix method. The asymmetric ratio algorithm is also unbiased (0.8% underestimate on average). However, this algorithm tends to overestimate $\bar{\sigma}_\beta$ for $\sigma_\beta = 5^o$ and 10^o, and underestimate it for 15^o and

20^o. In conclusion, the three algorithms are accurate and stable with respect to variability in the drop size distribution.

b. Axis Ratio

The other important feature of the precipitation model is the mean axis ratio versus D relation. Here we used the linear Pruppacher-Pitter model (1971)[41]. The original model fixed the slope at 0.062 mm^{-1} (see 2-20). We change the slope systematically from 0.032 to 0.092 to account for drop oscillations. The distribution of θ_b ($p_\Omega(\theta_b)$) is assumed to be Gaussian in shape with zero mean and σ_β equal to 10^o. Fig. 4.10 shows $\bar{\sigma}_\beta$ versus the slope of axis ratio versus D; Fig. 4.11 shows the standard deviation of estimated σ_β versus slope. The ρ_4 is almost not affected by the mean axis ratio. The Ryzhkov formula underestimates by 0.6-1^o as expected. If we ignore the extreme slope value (0.032 mm^{-1}), this algorithm is very stable ($\sigma_{\bar{\sigma}_\beta}$ is less than 0.4^o). The asymmetric ratio algorithm overestimates when the slope is less than 0.052 mm^{-1} and underestimates when the slope is larger. On average, it is nearly unbiased. Also, the asymmetric ratio algorithm is very stable because $\sigma_{\bar{\sigma}_\beta}$ is less than 0.3^o if we ignore the extreme values of the slope.

4.3.2 $\bar{\sigma}_\beta$ Fluctuation due to Measurement Error

Since we use radar measurements to estimate the standard deviation of canting angle, we have to evaluate the impact of measurement error on the algorithms. First, we simulate radar observables by setting $N_o = 8000$, $D_0 = 2\ mm$ and $\mu = 0$ (exponential dsd). The distribution of orientation angle, $p_\Omega(\theta_b)$, is Gaussian with zero mean and $\sigma_{\theta_b} = \sigma_\beta = 10^o$. The simulation gives the mean radar values as follows:

1. $Z_h = 55.52;\ dBZ.$

2. $Z_{dr} = 2.22;\ dB.$

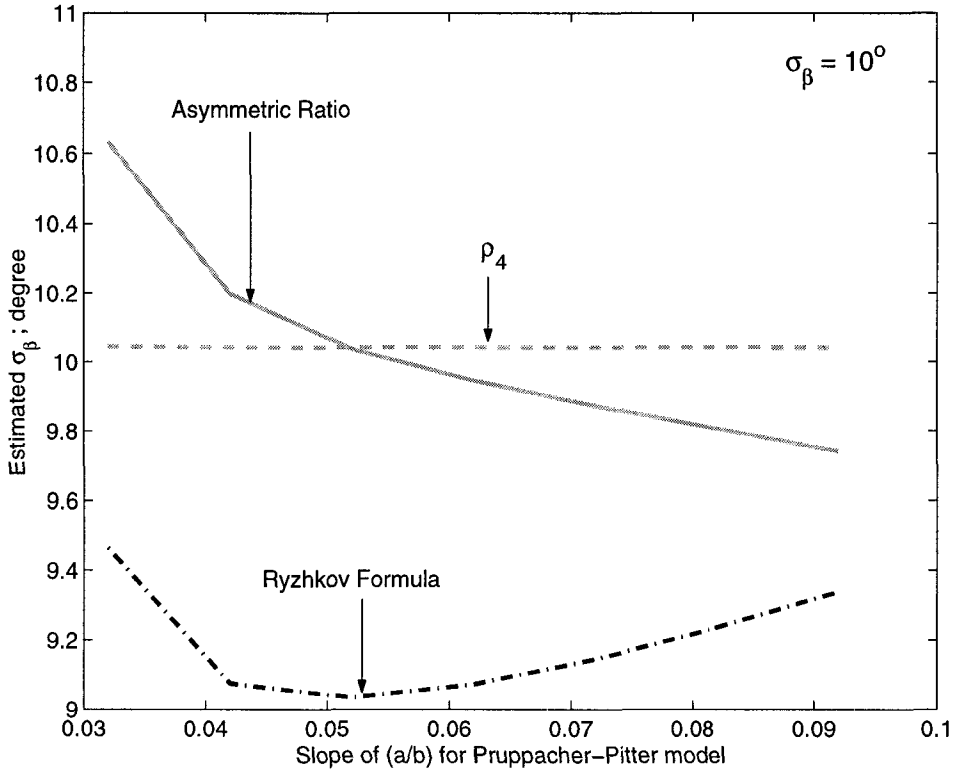

Figure 4.10: Mean of estimated σ_β versus different axis ratio models. The axis ratio model is suggested by Pruppacher-Pitter (1971)[41]. The original model fixed the slope of b/a versus D_{eq} at 0.062 mm^{-1}. Here we changed slopes from 0.032 to 0.092 mm^{-1}.

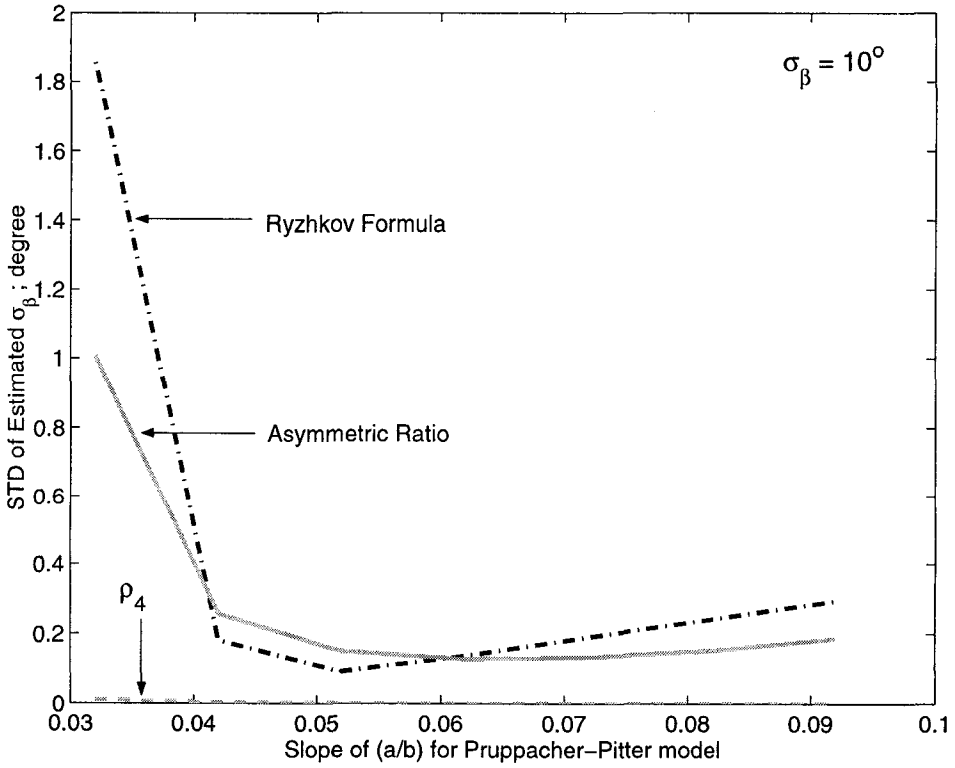

Figure 4.11: As in Fig 4.10 except for standard deviation of estimated σ_β.

3. $A_{sy} = 2.39$; dB.

4. $LDR = -27.16$; dB.

5. $\rho_{hv} = 0.992$. Note that ρ_{hv} is normalized by $\sqrt{|S_{hh}|^2|S_{vv}|^2}$ and R_{co} in the covariance matrix is normalized by $|S_{hh}|^2$.

The corresponding covariance matrix is,

$$\Sigma = \begin{bmatrix} 1 & 5.5682 \cdot 10^{-11} e^{j0.0089} & 0.7683 e^{-j0.0013} \\ - & 0.0038 & 2.5896 \cdot 10^{-10} e^{j3.1398} \\ - & - & 0.5996 \end{bmatrix} \tag{4-51}$$

Using the simulated radar values and covariance matrix, we calculate the mean σ_β by the three algorithms. The results are 10.04^o for ρ_4 algorithm, 9.91^o for Ryzhkov formula and 9.97^o for asymmetric ratio algorithm (note that the assumed value was 10^o).

Next, we simulate random errors for Z_{dr}, LDR, $|R_{co}|$ and δ_{co}. Note that A_{sy} is calculate from Z_{dr} and LDR. All random error sets are assumed to be independent and Gaussian shape with zero mean. The standard deviation of random errors for Z_{dr} is 0.2 dB, for LDR is 1.4 dB, for amplitude of R_{co} is 0.005 and for phase of R_{co} (δ_{co}) is 3^o. Applying these errors to the simulated radar values and the covariance matrix, we estimate σ_β using the three algorithms and obtain the standard deviation of estimated σ_β, mean of estimated σ_β and average error (by compare with estimated σ_β without random error). In order to get reliable results, we repeat the procedure 50 times and do the average.

Fig. 4.12 shows the PDF of estimated σ_β for a single simulation and Table 4.2 shows the average results based on 50 simulations. The Ryzhkov formula and asymmetric ratio algorithm are nearly insensitive to measurement errors (1.66% for Ryzhkov formula and 0.78% for the asymmetric ratio algorithm). We expect that the asymmetric ratio algorithm has the least error because the correlation

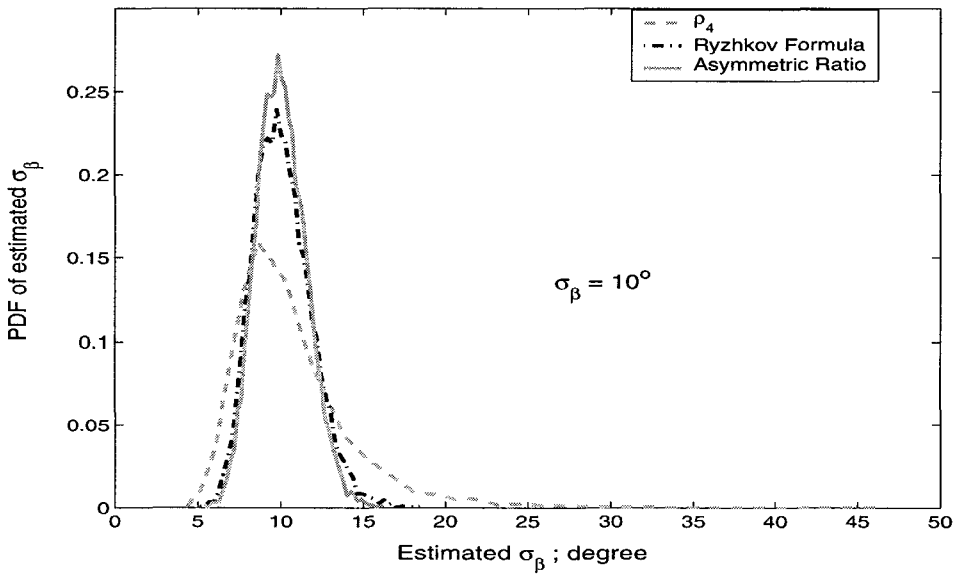

Figure 4.12: The PDF of estimated σ_β. This is a result from one of 50 simulations.

	Mean of $\sigma_{\bar{\sigma}_\beta}$	Mean of $\bar{\sigma}_\beta$	Error
ρ_4	4.01^o	10.82^o	7.70%
Ryzhkov	1.77^o	10.08^o	1.66%
Asymmetric ratio	1.52^o	10.04^o	0.78%

Table 4.2: Fluctuation of estimated σ_β due to measurement errors. The results are averaged over 50 individual simulations.

	σ_β by (4-4)	estimated σ_β by ρ_4	estimated σ_β by Ryzhkov formula	estimated σ_β by Asymmetric Ratio
$\theta_{b0} = 3^o$	2.90^o	3.35^o(15.52%)	3.17^o(9.31%)	3.75^o (29.10%)
$\theta_{b0} = 10^o$	7.17^o	7.33^o(2.23%)	6.93^o(−3.35%)	7.90^o (10.18%)
$\theta_{b0} = 15^o$	10.71^o	11.89^o (11.02%)	11.13^o (3.92%)	11.92^o (11.30%)

Table 4.3: The σ_β for the Holt distribution (1984)[22] compared with the three σ_β estimators.

between Z_{dr} and A_{sy} is higher. The ρ_4 algorithm has the most error (around 7.7%). Generally, the three algorithms can be considered to be stable with respect to radar measurement errors.

4.3.3 $\bar{\sigma}_\beta$ Fluctuation due to Orientation Distribution

In the previous section, we evaluated the performance of the canting angle algorithms by assuming that the canting angle distribution is Gaussian in shape. However, the canting angle distribution may not be Gaussian. Therefore, we need to examine if these algorithms still hold for non-Gaussian distributions. First, we set orientation angle (θ_b) to be Holt's distribution (Holt 1984)[22] with $A = 1000$ and $\theta_{b0} = 3^o$, 10^o and 15^o. The distribution of ϕ_b is assumed to be uniform. Using (4-4), we can get the distributions of canting angle (β) which are rectangular (for $\theta_{b0} = 3^o$) and bi-modal (for $\theta_{b0} = 10^o$ and 15^o). The normalized histograms (PMF) and corresponding σ_βs are shown in Fig. 4.9 (for $\theta_{b0} = 3^o$ and 10^o). We then use the Holt distribution to calculate the radar observables and using these values we can estimate σ_β.

Table 4.3 shows the simulation results for σ_β. We found that all three algorithms can be used to estimate σ_β for non-Gaussian distributions. The Ryzhkov formula is the better one (9.31% overestimate at $\theta_{b0} = 3^o$ is the worst case) and the Asymmetric ratio algorithm is the worst one (29.10% overestimate at $\theta_{b0} = 3^o$).

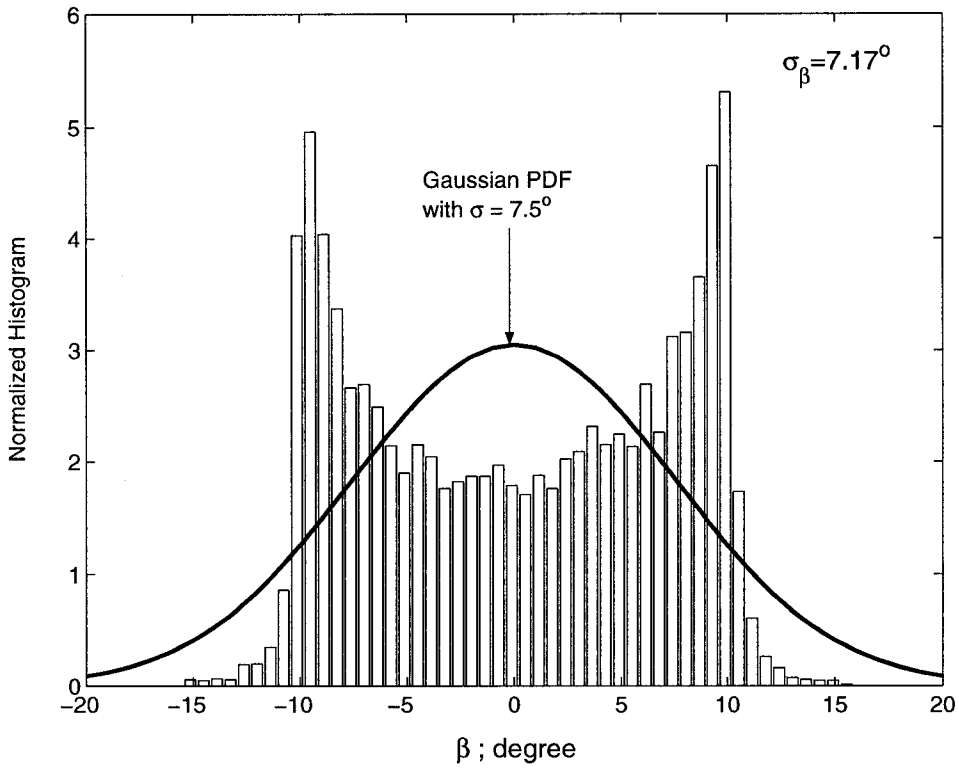

Figure 4.13: The normalized histogram (PMF) of canting angle (β) compared with Gaussian PDF with same σ_β. The orientation (θ_b) is the Holt distribution with $A = 1000$ and $\theta_{b0} = 10^o$.

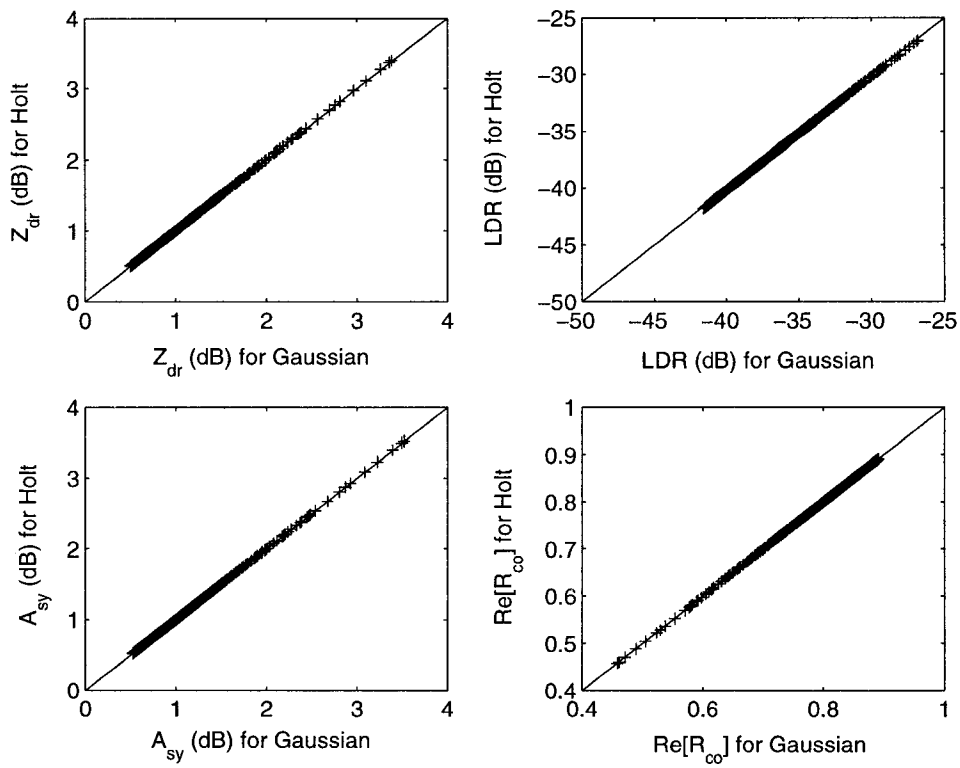

Figure 4.14: Z_{dr}, LDR, A_{sy} and $Re[R_{co}]$ for Holt and Gaussian orientation angle (θ_b) distributions. Z_{dr}, A_{sy} and $Re[R_{co}]$ are almost the same for these two distributions. The LDR is little higher for Gaussian orientation distribution.

Fig. 4.13 shows the normalized histogram (PMF) of β compared with a Gaussian PDF with $\sigma \approx \sigma_\beta$. The bi-modal distribution has higher probability at around $\pm 10^o$. Such canting would give higher (lower) vertical (horizontal) returned power compared with the Gaussian distribution. However, the probabilities of the bi-modal distribution drops fast for $\beta > 10^o$ and $\beta < -10^o$. In these regions, the Gaussian canting should have higher (lower) vertical (horizontal) power. Fig. 4.14 compares Z_{dr}, LDR, A_{sy} and $Re[R_{co}]$ for the two distributions. As we expect, Z_{dr}, A_{sy}, $Re[R_{co}]$ and LDR are almost the same for the two distributions. The co-cross correlations are too small because the mean canting angle is close to zero and because of "mirror" reflection symmetry. Our simulations show that it is possible to estimate the width of the canting angle distribution from radar measurements, and that it is generally unaffected by dsd variations, the mean shape or the precise form of the canting angle distribution.

4.4 Case Study

4.4.1 Case of July 28, 1997, Colorado

On the evening of July 28, 1997 (MDT; 29 July UTC), a flash-flood producing storm developed near Fort Collins, Colorado. Rain started to fall steadily west of Fort Collins from 1800 MDT (0000 UTC) to 2200 MDT (0400 UTC). The most intense rainfall was at 2100 MDT (0300 UTC) to 2200 (0400 UTC). During that time, the CSU-CHILL radar scans were mainly focused on the Duke gage network which is located southeast of the radar. Fortunately, the CSU-CHILL radar did 3 surveillance scans at 2130, 2145 and 2200 MDT. Therefore, we still have enough data to analyze the Fort Collins flood case.

Fig. 4.15 shows a PPI scan at 2145 MDT (0345 UTC). From the Z_h data, we can identify three major storm cells. The first one located at azimuth angle between 278^o and 295^o and range between 38 km and 50 km (western Fort Collins)

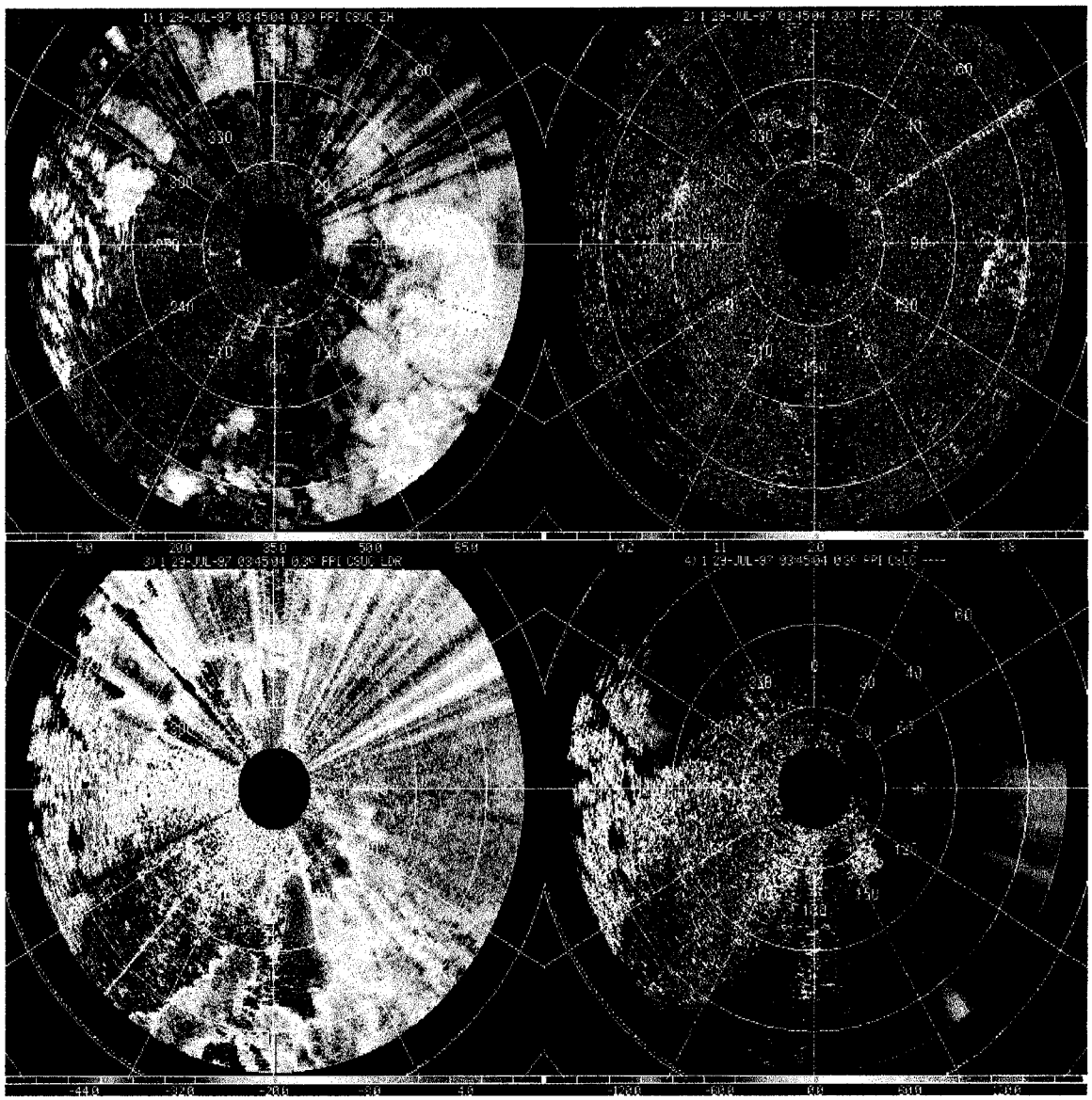

Figure 4.15: A 360°-PPI scan of CSU-CHILL radar at 21:45, July 28, 1997. The upper-left panel is Z_h (in dBZ), upper-right panel is Z_{dr} (in dB), lower-left panel is LDR (in dB) and lower-right panel is ϕ_{dp} (in degrees).

caused the destructive flash flood. In the following analysis, we refer to this as the "flood case". The second storm cell was located at azimuth angle between 98^o and 110^o, and range between 35 km and 60 km. This area covers the Duke gage network and will be referred to as the "Duke case". Also, from lower-right panel (ϕ_{dp}), there was no significant increase of ϕ_{dp} through the rain cell so we did not perform any attenuation-correction. However, we did do the Z_{dr} and LDR calibration using the sun-calibration data.

a. Flood Case

In this case, we used three 360^o-PPI scan data at 21:30, 21:45 and 22:00 MDT. In order to insure the data quality, we applied the following thresholds:

1. $Z_h \geq 35$; dBZ.
2. $Z_{dr} \geq 0.5$; dB.
3. $SNR \geq 40$; dB.
4. $K_{dp} \geq 0.1^o$.
5. $\rho_{hv} \geq 0.9$.

There were 5830 qualified data sets (individual range resolution volumes) in this case. Fig. 4.16 shows the histograms of estimated σ_β by using the simplified ρ_4 algorithm and the Ryzhkov algorithm. The distribution of σ_β using the ρ_4 algorithm is broader than the Ryzhkov algorithm. It agrees with the simulation results (see Fig. 4.12) because the ρ_4 method is more affected by measurement errors. The difference between two modal values is around 2.3^o. This could be due to **(a)** dsd variations where the Ryzhkov algorithm tends to slightly underestimate σ_β as compared with the ρ_4 algorithm (see Table 4.1 and using linear interpolation), and **(b)** mean axis ratio variations where the Ryzhkov algorithm also slightly underestimates the ρ_4 algorithm (see Fig. 4.10 and Fig. 4.11). Combining the dsd

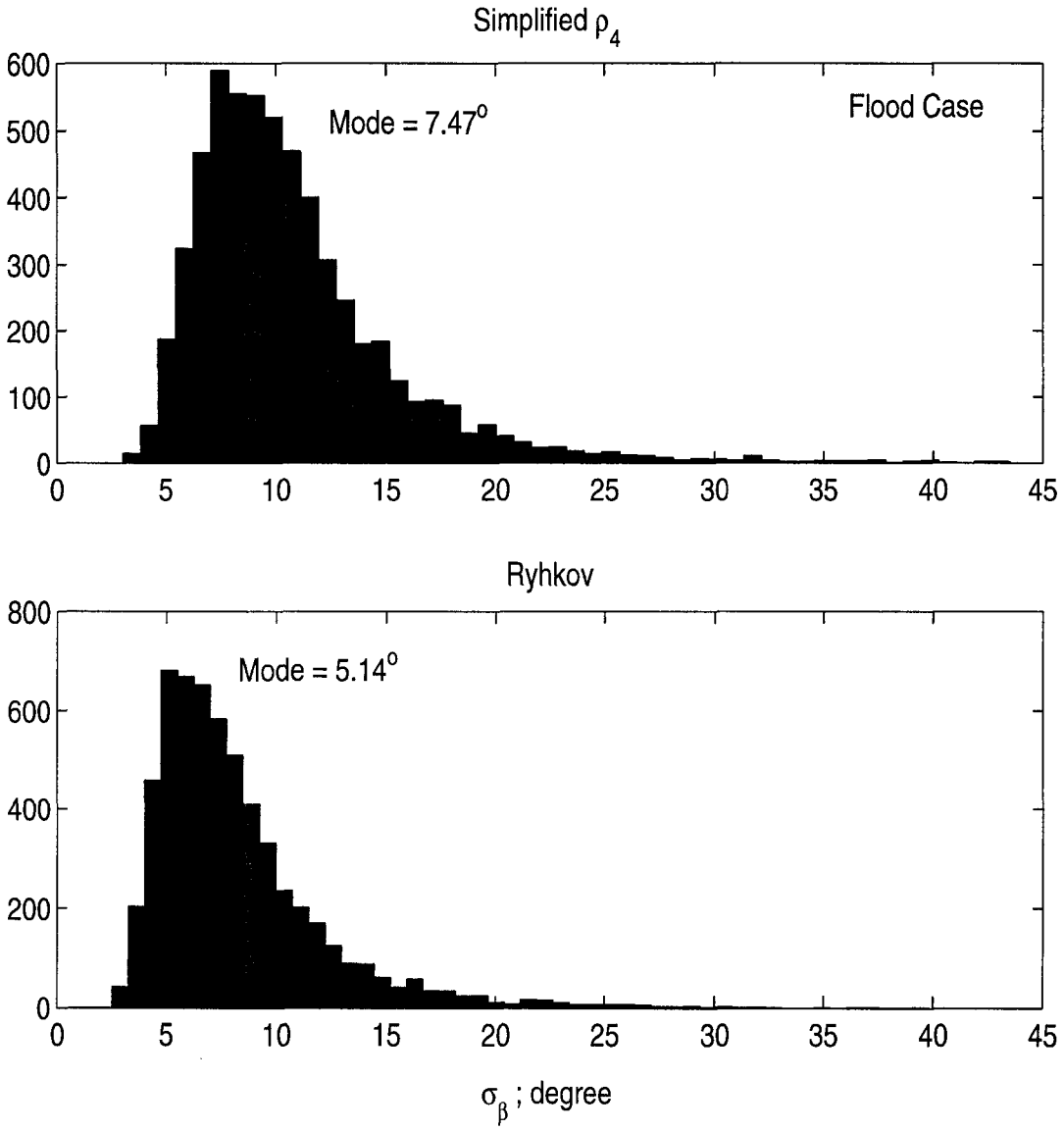

Figure 4.16: Histogram of estimated σ_β for the Flood case. The upper panel is for the simplified ρ_4 algorithm which has modal value at 7.47°, and the lower panel is for the Ryzhkov algorithm which has modal value of 5.14°.

and mean axis ratio effects, the Ryzhkov algorithm should underestimate σ_β by $1.3^o \pm 0.3^o$ at $\sigma_\beta = 7.5^o$ compared with the ρ_4 algorithm.

The upper panel of Fig. 4.17 shows the scatter plot of estimated σ_β versus Z_{dr}. We found that σ_β decreases when Z_{dr} increases. This tendency may reflect the fact that larger drops are more stably oriented as compared to small-sized drops (i.e., more "resistant" to transverse mode drop oscillations, for example). Both the ρ_4 and Ryzhkov algorithms show this same tendency. For further analysis, we divide Z_{dr} into several equal intervals from 0.5 dB to upper the bound of Z_{dr} (each interval is 0.5 dB). If the number of data points in each interval are more than 10, we compute the mean and standard deviation of σ_β. The lower panel of Fig. 4.17 shows the results. The mean σ_β from the Ryzhkov algorithm is systematically 3^o lower than the simplified ρ_4 algorithm for $0.5 < Z_{dr} \leq 1$ dB, and gets closer when Z_{dr} increases (less than 1^o for $4 < Z_{dr} \leq 4.5$ dB). These data also show that, on average, the larger-sized drops are more stably oriented than the smaller ones.

b. Duke Case

The CSU-CHILL radar scanned the Duke gage network area continuously from 21:31 to 21:32 MDT; our focus is on the area whose azimuth angle is from 98^o to 110^o, elevation angle is from 0^o to 2^o, and range is from 35 km to 60 km. After applying the data quality thresholds, there were 14807 data points available (each data point corresponds to data from an individual range resolution volume). Fig. 4.18 shows the histograms of estimated σ_β. As expected, the distribution of estimated σ_β using the simplified ρ_4 algorithm is broader than the Ryzhkov algorithm because of measurement fluctuations. The modal value of estimated σ_β is 8.11^o using the simplified ρ_4 algorithm and 6.16^o by using the Ryzhkov algorithm. Both mode numbers are higher than in the "flood case", but the difference between them is smaller.

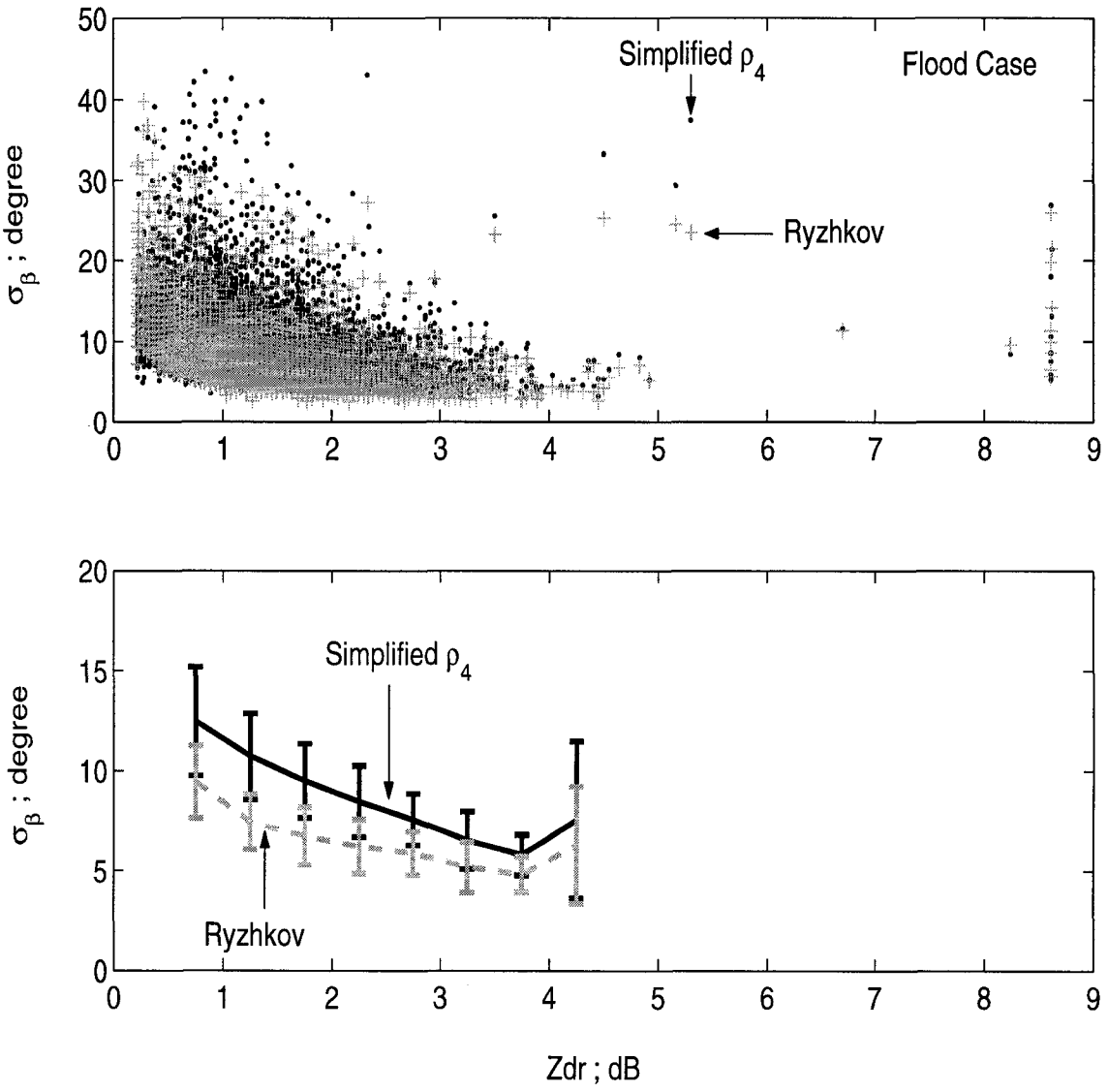

Figure 4.17: Estimated σ_β versus Z_{dr}. The upper panel is a scatter plot (5830 data points). In the second panel, we divide Z_{dr} into 8 equal intervals, each interval being 0.5 dB. We calculate the mean and standard deviation of corresponding σ_β in each interval. The error bar is one standard deviation.

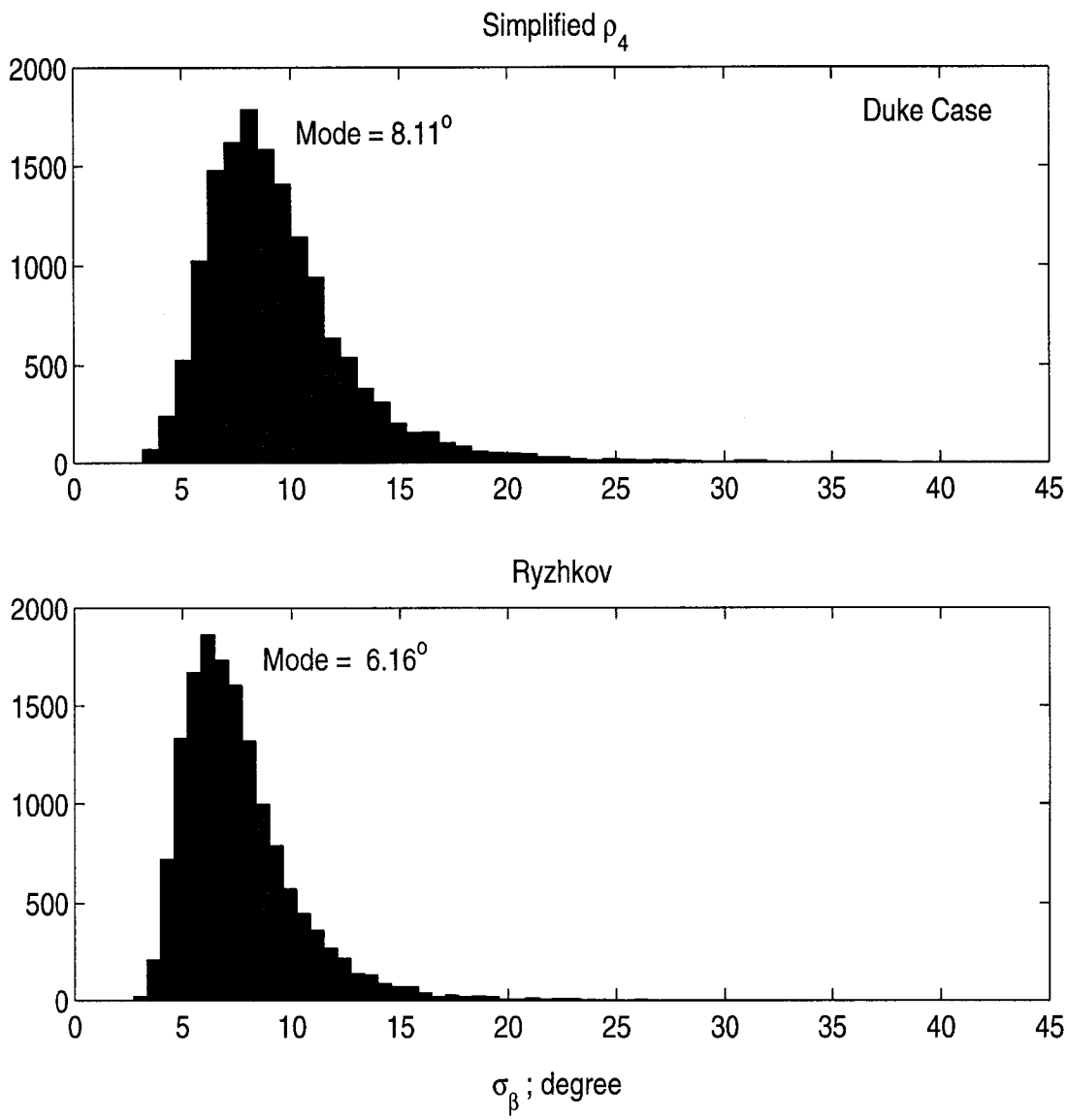

Figure 4.18: Same as Fig. 4.16 except from the Duke case (14,807 data points).

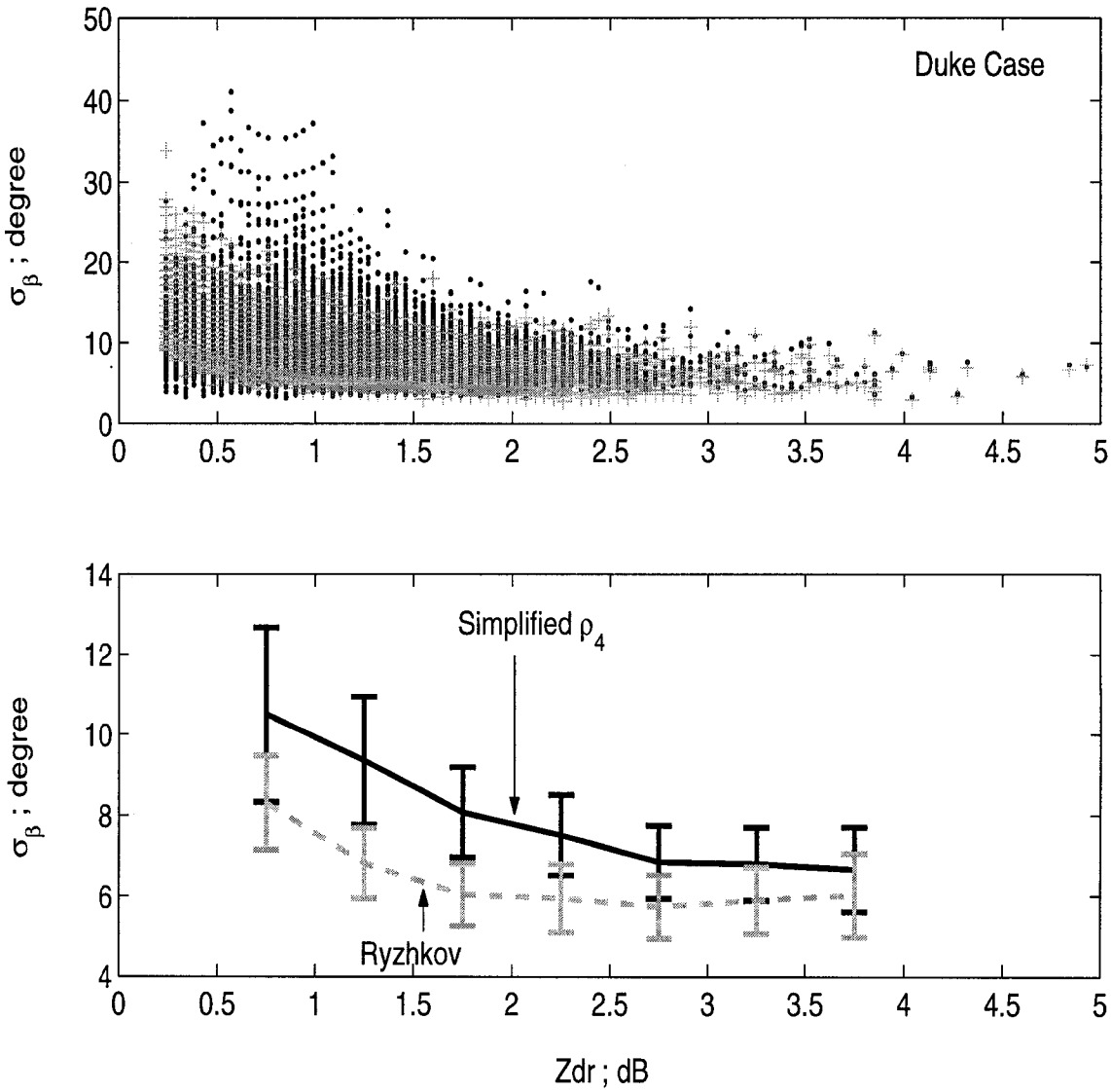

Figure 4.19: Same as Fig. 4.17 except from the Duke case.

The upper panel of Fig. 4.19 shows the scatter plot of estimated σ_β versus Z_{dr}. The dark dots represent the ρ_4 algorithm and grey crosses represent the Ryzhkov algorithm. Both algorithms show that σ_β decreases as Z_{dr} increases. The lower panel of Fig. 4.19 shows the mean and standard deviation of estimated σ_β versus Z_{dr}. The tendency is much clearer in this plot. The Ryzhkov algorithm is 2.2^o lower than the simplified ρ_4 for $0.5 < Z_{dr} \leq 1\ dB$, and is 0.64^o lower for $3.5 < Z_{dr} \leq 4$ dB. Once again, we find that the two algorithms have larger differences at low Z_{dr} values, and are roughly in agreement at high Z_{dr} values.

4.4.2 June 11, 2000, Colorado (STEPS) Case

From 22 May to 16 July 2000, a field campaign named Severe Thunderstorm Electrification and Precipitation Study (STEPS) was held near the border area between Colorado and Kansas. This field campaign involved three weather radars, CSU-CHILL radar from the Colorado State University, S-Pol radar from the National Center for Atmospheric Research and WSR-88D Doppler radar of the National Weather Service. Fig. 4.20 shows the locations of the three radars. The CSU-CHILL radar was located at 39^o $14.0763'$ north and 102^o $16.6745'$ west.

On the late evening of June 11, an intense rain-producing storm approached from the west of the CSU-CHILL radar and passed through to its east. Fig. 4.21 shows a PPI scan of Z_h. We can easily identify a high Z_h area (azimuth angle from 260^o to 355^o and range from 30 km to 60 km). The CSU-CHILL radar measured the 3x3 covariance matrix in each resolution volume. After carefully calibrating the covariance matrix and correcting for system offsets (the calibration and correction were done by Dr. John Hubbert), we were able to calculate Z_{dr}, LDR and ρ_{hv} from the covariance matrix and estimated σ_β by using the simplified ρ_4 algorithm and the Ryzhkov algorithm.

Fig. 4.22 shows the histogram of estimated σ_β using the two algorithms. Unlike the "Flood case" and the "Duke case", the differences between two modal values

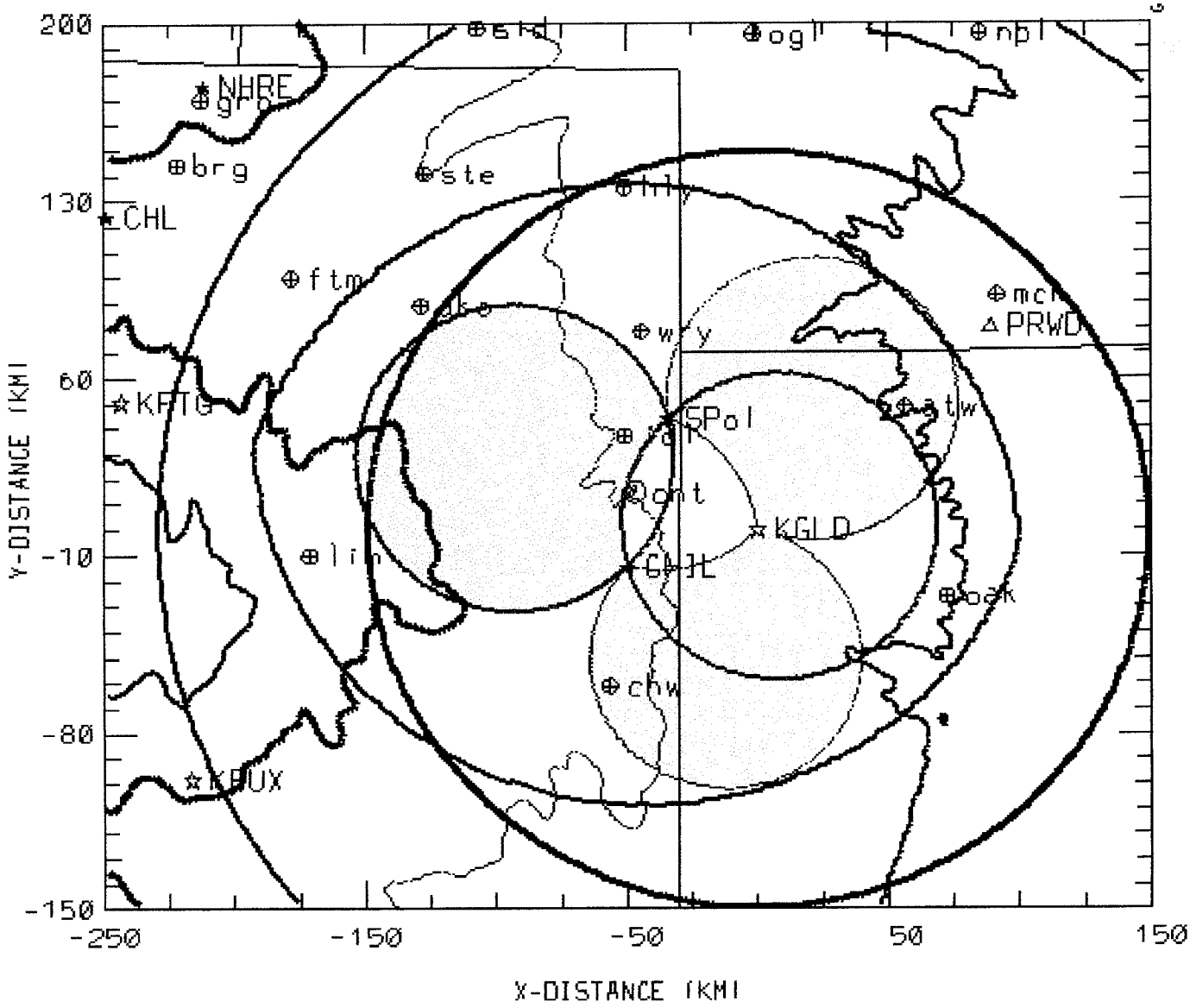

Figure 4.20: STEPS triple-Doppler radar network. The origin is at Goodland, Kansas where the WSR-88D is located. Two dark solid circles are range rings at 150 *km* and 230 *km* from Goodland. Inside blue line area is 150 *km* or less from the two research radars (S-Pol and CSU-CHILL).

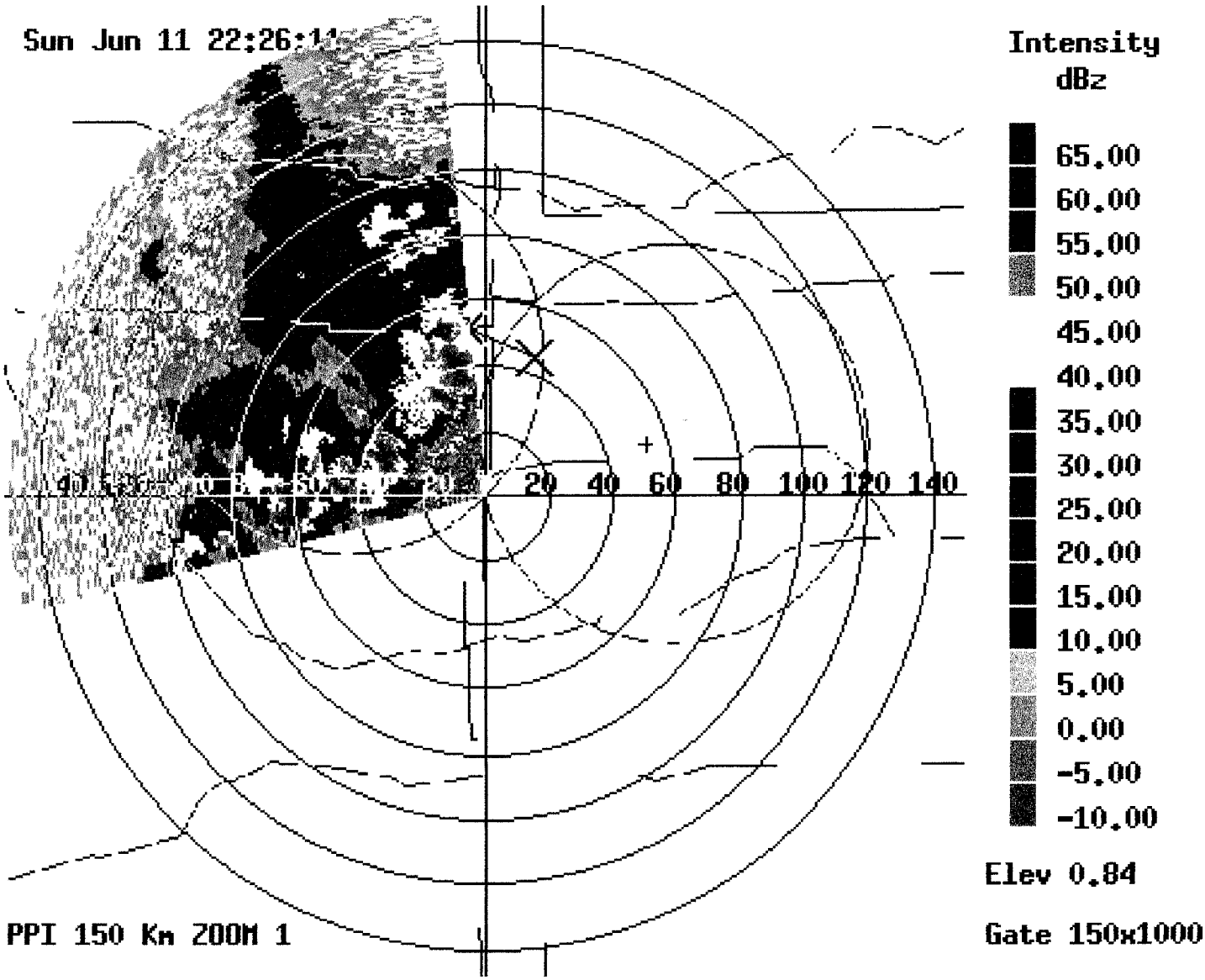

Figure 4.21: Radar scan of Z_h on June 11, 2000. We can identify a rain cell which located at azimuth angle around 350^o and range around 40 km from CSU-CHILL.

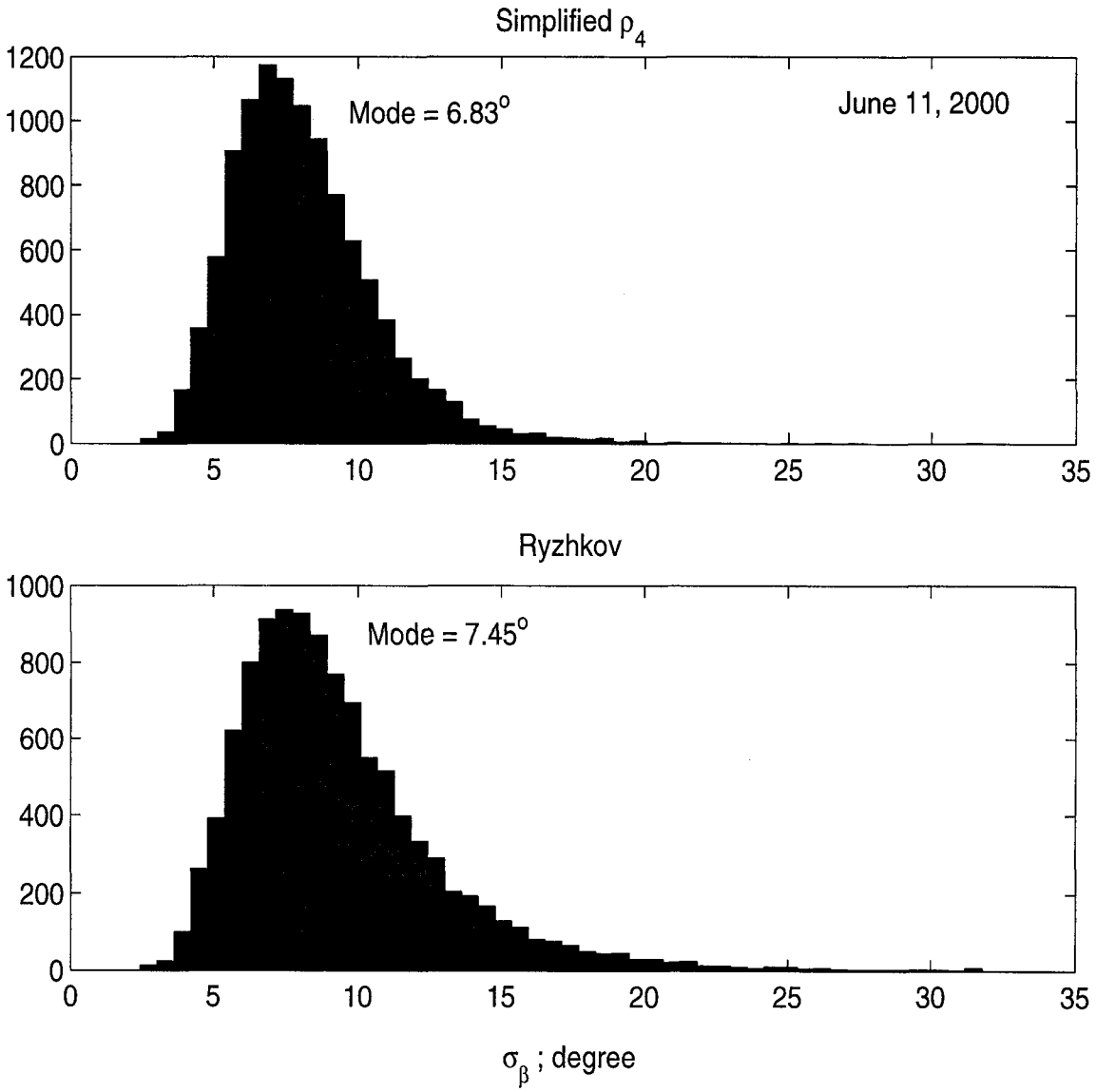

Figure 4.22: Same as Fig. 4.16 except from June 11, 2000 (10,807 data points).

is very small (around 0.6^o) with the Ryzhkov algorithm slightly over-estimating compared with the ρ_4 algorithm. Moreover, the histogram of σ_β using the Ryzhkov algorithm is broader than using the simplified ρ_4 algorithm. This phenomenon is not in agreement with the simulation results. One possible explanation is that this data set is from a very intense rain event and includes the volumes from two different elevations (0.55 and 1.1^o). So the variation of drop size and shape may be larger, since the simplified ρ_4 algorithm is less sensitive with drop size and shape compared with the Ryzhkov algorithm. Therefore, the standard deviation of estimated σ_β by using the simplified ρ_4 algorithm should be smaller.

Fig 4.23 shows estimated σ_β versus Z_{dr}. As in Fig. 4.17, the upper panel shows the scatter plot while the lower plot shows bin averaged data. In agreement with the previous datasets, the tendency for σ_β to decrease, on average, with increase in Z_{dr} is maintained in this data set also (case of very intense rain storm with large drops most likely formed from melting of graupel and tiny hailstones as opposed to the earlier more "tropical" like rain events). It seems that polarimetric based rain rate algorithms may have to take into account the behavior of σ_β versus Z_{dr} for accurate retrievals of rain rate (the usual approximation is to assume that σ_β is fixed at about 5-10^o independent of drop size).

4.5 Summary

In this chapter, we first studied the impact of drop oscillations on effective drop shapes. We also explained how multi-mode oscillations can effectively increase the standard deviation of canting angle. In Section 1, we explored the relation between orientation angles (θ_b and ϕ_b) and canting angle (β). Moreover, we study two possible orientation distributions (Gaussian and Holt) by computer simulation. Based on this relation and polarization theories, we explain two existing algorithms (Ryzhkov and ρ_4 algorithms) which are used to estimate the standard deviation

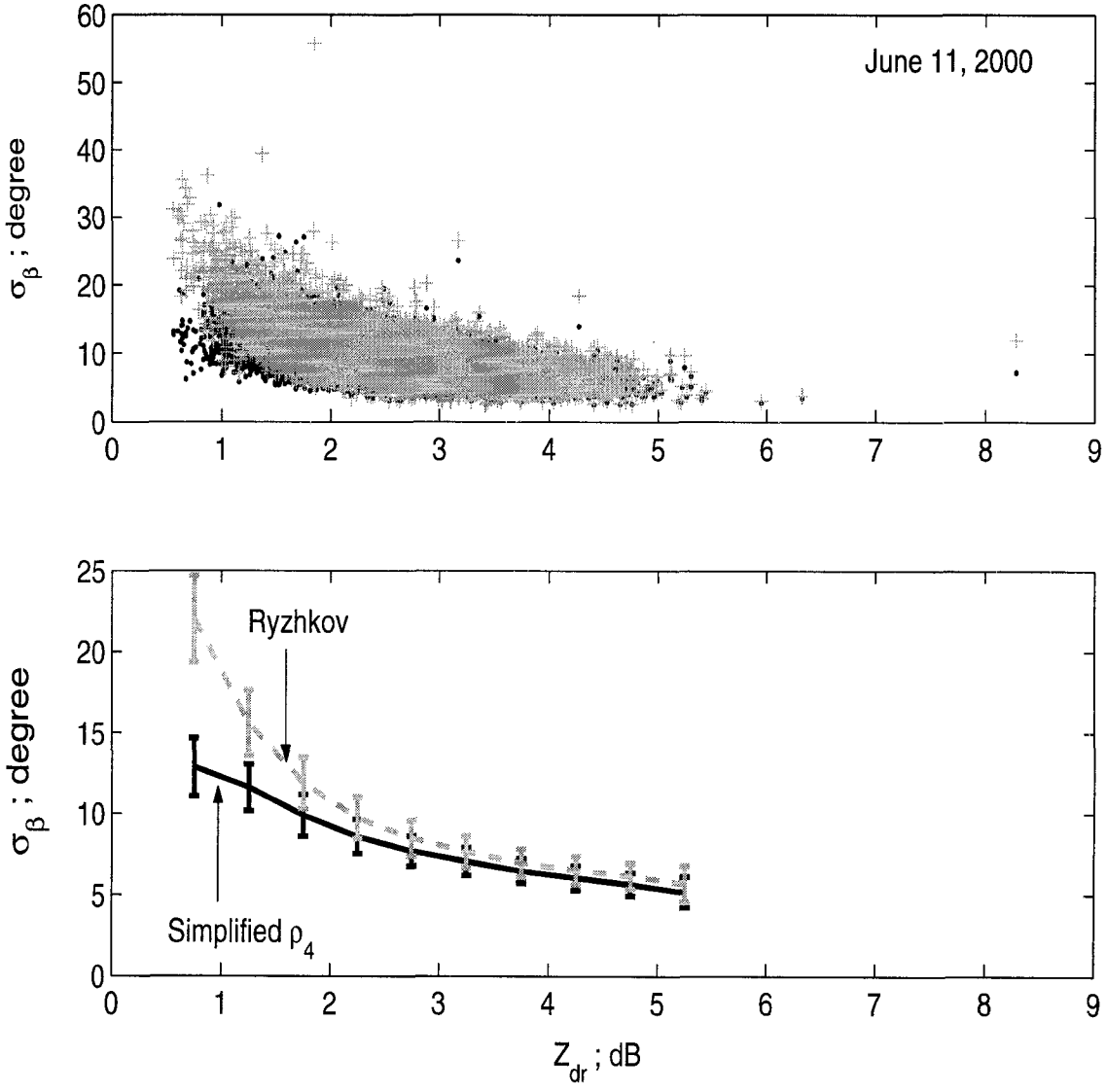

Figure 4.23: Same as Fig. 4.17 except from June 11, 2000.

of canting angle (σ_β), and have proposed two new algorithms (Asymmetric ratio algorithm and simplified ρ_4 algorithm).

In section 3, we examined the stability of three algorithms (simplified ρ_4, Ryzhkov and asymmetric ratio algorithm). We found that these three algorithms were not sensitive to details of the rain models (dsd and mean axis ratio) and to measurement errors. Moreover, we also showed that it is impossible to distinguish between two different orientation distributions with the same standard deviation by using dual-polarization radar parameters such as Z_{dr}, LDR and ρ_{hv}. Finally, we applied the Ryzhkov and simplified ρ_4 algorithms to three cases (Flood, Duke and STEPS case). The analysis show that both Ryzhkov and simplified algorithms can give reasonable results for σ_β versus Z_{dr}.

Fig. 4.24 shows the tendency. Note that the relative error is calculated by,

$$Error = 100\frac{\sigma_{\beta,Ryzhkov} - \sigma_{\beta,simplified\rho_4}}{\sigma_{\beta,simplified\rho_4}} \tag{4-52}$$

The absolute values of relative error are larger at small Z_{dr} and smaller at larger Z_{dr}. There is one possible explanation for this phenomenon. The Ryzhkov algorithm uses Z_{dr} and LDR to estimate σ_β, and assumes that the mean axis ratio follows the Pruppacher-Pitter axis ratio model. Fig. 4.25 shows the calculated relation between Z_{dr}, σ_β and LDR by using the Ryzhkov algorithm. If mean the shape of drops are more (or less) oblate compared with the Pruppacher-Pitter model, Z_{dr} would become larger (smaller) and LDR would become smaller (larger) for any canting angle. From Fig. 4.25, the Ryzhkov algorithm would tend to under-estimate (over-estimate) the σ_β. If the amplitude of oscillations is around the same, it would change the mean axis ratio (relatively) more for small drops as compared to big drops. Moreover, large drops are usually formed by melting of ice particles, and may contain melting ice cores. So the shape of larger drops tends to be stable. Actually, some studies have shown that drops > 2 mm agree well with

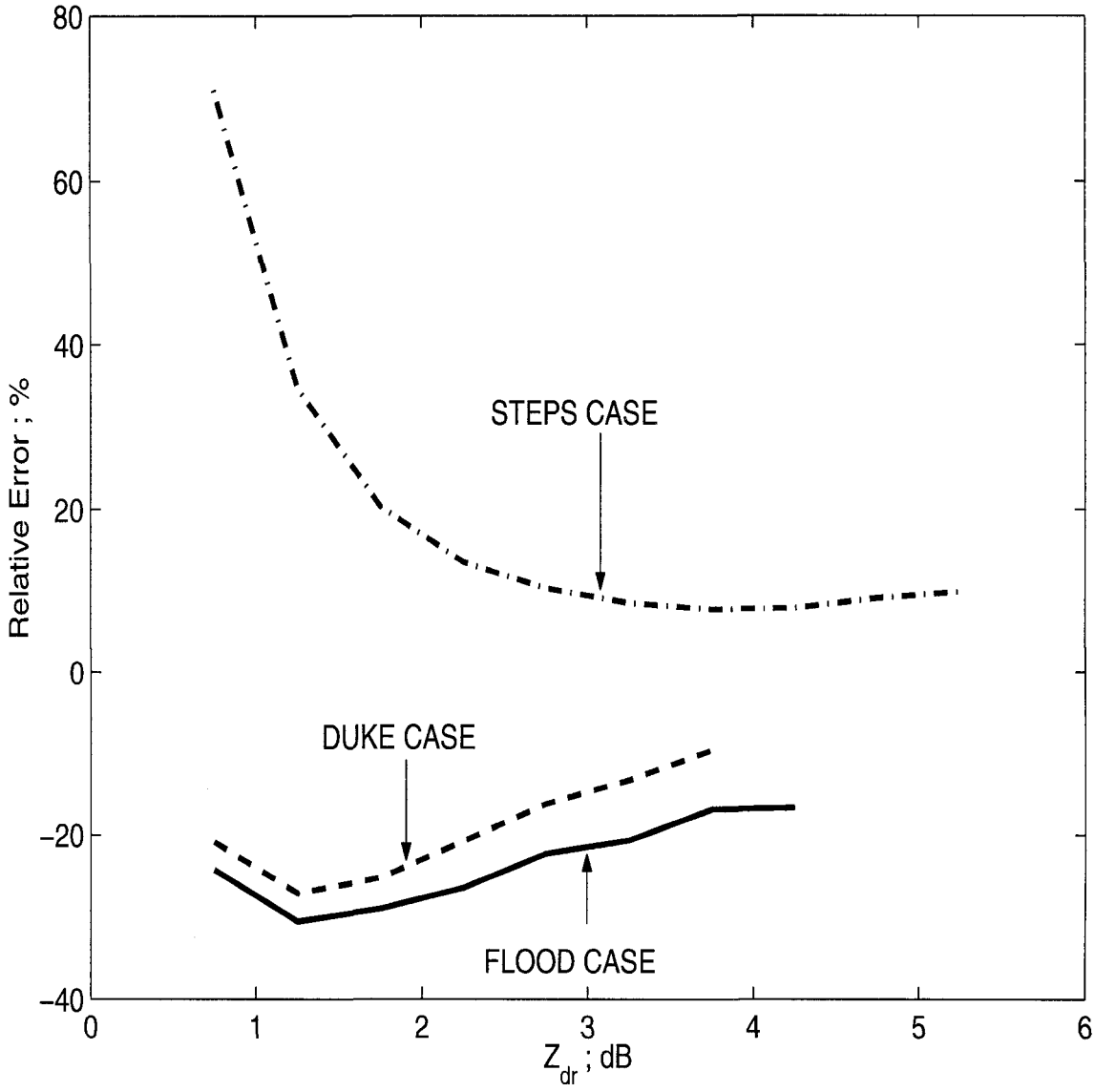

Figure 4.24: Relative error of the Ryzhkov algorithm with respect to the simplified ρ_4 algorithm. The relative error is smaller when Z_{dr} is larger.

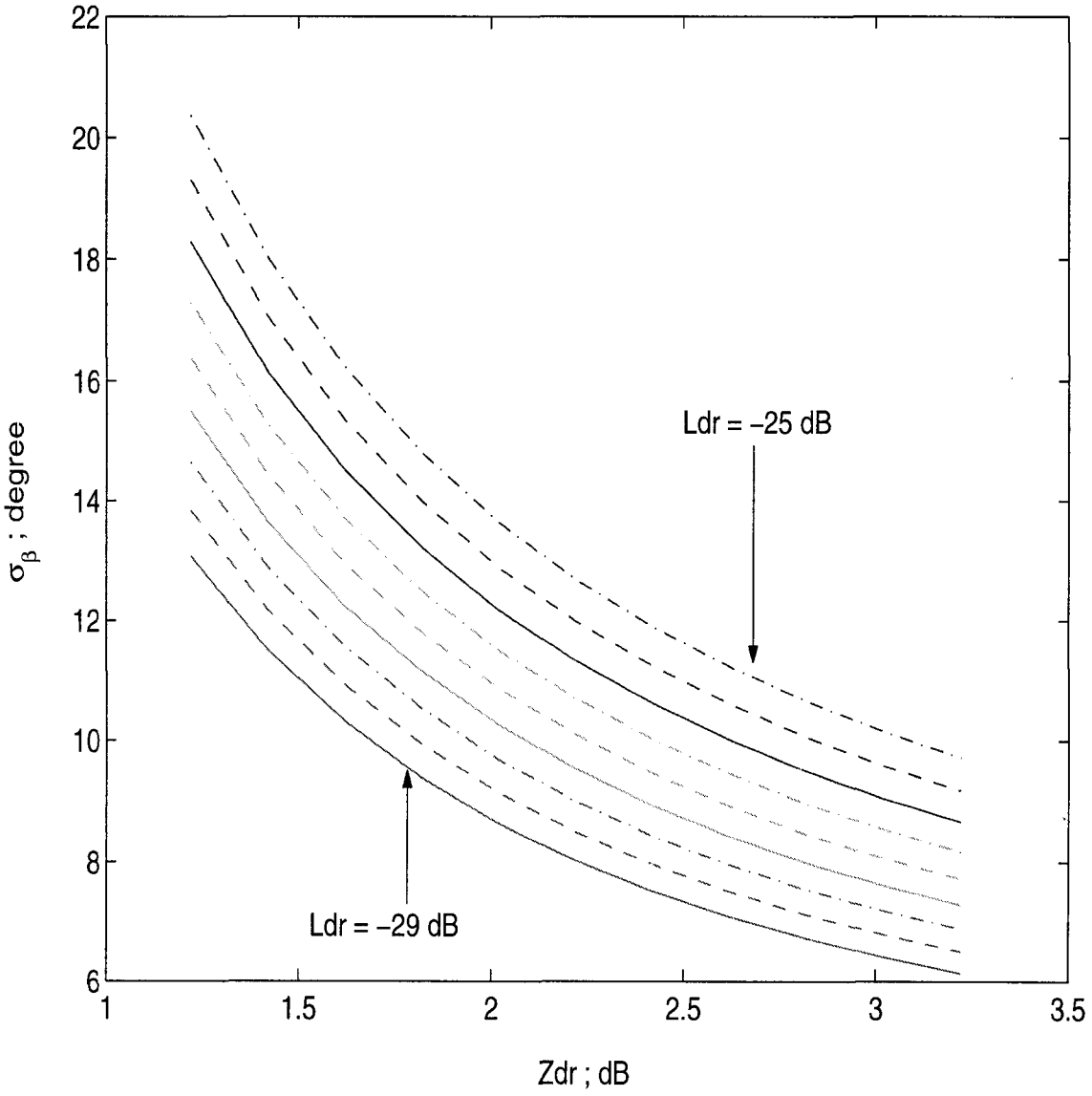

Figure 4.25: Z_{dr} versus estimated σ_β for different LDR values using the Ryzhkov algorithm. Each line represents a fixed LDR value. The LDR values are from -29 dB to -25 dB with 0.5 dB step.

wind-tunnel measurements of stable drop shape (Pruppacher et. al. 1971, Beard et. al. 1987)[41, 7]. Therefore, the Ryzhkov algorithm will tend to over or underestimate for small drops (small Z_{dr}) and tend to be more accurate for larger drops (large Z_{dr}).

On the other hand, the simplified ρ_4 algorithm uses Z_{dr}, LDR and $Re[R_{co}]$ to estimate σ_β. Fig. 4.26 shows surfaces of constant σ_β ($\sigma_\beta = 5$, 10 and 15^o) calculated for the simplified ρ_4 algorithm. When drops are more (or less) oblate, Z_{dr} becomes larger (smaller) and the algorithm will tend to overestimate σ_β (see Fig. 4.26b). At the same time, $Re[R_{co}]$ will become smaller (larger) and LDR will become smaller because $|S_{vh}|$ reduces (increases). The algorithm will tend to underestimate σ_β (see Fig. 4.26c). Overall, the variation of estimated σ_β due to the drop shape change may be minimized. Apparently, the simplified ρ_4 algorithm does as well as the ρ_4 algorithm and is less affected by drop shapes. If our hypothesis (explanation) is correct, the difference between the two algorithm may play an important role in drop shape identification.

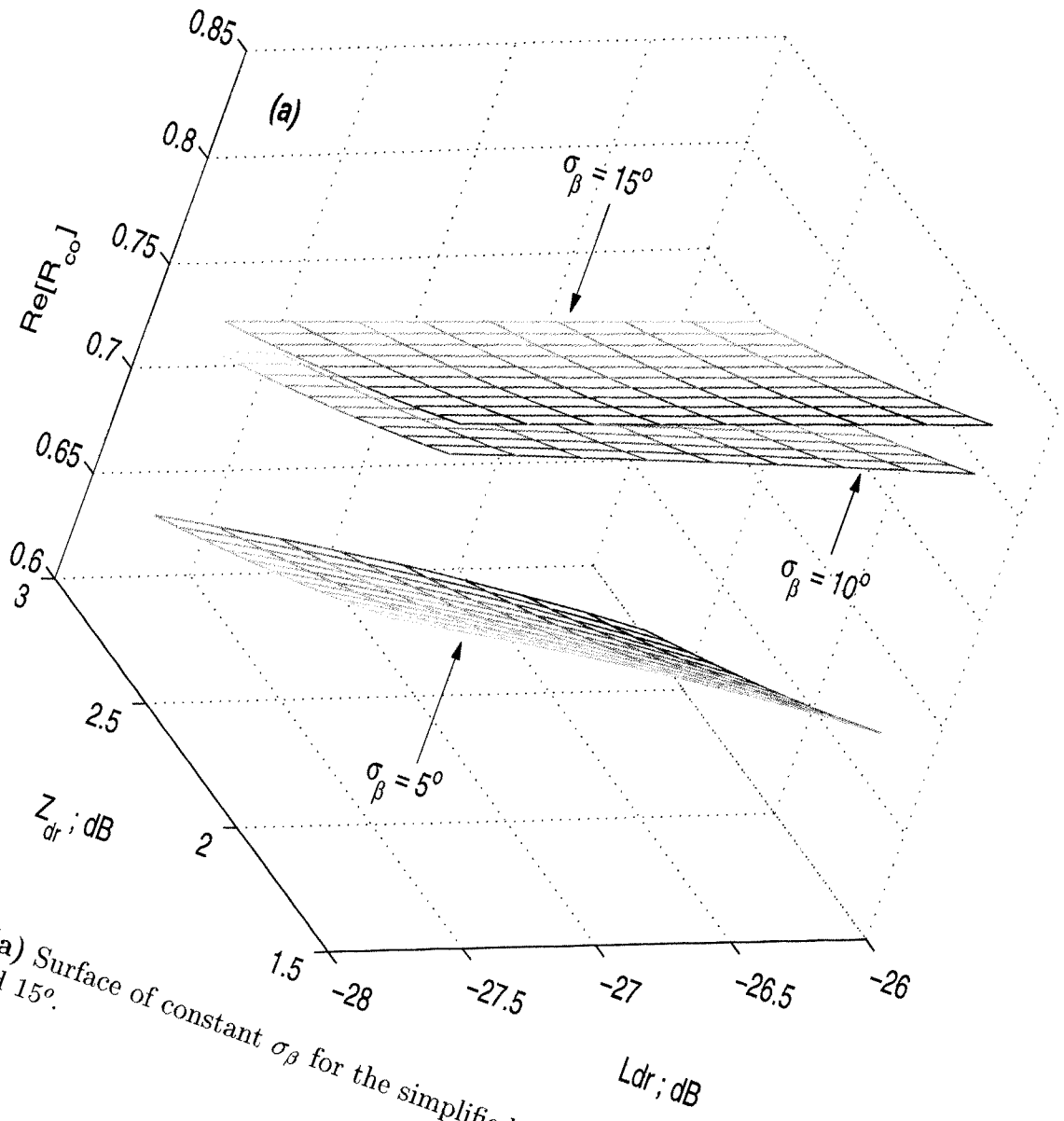

Figure 4.26: **(a)** Surface of constant σ_β for the simplified ρ_4 algorithm. The σ_β is set at 5, 10 and 15°.

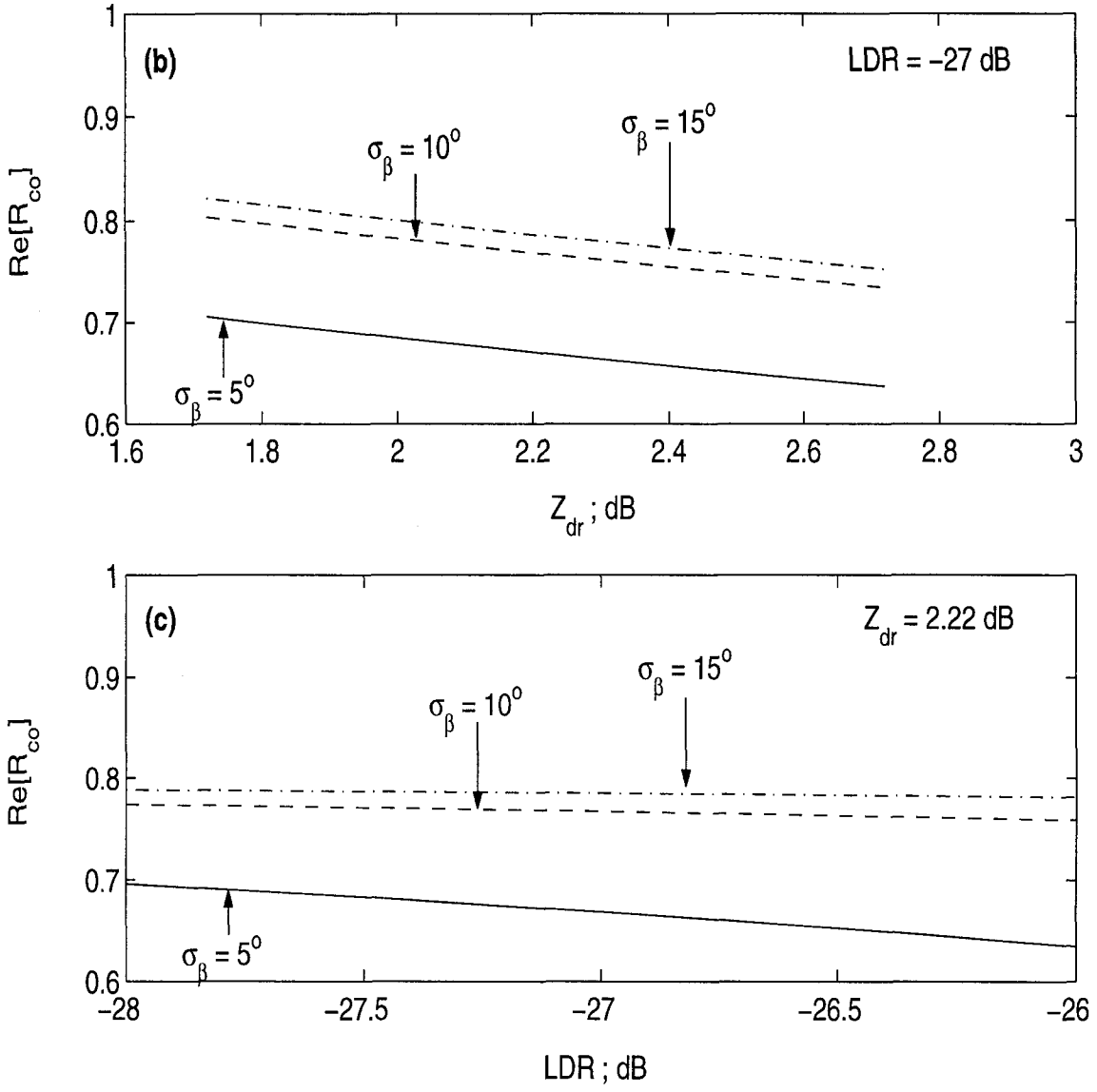

Figure 4.26: (cont.) **(b)** Z_{dr} versus $Re[R_{co}]$ for $LDR = -27\ dB$ **(b)** LDR versus $Re[R_{co}]$ for $Z_{dr} = 2.22\ dB$. Each line represents a constant σ_β (σ_β = 5, 10 and 15^o).

Chapter 5

CONCLUSION

5.1 Summary and Discussion

In this Dissertation, we studied the microphysical properties of rain and, subsequently, to get better rainfall rate estimation. The introductory chapter gives a brief review of radar meteorology, and then introduces polarization theories and some useful tools for dual-polarization radar analysis such as scattering matrix, covariance matrix and basis transformation.

Following the introduction, we proposed a mean areal rainfall rate estimator by using ϕ_{dp}. This estimation is based on the R-K_{dp} relationship. In order to reduce measurement fluctuations and random errors, we integrate the rainfall rate over an area. Since radar does not measure K_{dp} directly, we apply $K_{dp} = 0.5 * d\phi_{dp}/dr$ into our formula. Ryzhkov and Zrinć (2000)[44] derived a related mean areal R algorithm that assumed that K_{dp} is constant (or ϕ_{dp} is linear increasing) over the estimated area. However, this assumption can cause range weighting problem especially for a narrow K_{dp} profile versus range. Therefore, we used piece-wise linear fitting method and then assumed a "locally" linear R-K_{dp} relation. To compare these two algorithms, we analyzed the error structure of the algorithms by computer simulations and studied 12 rain cases using the C-Pol radar at Darwin, Australia and one case using the S-Pol radar in Brazil. Moreover, we introduced β correction (Gorgucci et al. 2000)[17] method into the two algorithms where

β is the slope of mean axis ratio versus drop diameter (which can change due to drop oscillations). Both computer simulations and case study analysis showed that our algorithm can give accurate estimation, and that β correction can reduce the estimation bias significantly for both algorithms.

In Chapter 3, we extend the application of β to evaluate parameters of the gamma drop size distribution. If radar parameters (Z_h, Z_{dr} and K_{dp}) satisfy certain pre-specified thresholds, we calculate β first, and then, calculate D_o and N_w by using β, Z_h and Z_{dr} (Gorgucci et al. 2001,2002)[18, 14]. Otherwise, if $Z_h > 0$ dBZ and $Z_{dr} > 0.2$ dB, we calculate D_o and N_w using Z_h and Z_{dr} only. After evaluating the gamma dsd parameters over an area, we propose an adjustable Z-R relationship whose exponent is fixed at 1.5 and whose multiplicative constant is function of μ and N_w. This pol-based Z-R relationship is simple and flexible. It can reduce measurement fluctuations because the coefficient is based on dsd parameters that are averaged over an area, and then applied to each resolution volume. To validate our methods, we compare radar retrieved dsd parameters with profiler dsd retrievals. We also compare the rain rate by using our pol-based Z-R relationship with gage rain rate. Case studies show that both radar retrieved dsd and rainfall rate estimates agree quite well with profiler dsd and gage rain rate.

There are three important features of precipitation, namely, the drop size distribution, mean axis ratio of drops and and drop orientation distribution. We studied the first two in Chapters 2 and 3. In Chapter 4, we study the drop orientation which appears to be governed by turbulence and drop oscillation. Although drops are actually oriented in 3-D space, radar can only observe drop orientation in the polarization plane. So we first study the relations between orientation angles (θ_b and ϕ_b) and canting angle (β). Note that β is refereed to as "slope of mean axis ratio versus drop diameter" in previous chapters but as "canting angle" in Chapter 4. Using the scattering and covariance matrices, we develop two

algorithms for σ_β which are referred to as the asymmetric ratio algorithm and the simplified ρ_4 algorithm. We examine the stability of these two algorithms along with the Ryzhkov algorithm (2001)[42]. We apply the Ryzhkov algorithm and the simplified ρ_4 algorithm to three rain cases. Both algorithms give reasonable results but do not agree with each other at low Z_{dr} values. However, we are able to explain this disagreement theoretically. We believe that the simplified ρ_4 algorithm is more accurate when drop shapes are not following the linear Pruppacher-Pitter model, perhaps due to drop oscillations or other reasons.

5.2 Future Research Suggestions

One of the main goals of weather radar is to get better estimates of precipitation. To get a better estimation using physically-based approaches, we need to understand the microphysical properties of precipitation. For example, although we can show that the areal rainfall rate algorithm based on Φ_{dp} can reduce measurement fluctuations and random noise and is mathematically unbiased, in reality, the normalized bias (NB) for an individual case could be very large (-44% the worst case). It may be due to the R-K_{dp} relation not being valid because of drop oscillations. We can use β correction applied over an area as we did for the S-Pol radar case. However, at C-band the β-correction has not been sufficiently validated because attenuation-correction of Z_h and Z_{dr} has to be applied prior to any β-correction (which will introduce additional errors so as to make the β-correction unreliable).

In Chapter 4, we proposed a pol-based Z-R relationship. The multiplicative coefficient is dependent on the radar retrieved dsd parameters. Basically, we estimate the dsd parameters by using β_{eff}, Z_h and Z_{dr}. Here we assume that the actual non-linear relation between mean axis ratio and D may be equivalent to a linear model which would keep K_{dp} the same. The linear model is $r = 1.03 - \beta_{eff} D$

where r is the mean axis ratio. The validation of radar retrieved dsd is evaluated by comparing against profiler dsd retrievals. The profiler estimates dsd by using sds (single Doppler spectrum) method and a statistical method. We found that the dual-pol radar retrieved dsd agreed well with either the sds method or the statistical method for $R > 5\ mm\ h^{-1}$. We still need to analyze more cases to understand the difference between sds and statistical method. Moreover, we also found that the estimated rainfall rate by using the pol-based Z-R would have larger error at high Z_h gradient region compared with gage rainfall rate. This is not unexpected as in regions of large gradients the gage point estimate of R cannot accurately be "mapped" into a surface estimate. Thus, a significantly larger proportion of the radar-gage error may be due to the "point-to-surface conversion" error of gages alone. Thus, radar retrievals of R should be compared with gages only when the gradient of Z_h over the region represented by the gage is small (uniform rain).

The last topic of this dissertation is drop orientation. We study the relation of drop orientation and canting angle and propose two algorithms to estimate the standard deviation of canting angle (σ_β). Here we assume that the mean canting angle is zero based on the expected natural behavior of drop orientation (i.e., the azimuthal angle ϕ_b should be uniformly distributed). However, previous studies have shown that antenna misalignment can cause the H/V basis to be rotated slightly (Huang et al. 2001)[24]. In this case, the mean canting angle will be close but not be equal to zero. We can examine the mean canting angle by using the covariance matrix. In order to do so, we need to calibrate the covariance matrix accurately. We apply two algorithms to estimate σ_β in three cases. Theoretically, these two algorithms should give very close results. The data show that they are in good agreement at large Z_{dr} but deviate at small Z_{dr}. We give a reasonable explanation but lack solid proof. We can validate our estimation by analyzing 2-D video disdrometer data because this instrument can give the drop shape and orientation

separately. By analyzing 2D-video data, we can establish more accurate precipitation models (including drop size distribution, orientation distribution and mean axis ratio model) and get more information about the microphysical properties of precipitation. Subsequently, we can estimate precipitation even more accurately by using polarimetric radar technology.

Bibliography

[1] E. Andsager, K. V. Beard, and N. F. Laird. Laboratory measurements of axis ratios for large raindrops. *J. Atmos. Sci.*, 56:2673–2683, 1999.

[2] E. V. Appleton and M. A. F. Barnett. On some direct evidence for downward atmospheric reflection of electric rays. In *Proc. Roy. Soc..*, volume 109 of *A*, pages 621–641, 1926.

[3] D. Atlas. Microwave scattering from nonspherical hydrometeors. In *In Proc. Conf. on Water Resources.*, volume Bull 41, pages 269–276. Illinois, State Water Survey, 1951.

[4] D. Atlas, R. C. Srivastava, and R. S. Sekhon. Doppler radar characteristics of precipitation at vertical incidence. *Rev. Geophys. Space Phys.*, 2:1–35, 1973.

[5] D. Atlas and C. W. Ulbrich. Path- and area-integrated rainfall measurement by microwave attenuation in th 1-3 cm band. *J. Appl. Meteor.*, 16:1322–1331, 1977.

[6] K. Aydin, H. Direskeneli, and T. A. Seliga. Dual-polarization radar estimation of rainfall parameters compared with ground-based disdrometer measurements: October 29, 1982, central illinois experiment. *IEEE Trans. Geosci. Remote Sens.*, GE-25:834–844, 1987.

[7] K. V. Beard and C. Chuang. A new model for the equilibrium shape of raindrops. *J. Atmos. Sci.*, 44:1509–1524, 1987.

[8] K. V. Beard and A. R. Jameson. Raindrop canting. *J. Atmos. Sci.*, 40:448–454, 1983.

[9] V. N. Bringi and V. Chandrasekar. *Polarimetric Doppler weather radar : Principles and application.* Cambridge Univ. Press, Cambridge, UK, 2001.

[10] V. N. Bringi, V. Chandrasekar, and R. Xiao. Raindrop axis ratios and size distributions in florida rainshafts: An assessment of multiparameter radar algorithms. *IEEE Trans. Geosci. Remote Sens.*, 36:703–715, 1998.

[11] V. N. Bringi, G. Huang, V. Chandrasekar, and E. Gorgucci. A methodology for estimating the parameters of a gamma raindrop size distribution model from polarimetric radar data: Application to a squall-line event from the trmm/brazil campaign. *J. Atmos. Oceanic Tech.*, 19:633–645, 2002.

[12] V. N. Bringi, G. Huang, V. Chandrasekar, and T. D. Keenan. An areal rainfall estimator using differential propagation phase: Evaluation using a c-band radar and a dense gage network in the tropics. *J. Atmos. Oceanic Tech.*, 18:1810–1818, 2001a.

[13] V. N. Bringi, T. D. Keenan, and V. Chandrasekar. Correcting c-band radar reflectivity and differential reflectivity data for rain attenuation: A self-consistent method with constraints. *IEEE Trans. Geosci. Remote Sens.*, 39:1906–1915, 2001b.

[14] E. Gorgucci, V. Chandrasekar, V. N. Bringi, and G. Scarchilli. Estimation of raindrop size distribution parameters from polarimetric radar measurements. *J. Atmos. Sci.*, 59:2373–2384, 2002.

[15] E. Gorgucci, G Scarchilli, and V. Chandrasekar. A robust estimator of rainfall rate using differential reflectivity. *J. Atmos. Oceanic Tech.*, 1:586–592, 1994.

[16] E. Gorgucci, G. Scarchilli, and V. Chandrasekar. Estimation of mean raindrop shape from polarimetric radar measurements. In *29th Int. Conf. on Radar Meteor.*, pages 168–171. Amer. Meteor. Soc., 1999.

[17] E. Gorgucci, G. Scarchilli, V. Chandrasekar, and V. N. Bringi. Measurement of mean raindrop shape from polarimetric radar observations. *J. Atmos. Sci.*, 57:3406–3413, 2000.

[18] E. Gorgucci, G. Scarchilli, V. Chandrasekar, and V. N. Bringi. Rainfall estimation from polarimetric radar measurements: Composite algorithms independent of raindrop shape-size relation. *J. Atmos. Oceanic Tech.*, 18:1773–1786, 2001.

[19] A. W. Green. An approximation for the shapes of large raindrops. *J. Appl. Metero.*, 14:1578–1583, 1975.

[20] A. Hendry, Y. M. M. Antar, and G. C. McCormick. On the relationship between the degree of preferred orientation in precipitation and dual-polarization radar echo characteristics. *Radio Sci.*, 22:37–50, 1987.

[21] A. Hendry and G. C. McCormick. Polarization related parameters for rain: Measurements obtained by radar. *Radio Sci.*, 11:731–740, 1976.

[22] A. R. Holt. Some factors affecting the remote sensing of rain by polarization diversity radar in the 3- to 35-ghz frequency range. *Radio Sci.*, 19:1399–1412, 1984.

[23] G Huang. The two transmitters/two receivers csu-chill radar system: Calibration issues and sample data analysis. Master's thesis, Colorado State University, 1997.

[24] G. Huang, Hubbert J. C., and V. N. Bringi. Precipitation canting angle distribution estimation from covariance matrix analysis of csu-chill radar data. In *30th Int. Conf. on Radar Meteor.*, pages 651–653. Amer. Meteor. Soc., 2001.

[25] J. Hubbert and V. N. Bringi. An iterative filtering technique for the analysis of copolar differential phase and dual-frequency radar measurements. *J. Atmos. Oceanic Technol.*, 12:643–648, 1995.

[26] A. J. Illingworth and Blackman T. M. The need to normalise rsds based on the gamma rsd formulations and implications for interpreting polarimetric radar data. In *29th Int. Conf. on Radar Meteor.*, pages 629–631. Amer. Meteor. Soc., 1999.

[27] A.R. Jameson. Microphysical interpretation of multi-parameter radar measurements in rain. part i: Interpretation of polarization measurements and estimation of raindrop shape. *J. Atmos. Sci.*, 40:1792–1802, 1983.

[28] A.R. Jameson. Relations among linear and circular polarization parameters measured in canted hydrometeors. *J. Atmos. Oceanic Technol.*, 4:634–645, 1987.

[29] R. C. Jones. A new calculus for the treatment of optical system. *J. Opt. Soc. Amer.*, 31:488–493, 1941.

[30] T. D. Keenan, K. Glasson, F. Cummings, T. S. Bird, R. J. Keeler, and J. Lutz. The bmrc/ncar c-band polarimetric (c-pol) radar syatem. *J. Atmos. Oceanic Technol.*, 15:871–886, 1998.

[31] J. M. Kwiatkowski and A. B. Kostinski. The use of optimal polarizations for studying the microphysics of precipitation: Nonattenuating wavelengths. *J. Atmos. Oceanic Technol.*, 12:96–114, 1995.

[32] M. Maki, T. D. Keenan, Y. Sasaki, and K. Nakamura. Spatial variability of raindrop size distribution in tropical continental squall lines. In *29th Int. Conf. on Radar Meteor.*, pages 651–654. Amer. Meteor. Soc., 1999.

[33] K. V. Mardia. *Statistics of Directional Data.* Academic Press, New York, 1972.

[34] J. S. Marshall and W. M. K. Palmer. The distribution of raindrops with size. *J. Meteor.*, 5:165–166, 1948.

[35] P. T. May, T. D. Keenan, D. S. Zrnić, L. D. Carey, and S. A. Rutledge. Polarimetric radar measurements of tropical rain at a 5-*cm* wavelength. *J. Appl. Meteor.*, 38:750–765, 1999.

[36] G. C. McCormick and A. Hendry. Radar measurement of precipitation-related depolarization in thunderstorm. *IEEE Trans. Geosci. Electron.*, GE-17:142–150, 1979.

[37] G. C. McCormick, A. Hendry, and B. L. Barge. The anisotropy of precipitation media. *Nature*, 238:214–216, 1972.

[38] J. I. Metcalf. A new slant on the distribution and measurement of hydrometeor canting angles. *J. Atmos. Oceanic Technol.*, 5:571–578, 1988.

[39] V. Nespor, W. F. Krajewski, and A. Kruger. Wind-induced error of rain drop size distribution measurement using a two-dimensional video disdrometer. *J. Atmos. Oceanic Technol.*, 17:1483–1492, 2000.

[40] H. R. Pruppacher and K. V. Beard. A wind tunnel investigation of the internal circulation and shape of water drops falling at terminal velocity in air. *Quart. J. Roy. Meteor. Soc.*, 96:247–256, 1970.

[41] H. R. Pruppacher and R. L. Pitter. A semi-empirical determination of the shape of cloud and rain drops. *J. Atmos. Sci.*, 28:86–94, 1971.

[42] A. Ryzhkov. Interpretation of polarimetric radar covariance matrix for meteorological scatterers: Theoretical analysis. *J. Atmos. Oceanic Technol.*, 18:315–328, 2001.

[43] A. Ryzhkov and D. S. Zrinć. Assessment of rainfall measurement that uses specific differential phase. *J. Atmos. Oceanic Technol.*, 35:2080–2090, 1996.

[44] A. Ryzhkov, D. S. Zrinć, and R. Fulton. Areal rainfall estimates using differential phase. *J. Appl. Metero.*, 39:263–268, 2000.

[45] M. Sachidananda and D. S. Zrnić. Rain rate estimated from differential polarization measurements. *J. Atmos. Oceanic Technol.*, 4:588–598, 1987.

[46] D. S. Saxon. Tensor scattering matrix for the electromagnetic field. *Phys. Rev.*, 100:1711–1775, 1955.

[47] T. A. Seliga and V. N. Bringi. Potential use of radar differential reflectivity measurements at orthogonal polarizations for measuring precipitation. *J. Appl. Metero.*, 15:69–76, 1976.

[48] T. A. Seliga and V. N. Bringi. Differential reflectivity and differential phase shift: Applications in radar meteorology. *Radio Sci.*, 13:271–275, 1978.

[49] B.A. Silverman, L. K. Rogers, and D. Dahl. On the sampling variance of rain gauge networks. *J. Appl. Meteor.*, 20:1468–1478, 1981.

[50] J. Testud, S. Oury, P. Amayenc, and R. A. Black. The concept of "normalized" distributions to describe raindrop spectra: a tool for cloud physics and cloud remote sensing. *J. Appl. Meteor.*, 40:1118–1140, 2001.

[51] A. Tokay and K. V. Beard. A field study of raindrop oscillations. part i: Observation of size spectra and evaluation of oscillation causes. *J. Appl. Meteor.*, 35:1671–1687, 1996.

[52] A. Tokay, O. W. Thiele, A. Kruger, and W. F. Krajewski. New measurements of drop size distribution and its impact in radar rainfall retrievals. In *29th Int. Conf. on Radar Meteor.*, pages 659–662. Amer. Meteor. Soc., 1999.

[53] K. Tragl. Polarimetric radar backscattering from reciprocal random targets. *IEEE Trans. Geosci. Remote Sens.*, 28:856–864, 1990.

[54] C. W. Ulbrich. Natural variations in the analytical form of raindrop size distributions. *J. Climate Appl. Meteor.*, 22:1764–1775, 1983.

[55] H. C. van de Hulst. *Light scattering by small particle.* Wiley, New York, 1957.

[56] C. R. Williams, A. Kruger, K. S. Gage, A. Tokay, R. Cifelli, W. F. Krajewski, and C. Kummerow. Comparison of simultaneous raindrop size distributions estimated from two surface disdrometers and a uhf profiler. *Geophys. Res. Lett.*, 27:1763–1766, 2000.

[57] P. T. Willis. Functional fits to some observed dropsize distributions and parameterization of rain. *J. Atmos. Sci.*, 41:1648–1661, 1984.